MOTION ASPECTS IN JOINT IMAGE RECONSTRUCTION AND NONRIGID MOTION ESTIMATION

by

Se Young Chun

A dissertation submitted in partial fulfillment
of the requirements for the degree of
Doctor of Philosophy
(Electrical Engineering: Systems)
in The University of Michigan
2009

Doctoral Committee:

Professor Jeffrey A. Fessler, Chair
Professor Alfred O. Hero III
Professor Charles R. Meyer
Assosiate Professor Selim Esedoglu
Associate Professor Marc L. Kessler

In memory of my father, Ye Ki Jun ...

ACKNOWLEDGEMENTS

I have been enjoying my Ph.D. program in Ann Arbor a lot not only because of all the interesting research topics, but also because of all people I have in my life. Without them, I wouldn't be able to survive and finish this program. I would like to thank God for sending me to Michigan and orchestrating my life among all people I met in Ann Arbor. The personal walk with Him was the source of my strength for the last 6 years.

I thank my late father, Ye Ki Jun, for supporting me in many different ways. Without his promise to support me for a year, I wouldn't be able to come to the United States. I know that it would be him to be the happiest person for my Ph.D., but I am sad that he couldn't enjoy this moment with my family. Many people will miss him. However, I am still thankful that I can share my joy with my family, my mother Soon Ja Park, my sister Mi Hyun Jeon, my brother-in-law Masafumi Fuchikami, and my nephew Harumitsu Fuchikami. Family gatherings in Korea and Japan always cheered me up.

I would like to thank my advisor Jeff Fessler for many things. I have been really enjoying working with him. His intuition for the problem, his passion for the research, and his openness to any possibilities such as my naive ideas have inspired me and I've learned a lot from him. It has been my privilege to work with him. I would also like to thank my thesis committee members, professor Hero, professor Meyer, professor Esedoglu, and professor Kessler. I really enjoyed meetings with them and had great feedbacks to my dissertation. It was such an honor to have them as a thesis committee.

I would like to thank my friends. A Ph.D. program could be very dry, but I have

enjoyed my 'long' stay in Ann Arbor because of them. I am sorry that I couldn't list all your names in here. My life in the lab has been joyous because of my labmates. I enjoyed my conversations with them whether it is related to research topics or not. It was always a good break to talk with them in the midst of the work. My life outside the lab has also been amazing because of my friends from my church, Harvest Mission Community Church. I could meet so many wonderful friends through this church and they helped me in many ways. My Korean friends in Ann Arbor have also been a great cheer-up for me. Having a conversation with them in my own language has been invaluable to me.

TABLE OF CONTENTS

LIST OF FIGURES

LIST OF TABLES

LIST OF APPENDICES

<u>Appendices</u>

ABSTRACT

MOTION ASPECTS IN JOINT IMAGE RECONSTRUCTION AND NONRIGID MOTION ESTIMATION

by

Se Young Chun

Chair: Jeffrey A. Fessler

Many medical imaging applications often require relatively long image acquisition times to form high-SNR images. However, long scan times can lead to motion artifacts. Conventional acquisition and reconstruction methods must sacrifice enough measurements for less motion artifacts or vice versa.

Motion-compensated image reconstruction (MCIR) methods use all collected measurements, but reduce motion artifacts by incorporating motion information into the image reconstruction framework. Several motion incorporation schemes in MCIR have showed superior performance over image reconstruction methods without motion information. However, there has been little research that emphasizes the motion aspects of MCIR. This dissertation addresses a few issues of MCIR methods in motion aspects.

First of all, we investigated methods for motion regularization. The usual choice for a motion regularizer in MCIR has been an elastic regularizer. Recently, there has been much research on regularizing nonrigid deformations with two different motion priors. Conven-

tional methods that enforce deformations to be locally invertible require high computational complexity and large memory. We developed a sufficient condition that guarantees the local invertibility and proposed a simple regularizer based on that sufficient condition. Using both motion invertibility and rigid motion priors may cause conflicts near the diaphragm and the rib cage. We relaxed our motion invertibility regularizer to reduce undesirable bone warping yet better match the image intensities between deformed and target images and permits discontinuous deformations near the sliding area.

Secondly, we studied the statistical properties of MCIR, showing that all MCIR methods are closely related to one another. This study also showed how motion affects the spatial resolution and noise properties of MCIR. We designed spatial regularizers to provide approximately uniform spatial resolution for MCIR. These regularizers enabled different MCIR methods to approximately have the same resolution. Noise properties were compared based on these regularizers.

Lastly, we investigated joint image reconstruction and nonrigid motion estimation with different spatial and motion regularizers and regularization parameters. We performed a 4D PET simulation with lesions. Most MCIR methods produced better-quality images with better SNR and less motion blur. The proposed motion invertibility regularizer allowed more flexibility of deformation estimates compared to a conventional quadratic motion regularizer.

CHAPTER 1

Introduction

1.1 Spatial/temporal tradeoff in image acquisition

When we take a picture of people we usually ask them not to move. We also try not to move when we push the shutter button of a camera. However, we do not worry about being completely still - whether we take photos or pose for them - because we can adjust the shutter speed of the camera. By using a fast shutter speed, we can reduce motion blur and get clearer pictures, as illustrated in Figure 1.1.

However, there are situations that require slower shutter speeds. Figure 1.2 shows photos taken at night. Since there are fewer photons that a camera can collect, longer exposures are needed for better quality photos.

These two examples illustrate the spatial/temporal trade-off in image acquisition. A faster shutter speed is essential to avoid motion blur (high temporal resolution), but it may not collect enough photons (low SNR). On the other hand, a slower shutter speed allows enough time to collect photons (or measurements) for a better quality of images (high SNR) but is prone to motion artifacts (low temporal resolution). Figures 1.1 and 1.2 show

---

[1]"Shutter Speed - Everything You Wanted to Know but Thought it Was Uncool to Ask" at http://www.idigitalphoto.com/shutter-speed-explained/

[2]"Shutter speed in Greenwich" taken by Aram Dulyan.

(a) 1/8 sec

(b) 1/30 sec

(c) 1/60 sec

(d) 1/500 sec

Figure 1.1: Photos with different shutter speeds, illustrating motion artifacts [1].

fortunate cases since there are ways to overcome the limitations in these situations: one has plenty of photons while there is motion, and the other has no motion while there are not many available photons. However the worst situation may happen, *i.e.*, not only having the motion of subjects but also insufficient measurements. Unfortunately, many medical imaging applications fall into this category.

1.2 Limitations in medical imaging modalities

Many medical imaging modalities have been used in clinical settings successfully to improve patient care. However, there are also many application areas where medical imaging modalities cannot capture good quality images due to their innate characteristics of image acquisition speed and patient motion.

(a) 1.3 sec

(b) 2.5 sec

(c) 4 sec

(d) 8 sec
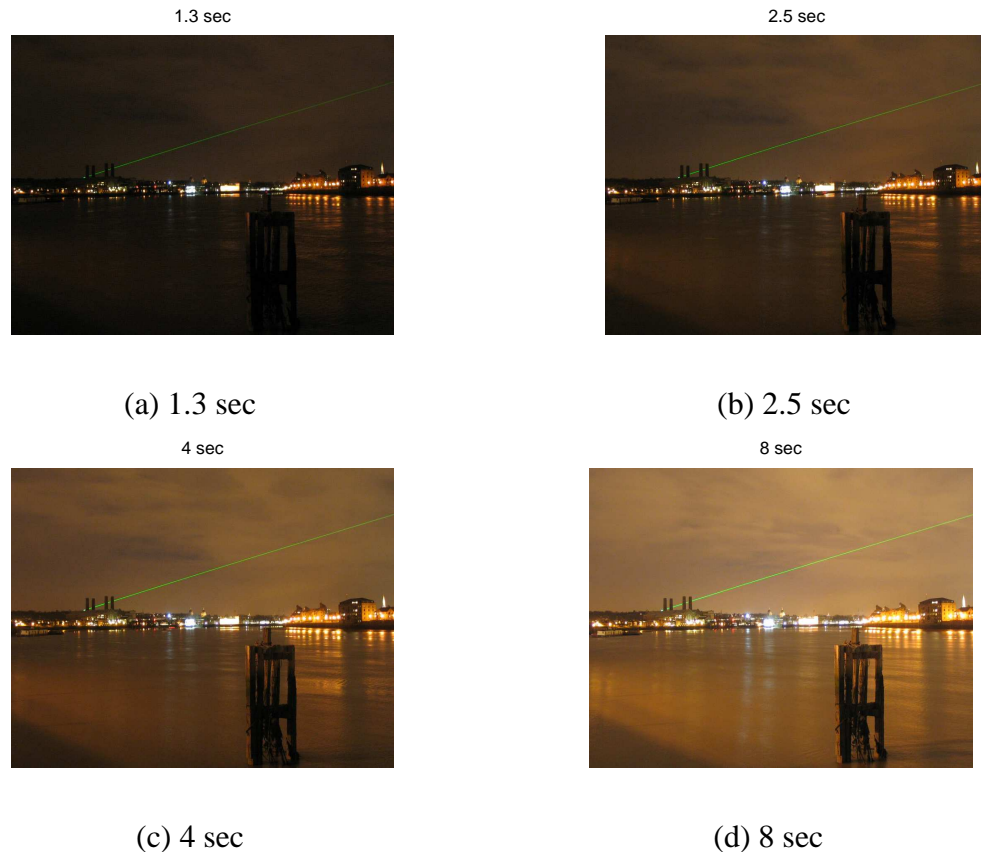
Figure 1.2: Photos with different shutter speed to overcome insufficient measurements [2].

The gantry speed of X-ray computed tomography (CT) is usually 330-400 milliseconds (ms) per rotation [98]. This is enough to acquire a thorax/abdomen image without motion blur as patients hold their breath (usually no more than 20 seconds). However, for cardiac studies, heart-beat rates are usually as fast as 90 or 100 beats-per-minute (bpm), but it usually takes 5-10 seconds to cover the entire heart. Therefore, cardiac CT must deal with heart motion. Another issue related to CT image quality is radiation dose. It is desirable to use a low dose in CT for the safety of patients. However, in some cardiac CT scans, only part of the dose (measurements) is used for imaging. To reduce dose, CT should collect fewer measurements and avoid motion blur.

Positron emission tomography (PET) collects gamma rays from radioactive materials that were administered to patients and uses them for imaging. However, PET usually

requires 3-7 minutes to acquire images per bed position or for each field of view [64]. Since the human breathing cycle is usually about 5 seconds, PET images can have heart motion artifacts as well as respiratory motion artifacts.

Magnetic Resonance Imaging (MRI) collects k-space data, but each k-space readout in short TR scans usually takes a few milliseconds (ms) [70]. Since it can take seconds to scan the full k-space for a 2D slice, cardiac and abdominal imaging may contain blurring and ghosting artifacts. This innate limitation of a MR image acquisition restricts the spatial and temporal resolution of MR imaging [91].

There are many medical applications with different imaging modalities that require long image acquisition times for better-quality images while patient motion is inevitable during the scan. Therefore, a proper strategy to deal with motion is crucial for these applications.

1.3 Strategies for motion in medical imaging

There are several ways to treat motion in medical imaging [64]. One way is to ignore motion and reconstruct an image from all measured data [59]. Figure 1.3 (c) shows an example of penalized weighted least square (PWLS) PET image reconstruction with all 1 million (M) counts from 8 motion phases, without motion compensation. In comparison to the true image in Figure 1.3 (a), it exhibits blur near the diaphragm and heart areas due to motion. This 'ungated' image reconstruction method is used frequently in clinical PET imaging.

For periodic motion, one can "gate" measurements according to motion, *i.e.*, to collect partial data at the same phase of heart or respiratory motion. Figure 1.4 illustrates respiratory gating with 8 gates. A gating method aggregates measurements at the same phase of motion to reduce motion artifacts. However, gating reduces SNR since it discards

TRUE

PWLS: 125K counts w/o motion

(a) TRUE

(b) PWLS w/ 125K counts

PWLS: 1M counts w/ motion

PWLS: 1M counts w/o motion

(c) PWLS w/ 1M counts and w/ motion

(d) PWLS w/ 1M counts and w/o motion
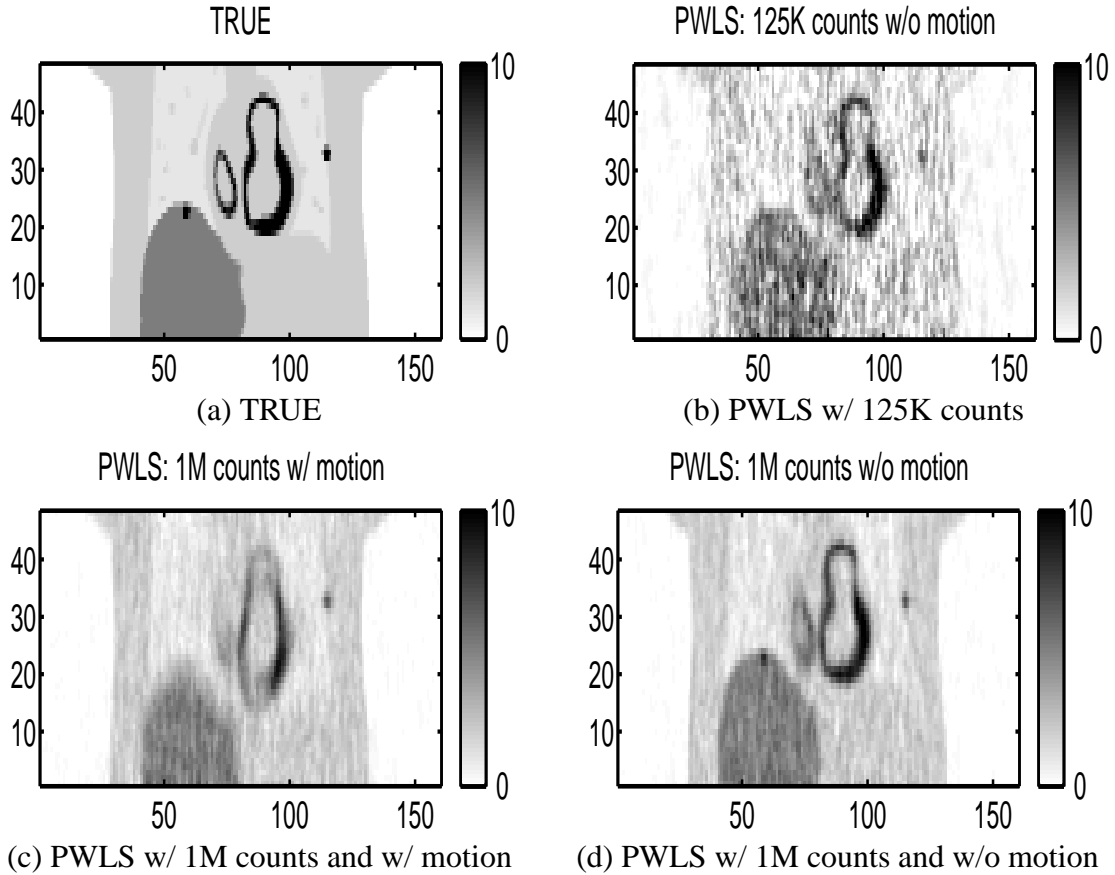
Figure 1.3: PWLS reconstructed PET images with different measurement counts and with/without motion (Coronal views of 3D images).

data (7/8 of the total measurements in Figure 1.4). Figure 1.3 (b) shows an example of the reconstructed image with 1/8 of measurements, *i.e.*, 125 thousand (K) counts, out of 1 million (M) counts. Gating reduces the blur near the diaphragm, but it also produces a low SNR image. This 'gated' image reconstruction has been investigated for many different medical imaging modalities such as PET [40, 62, 109], CT [10, 77], SPECT [71], and MRI [3]. Gating is based on signals such as an electrocardiogram (ECG) [3], video-camera based motion detectors [62], pneumatic respiratory bellows [45], and collected data itself [39].

Temporal relationships between image frames can be exploited to improve image quality by using 4D models for image sequences and temporal regularizers [49, 67]. Note that
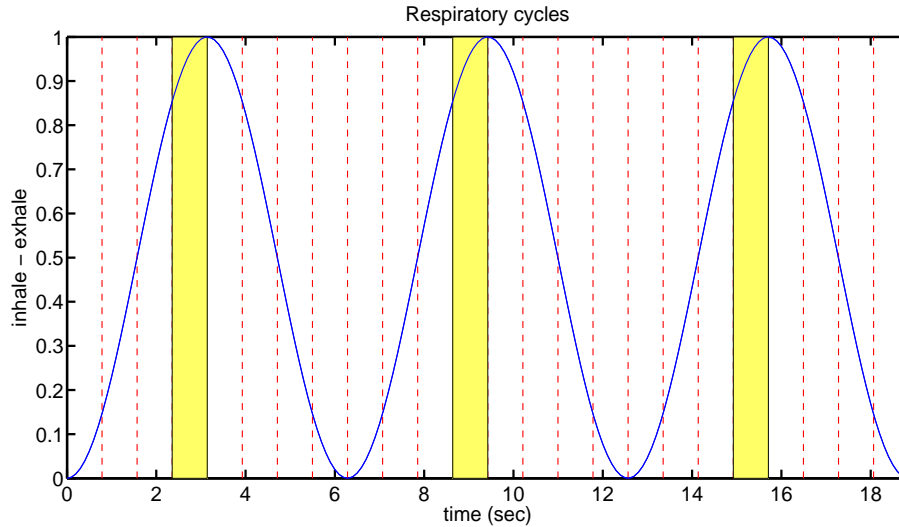
Figure 1.4: An example of a respiratory gating. A gating method only collects measurements at the same phase of motion (shaded areas).

these methods may not use any explicit motion deformations.

Motion-compensated image reconstruction (MCIR) is a method to exploit all measurements with motion information so that one may achieve both better signal-to-noise ratio (SNR) and less motion-blurring [5, 6, 14, 19, 29, 35, 46, 52, 53, 57, 69, 75, 100, 103]. In this way, we can obtain the advantages of both gated and ungated methods. Figure 1.3 (d) shows an 'oracle' reconstructed image that uses all measurements (1M counts) and eliminates motion artifacts by using a perfect model. This figure shows the 'gold standard' of a reconstructed image and illustrates that using motion compensation can improve the image quality. MCIR methods are the focus of this dissertation.

1.4 Contributions of this dissertation

MCIR methods have been investigated to improve the reconstructed image quality *and* to reduce motion artifacts. Many medical imaging applications with different imaging modalities can benefit from them. Since most medical imaging modalities in some applications have suffered from insufficient measurements and motion artifacts due to their

long image acquisition time, MCIR may aid in improving the reconstructed image quality in terms of SNR and motion blur [14, 35, 52, 53, 57, 75]. MCIR methods can also improve patient care as they can reduce an unnecessary scanning time or a harmful radiation dose [100].

Recently many different MCIR models have been proposed and investigated [25, 34, 35, 46, 57, 114] not only in medical imaging research, but also for super resolution (SR) research. They improved the quality of reconstructed images significantly compared to ungated and gated image reconstruction methods. However, there are also many unanswered questions about MCIR methods.

First of all, how can we obtain reasonable nonrigid motion estimates? Many medical imaging applications require nonrigid motion information since human organ is nonrigid [50]. However, estimating nonrigid motion is *ill-posed* [18] and usually requires motion priors to regularize. Even though nonrigid image registration methods have been investigated extensively [18], not many have been used in MCIR methods. The usual choice for motion regularization in MCIR has been a quadratic or an elastic penalty [35, 52, 53, 57, 75]. This dissertation proposes two kinds of motion regularizers. One is a motion regularizer that encourages local invertibility of deformations [13–15]. This method is fast and memory-efficient, so it is suitable for MCIR methods, which usually involve more than two image frames. Some medical imaging modalities such as CT provide indirect information about tissue rigidity that can be used as a motion prior since we know that rigid tissues such as bone can only move rigidly. However, such rigid motion priors may sometimes cause conflicts with priors on the smoothness or the local invertibility of deformations. This dissertation proposed a method to relax our proposed motion invertibility regularizer so that it can be used with a rigid motion regularizer without such conflicts [17].

Secondly, among many MCIR models which ones should we choose? MCIR models differ in terms of how they incorporate motion information into the image reconstruction framework. Even though they have been well-studied separately, there has been less attention to comparing different MCIR methods. Asma *et al.* compared two different MCIR models, but the analysis used a conventional kappa approximation [24] for the noise comparison so it was limited [5]. This dissertation compares three different MCIR models for the *regularized* case. Since MCIR methods experience resolution changes for nonrigid motion [96], it is important to match the spatial resolution of MCIR methods. For given motion, we extend a regularization design for uniform spatial resolution [24] to three different MCIR models. Based on the spatial regularization designs, we compare the statistical properties of MCIR methods [14, 16].

Lastly, what would happen to joint MCIR methods with different motion regularizers? Our theoretical comparison of different MCIR methods in this dissertation is limited since we assume given nonrigid motion. Analysis based on known motion is still useful since there are many multimodal imaging applications where we can obtain motion information separately such as PET/CT [53, 75] and PET/MR. However, there are also many applications with unknown nonrigid motion so joint MCIR methods are necessary to estimate motion information simultaneously. In SR problems, there has been some research on the performance analysis with unknown global translation motion [78, 79]. Even though it would be very beneficial to analyze the theoretical performance of MCIR, it is very challenging to deal with nonrigid motion in this analysis. As an initial step, this dissertation reports a simulation comparison of MCIR methods with different motion regularizers [14].

1.5 Outline of the dissertation

This dissertation investigates the motion aspects of MCIR models.

Chapter 2 describes a mathematical framework for incorporating motion models in medical imaging. Three existing MCIR models are considered: post-reconstruction motion correction (PMC) [34, 46], motion-compensated temporal regularization (MTR) [57, 114], and a parametric motion model (PMM) [25, 35],

Chapter 3 investigates sufficient conditions for ensuring the local invertibility of estimated deformations and proposes a fast and memory-efficient motion regularizer based on them [13, 15]. We compare this proposed method to a conventional Jacobian penalty [41, 47].

Chapter 4 elaborates on resolving conflicts between a proposed motion invertibility regularizer [15] and a rigid motion regularizer of rigid tissues [56, 84, 93] near the sliding area of the diaphragm. This chapter proposes to relax a motion invertibility regularizer by using a Geman-type function [17, 26].

Chapter 5 compares the statistical properties of different MCIR methods with known, but possibly nonrigid, motion. Spatial regularizers for different MCIR methods are proposed to approximately provide uniform spatial resolution [16], extending [24].

Lastly, Chapter 6 shows preliminary simulation results of joint MCIR methods with XCAT 4D phantom images and lesions [88]. We compared MCIR methods with the proposed motion invertibility regularizer and with a conventional quadratic motion regularizer [14].

CHAPTER 2

Motion-compensated image reconstruction models

In the previous chapter, we reviewed strategies for dealing with motion artifacts in medical imaging. This chapter provides mathematical formulae for these strategies, that will be used for the rest of this dissertation. Ungated and gated image reconstruction models and their cost functions will be presented. Three existing MCIR models and their cost functions will also be listed. The models of this chapter are general enough to represent different medical imaging modalities, but more specific assumptions will be made in other chapters when necessary.

2.1 Mathematical models

2.1.1 Measurement model

Let t_m denote the time of the mth "scan," *i.e.*, the mth frame in a gated study or in a video sequence. We assume that the measurements are related to the object $\boldsymbol{f}_m = \{f(\cdot, t_m)\}$ linearly as follows:

$$\boldsymbol{y}_m = \boldsymbol{A}_m \boldsymbol{f}_m + \boldsymbol{\epsilon}_m, \qquad m = 1, \ldots, M \qquad (2.1)$$

where $\boldsymbol{y}_m$ denotes the measurements for the mth frame, $\boldsymbol{A}_m$ denotes the system model for the mth frame , $\boldsymbol{\epsilon}_m$ denotes noise, and M is the number of gates or frames. We assume

that the object $\boldsymbol{f}_m$ and measurement $\boldsymbol{y}_m$ are motion-free, *i.e.*, the object does not move during the mth scan (gate or frame). We allow the system model $\boldsymbol{A}_m$ to possibly differ for each frame to accommodate systems that rotate such as gated SPECT or CT or that can otherwise change sampling properties dynamically such as MRI. We can also assume that $\boldsymbol{A}_m = \boldsymbol{A}_0, \; \forall m$ for cases such as an attenuation corrected PET scan or a video sequence.

2.1.2 Deformation model

In this thesis, we use nth-order B-spline based deformations for our theoretical results in Chapter 3 and 4. We use cubic B-spline based motion for all simulations involving motion estimation in Chapter 3, 4 and 6.

A 3D nonrigid transformation $\underline{T} : \mathbf{R}^3 \to \mathbf{R}^3$ can be written

$$\underline{T}(\underline{r}) = \underline{r} + \underline{d}(\underline{r}), \tag{2.2}$$

where $\underline{r} = (x, y, z)$ and $\underline{d}(\underline{r})$ is the deformation. We model the 3D deformation (or displacement) $\underline{d} = (d^x, d^y, d^z)$ using a tensor product of nth-order B-splines as follows:

$$d^q(\underline{r}; \underline{\alpha}) = \sum_{ijk} \alpha^q_{ijk} \beta\left(\frac{x}{m_x} - i\right) \beta\left(\frac{y}{m_y} - j\right) \beta\left(\frac{z}{m_z} - k\right), \tag{2.3}$$

where $q \in \{x, y, z\}$, m_q is knot spacing in the q direction and β is a nth-order B-spline basis.

2.1.3 Image interpolation model

We parametrize the object $f_m(\underline{r}) \triangleq f(\underline{r}, t_m)$, for $\underline{r} \in \mathbf{R}^3$, with a basis function ω as follows:

$$f_m(\underline{r}) = \sum_{k=1}^{K} c_{mk}\omega(\underline{r} - \underline{l}_k) \tag{2.4}$$

where K is the number of basis functions and $\underline{l}_k \in \mathbf{R}^3$ is the center of the kth basis function.

Then, for a warp $\underline{r} \mapsto \underline{r} + \underline{d}(\underline{r}; \underline{\alpha})$ that is parameterized by $\underline{\alpha}$, a warped version of the image f_m can be represented as

$$f_m(\underline{r} + \underline{d}(\underline{r}; \underline{\alpha})) = \sum_{k=1}^{K} c_{mk}\omega(\underline{r} + \underline{d}(\underline{r}; \underline{\alpha}) - \underline{l}_k). \tag{2.5}$$

For convenience, we rewrite (2.5) in matrix-vector notation. Let $\boldsymbol{c}_m = (c_{m1}, \ldots, c_{mK})$ denote a vector of the image coefficients for the mth frame, and $\boldsymbol{f}_m = (f_m(\underline{r}_1), \ldots, f_m(\underline{r}_N))$ denote a vector of a discretization of $f_m(\underline{r})$ with N samples at locations $\{\underline{r}_n\}$. Then a warped image vector $\{f_m(\underline{r}_n + \underline{d}(\underline{r}_n; \underline{\alpha}))\}$ can be represented in the matrix form

$$\breve{\boldsymbol{T}}(\underline{\alpha})\boldsymbol{c}_m \tag{2.6}$$

where the $N \times K$ warping matrix $\breve{\boldsymbol{T}}(\underline{\alpha})$ has elements

$$[\breve{\boldsymbol{T}}(\underline{\alpha})]_{nk} = \omega(\underline{r}_n + \underline{d}(\underline{r}_n; \underline{\alpha}) - \underline{l}_k). \tag{2.7}$$

In our simulation, we used a tensor-product of cubic B-spline image bases for ω, with $\underline{l}_k = \underline{r}_k$.

We assume that $\underline{d}(\underline{r}_n; \underline{\alpha})$ is defined by the B-spline deformation model (2.3) in some chapters. However, the analysis in Chapter 5 does not assume any motion model for the given nonrigid motion information. For simplicity, the model (2.5) ignores any intensity changes due to local volume changes.

2.1.4 Warp model

For notational convenience, we define a warp $\breve{\boldsymbol{T}}_{j,i}$ from the coefficients of image $\boldsymbol{f}_i$ to the image $\boldsymbol{f}_j$ based on the vector-matrix notation (2.6) as follows:

$$\boldsymbol{f}_j = \breve{\boldsymbol{T}}_{j,i}\boldsymbol{c}_i, \quad i, j = 1, \cdots, M. \tag{2.8}$$

For applications with periodic motion, we can additionally define $\boldsymbol{f}_{M+1} \triangleq \boldsymbol{f}_1$ and $\breve{\boldsymbol{T}}_{M+1,M} \triangleq \breve{\boldsymbol{T}}_{1,M}$. We also denote that

$$\breve{\boldsymbol{T}}_0 = \breve{\boldsymbol{T}}_{i,i}, \quad i = 1, \cdots, M. \tag{2.9}$$

For some parts of our analysis, we use the image to image warp $\boldsymbol{T}_{j,i}$ defined such that

$$\boldsymbol{f}_j = \boldsymbol{T}_{j,i}\boldsymbol{f}_i, \quad i,j = 1, \cdots, M. \tag{2.10}$$

This matrix can be approximated by

$$\boldsymbol{T}_{j,i} \approx \breve{\boldsymbol{T}}_{j,i}\breve{\boldsymbol{T}}_0^{-1} \tag{2.11}$$

where using $\breve{\boldsymbol{T}}_0^{-1}$ suffices to choose $\underline{r}_k = \underline{l}_k$ and $\breve{\boldsymbol{T}}_0^{-1}$ with B-spline bases ω are well-defined [105, 106].

For some parts of the analysis, we assume that the given warps $\boldsymbol{T}_{j,i}$ are invertible, symmetric and transitive, *i.e.*,

$$\boldsymbol{T}_{j,i}^{-1} = \boldsymbol{T}_{i,j}, \quad \forall\, i,j \tag{2.12}$$

$$\boldsymbol{T}_{j,i} = \boldsymbol{T}_{j,j-1}\boldsymbol{T}_{j-1,j-2}\cdots\boldsymbol{T}_{i+1,i}, \quad \forall\, j > i. \tag{2.13}$$

We let $|\nabla\boldsymbol{T}_{j,i}|$ denote the determinant of the Jacobian matrix for the transformation $\underline{r} + \underline{d}_{j,i}(\underline{r};\underline{\alpha})$ in (2.7) for notational convenience.

2.2 Motion-compensated image reconstruction

2.2.1 Cost function and optimization

Cost functions for MCIR methods usually contain measurements $\boldsymbol{y}_m$, unknown images $\boldsymbol{f}_m$, and known or unknown motion parameterized by $\underline{\alpha}_m$. A typical form of the cost functions for MCIR methods is

$$\Psi(\boldsymbol{y}_1, \cdots, \boldsymbol{y}_M | \boldsymbol{f}_1, \cdots, \boldsymbol{f}_M, \underline{\alpha}_1, \cdots, \underline{\alpha}_M). \tag{2.14}$$

In this thesis, we use the Conjugate Gradient (CG) optimization method to minimize (2.14) with respect to $\boldsymbol{f}_1, \ldots, \boldsymbol{f}_M, \underline{\alpha}_1, \ldots, \underline{\alpha}_M$. We use an alternating minimization method that minimizes (2.14) with respect to $\boldsymbol{f}_1, \ldots, \boldsymbol{f}_M$ and $\underline{\alpha}_1, \ldots, \underline{\alpha}_M$ alternatively,

i.e.,

start loop

$$(\hat{\underline{\alpha}}_1, \cdots, \hat{\underline{\alpha}}_M) = \underset{\underline{\alpha}_1, \cdots, \underline{\alpha}_M}{\operatorname{argmin}} \Psi(\boldsymbol{y}_1, \cdots, \boldsymbol{y}_M | \hat{\boldsymbol{f}}_1, \cdots, \hat{\boldsymbol{f}}_M, \underline{\alpha}_1, \cdots, \underline{\alpha}_M)$$

$$(\hat{\boldsymbol{f}}_1, \cdots, \hat{\boldsymbol{f}}_M) = \underset{\boldsymbol{f}_1, \cdots, \boldsymbol{f}_M}{\operatorname{argmin}} \Psi(\boldsymbol{y}_1, \cdots, \boldsymbol{y}_M | \boldsymbol{f}_1, \cdots, \boldsymbol{f}_M, \hat{\underline{\alpha}}_1, \cdots, \hat{\underline{\alpha}}_M)$$

end loop.

The loop is repeated until the estimates "converge", *i.e.*, change less than some small threshold between subsequent iterations. The step size in the CG method is determined by the first step of Newton's method. See Appendix A for details.

2.2.2 Motion-compensated image reconstruction models

We investigated three different types of MCIR methods in this dissertation: post-reconstruction motion correction (PMC) [34, 46], parametric motion model (PMM) [14, 25, 35, 52, 53, 75, 100] and motion-compensated temporal regularization (MTR) [57, 114]. Here we explain how each MCIR method alters (2.14).

PMC decouples images and motion in (2.14) as follows:

$$\sum_{m=1}^{M} \Psi_1(\boldsymbol{y}_m | \boldsymbol{f}_m) \tag{2.15}$$

$$\Psi_2(\hat{\boldsymbol{f}}_1, \cdots, \hat{\boldsymbol{f}}_M | \underline{\alpha}_1, \cdots, \underline{\alpha}_M). \tag{2.16}$$

We assume that measurements $\boldsymbol{y}_m$ are independent from each other. Ψ_1 is a cost function that estimates an image for each gate $\boldsymbol{f}_m$ from each measurement $\boldsymbol{y}_m$. The gated image reconstruction estimator $\hat{\boldsymbol{f}}_m$ will be applied to the cost function Ψ_2 that estimates warps $\mathcal{T}_{1,m}$ from mth frame to 1st frame. We chose frame 1 for PMC image reconstruction without loss of generality and a warp $\mathcal{T}_{1,m}$ depends on some parameters $\underline{\alpha}_m$. Therefore,

the PMC estimator becomes an average of the warped estimated images from all frames:

$$\hat{\boldsymbol{f}}_{\mathrm{PMC}} = \frac{1}{M} \sum_{m=1}^{M} \hat{\mathcal{T}}_{1,m} \hat{\boldsymbol{f}}_m$$

where $\hat{\mathcal{T}}_{1,m}$ depends on $\hat{\underline{\alpha}}_m$.

PMM substitutes $\boldsymbol{f}_m$ with $\mathcal{T}_{m,1}\boldsymbol{f}_1$ in (2.14) where $\mathcal{T}_{m,1}$ depends on $\underline{\alpha}_m$. Therefore, the PMM cost function becomes

$$\Psi(\boldsymbol{y}_1, \cdots, \boldsymbol{y}_M | \boldsymbol{f}_1, \underline{\alpha}_1, \cdots, \underline{\alpha}_M). \tag{2.17}$$

The cost function (2.15) does not depend on motion $\underline{\alpha}_m$. We could estimate images and then motion sequentially. In contrast, the estimator of an image $\hat{\boldsymbol{f}}_1$ in (2.17) depends on the estimator of motion $\hat{\underline{\alpha}}_1, \cdots, \hat{\underline{\alpha}}_M$ and vice versa. Therefore, images and motion have to be estimated simultaneously.

Lastly, MTR decouples motion parameters and measurements in the cost function (2.14) as follows:

$$\sum_{m=1}^{M} \Psi_1(\boldsymbol{y}_m | \boldsymbol{f}_m) + \Psi_2(\boldsymbol{f}_1, \cdots, \boldsymbol{f}_M, \underline{\alpha}_1, \cdots, \underline{\alpha}_M). \tag{2.18}$$

Since Ψ_2 in the MTR cost function couples images and motion, images and motion have to be estimated simultaneously just like the PMM case. A typical choice for Ψ_2 is

$$\zeta \sum_{m=1}^{M} \| \boldsymbol{f}_{m+1} - \mathcal{T}_{m+1,m} \boldsymbol{f}_m \|_2^2$$

where $\mathcal{T}_{m+1,m}$ depends on $\underline{\alpha}_m$.

A MCIR cost function (2.14) can be simplified according to each MCIR method. Chapter 5 studies the relationship between different MCIR estimators with given motion. Chapter 6 compares different MCIR methods in joint image reconstruction and nonrigid motion estimation by simulations. The analyses in Chapter 5 aid the understanding of the results with more complicated joint MCIR models.

2.2.3 Regularizers

Estimating $\boldsymbol{f}_1, \ldots, \boldsymbol{f}_M, \underline{\alpha}_1, \ldots, \underline{\alpha}_M$ from $\boldsymbol{y}_1, \ldots, \boldsymbol{y}_M$ based on a cost function (2.14) is usually highly *ill-posed*. One of the typical ways to resolve this issue is to introduce regularizers for images and motion:

$$\Psi(\boldsymbol{y}_1, \cdots, \boldsymbol{y}_M | \boldsymbol{f}_1, \cdots, \boldsymbol{f}_M, \underline{\alpha}_1, \cdots, \underline{\alpha}_M) + \eta_R \mathcal{R}_R(\boldsymbol{f}_1, \cdots, \boldsymbol{f}_M) + \eta_M \mathcal{R}_M(\underline{\alpha}_1, \cdots, \underline{\alpha}_M).$$
(2.19)

A motion regularizer $\mathcal{R}_M$ is usually based on motion priors such as smoothness of warps, motion invertibility, tissue rigidity and so on. Chapter 3 and 4 describe two motion regularizers $\mathcal{R}_M$ based on two different motion priors: motion invertibility and tissue rigidity/sliding. They can also be used for general image registration problems.

A typical spatial regularizer is a quadratic regularizer based on the assumption (or image prior) that the image is smooth. Nonquadratic spatial regularizers are also frequently used to preserve edges. The spatial resolution properties of an image reconstruction method depend on the relationship between Ψ and $\mathcal{R}_R$, not on $\mathcal{R}_R$ alone. There has been several efforts to design spatial regularization methods that approximately provide uniform spatial resolution. This regularization design depends on measurements, *i.e.*,

$$\mathcal{R}_R(\boldsymbol{f}_1, \cdots, \boldsymbol{f}_M | \boldsymbol{y}_1, \cdots, \boldsymbol{y}_M).$$

Chapter 5 extends such methods to consider motion estimates, *i.e.*,

$$\mathcal{R}_R(\boldsymbol{f}_1, \cdots, \boldsymbol{f}_M | \boldsymbol{y}_1, \cdots, \boldsymbol{y}_M, \hat{\underline{\alpha}}_1, \cdots, \hat{\underline{\alpha}}_M)$$
(2.20)

to improve spatial resolution uniformity.

With the knowledge of simplified MCIR cost functions and estimators, motion regularizer $\mathcal{R}_M$ and spatial regularizer $\mathcal{R}_R$ in (2.20), Chapter 6 reports the results of simulations for joint image reconstruction and nonrigid motion estimation based on (2.19) with the proposed motion regularizer of Chapter 3.

CHAPTER 3

Regularization for nonrigid motions: invertibility [1]

One of the important issues in motion-compensated image reconstruction is the motion estimation problem. Image registration has been a core tool not only in motion-compensated image reconstruction, but also in many medical imaging applications. Image fusion of structural and functional images requires image matching from one to another. Several image reconstruction schemes for MR, PET and CT incorporate motion correction or joint estimation of motion into the reconstruction process to improve image quality [34, 51, 52, 57, 75, 76]. Radiation treatments may be able to target cancer cells more accurately through motion correction [111, 112]. Rigid or affine transformations can provide fast and reliable image registration for relatively small changes. However, most of the human body does not conform to a rigid or affine approximation [18]. Lamare *et al.* [51] used affine image registration for respiratory motion correction, but reported that it was sufficient only for a single organ and associated lesions. Effective motion correction usually requires nonrigid image registration, which enables more flexible matching of local details between two images than rigid registration.

There are many methods for nonrigid image registration [18, 33]. Since Szeliski *et al.* [95], B-spline bases have been used frequently for nonrigid image registration be-

---

[1]This chapter is based on [13, 15].

cause locally supported basis function expansions are easier to solve computationally than PDEs and B-splines have the properties of smoothness, compact support, fast interpolation schemes and hierarchical structure for multi-resolution [33, 48, 104]. However deformations with high degrees of freedom can lead to unrealistic transformation results such as folding in the absence of appropriate constraints [18].

There have been some efforts to regularize nonrigid image registration based on B-splines by making certain reasonable assumptions. Rueckert *et al.* [86] penalized the bending energy of the deformation directly, assuming that the local deformation of tissues should be smooth. Sorzano *et al.* [92] proposed a regularizer based on the gradients of the divergence and the curl of the displacement field. Rohlfing *et al.* [81] used an incompressibility constraint: the Jacobian determinant of a transformation should be unity, assuming that local deformations are volume preserving. They applied this method after making an initial affine transformation. See [33] for other methods for constraining the transformation.

Another reasonable constraint is to impose local invertibility of the nonrigid transformation to ensure that image registration is topology-preserving or diffeomorphic.

One way to ensure local invertibility is to require the Jacobian determinant of the transformation to be positive everywhere, either as a hard constraint or by a penalty method [47]. However most such approaches constrain the Jacobian determinant of a transformation only at each discrete voxel grid point, so local invertibility is not strictly guaranteed on the whole continuous domain. Recently, Sdika [87] described a condition involving the *gradient* of the Jacobian determinant that encourages the local invertibility to be achieved everywhere even though that condition is invoked only at each discrete grid point. However, compared to unregularized image registration, calculating the Jacobian determinant or its gradient significantly increases computation time due to additional

B-spline interpolations of the partial derivatives of a deformation.

Ensuring invertibility is somewhat easier when using 1st-order B-spline bases for deformations. Musse *et al.* [61] derived elegant linear constraints that provide necessary and sufficient conditions to ensure that the Jacobian determinant values of such transformations are positive everywhere. However, that 2D approach was restricted to 1st-order B-spline deformations. Karacali *et al.* [38] proposed a method to regularize 2D and 3D deformations to ensure that 1st-order B-splines are topology-preserving. Noblet *et al.* [68] generalized [61] for 3D B-spline deformations and illustrated their method with 1st-order B-splines, but enforcing the constraints requires much higher computation than regularization based on bending energy.

Lastly, one can ensure local invertibility by imposing sufficient conditions that are simpler than the necessary conditions. Choi *et al.* [11] suggested box constraints for cubic B-spline deformation coefficients that ensure invertibility, but those sufficient conditions preclude large deformations. Rueckert *et al.* [85] concatenated many transformations based on those box constraints to achieve large deformations. Rohde *et al.* [80] suggested a sufficient condition for local invertibility, derived using Neuman series for a transformation model that uses a sum of deformations. Motivated by [80], Kim *et al.* [41–43] suggested similar sufficient conditions for 3D transformations based on cubic B-splines and implemented a constrained minimization algorithm using Dykstra's cyclic projection method. We recently extended Kim's sufficient conditions for local invertibility of deformations so that we can use nth-order B-spline bases and so we can also assign the upper bound on the Jacobian determinant value independently from the lower bound choice. We implemented it with a simple and fast quadratic-like penalty function [13, 15].

This chapter elaborates on the method based on the proposed sufficient condition for the local invertibility of deformations [13, 15] and and compares it empirically with other

regularization methods based on existing sufficient conditions for the local invertibility of deformations as well as with the traditional Jacobian penalty method that uses a discrete grid [41, 47].

3.1 Background

3.1.1 Mathematical model for nonrigid registration

The goal in image registration is to estimate the deformation coefficients $\underline{\alpha} = \{\alpha_{i,j,k}^q\}$ in (2.3) by maximizing a similarity metric Ψ:

$$\hat{\underline{\alpha}} = \arg \max_{\underline{\alpha}} \Psi[g(\cdot), f(\underline{T}(\cdot; \underline{\alpha}))] \tag{3.1}$$

where $g(\underline{r})$ and $f(\underline{r})$ denote two 3D images.

To help stabilize the estimation, and to have physically plausible deformations, often we would like to ensure that the estimated coefficients $\hat{\underline{\alpha}}$ in (2.2) correspond to a diffeomorphic transformation $\underline{T}$. The methods in this chapter are applicable to any similarity metric; for a survey of such metrics, see [32]. Section IV focuses on the l_2 similarity metric for registering thorax CT images at different inhalations for the purpose of radiation therapy planning and monitoring.

3.1.2 Invertibility and diffeomorphic transformations

Invertibility of a nonrigid transformation $\underline{T}$ is a necessary condition for it to be diffeomorphic. $\underline{T}$ is diffeomorphic if both $\underline{T}$ and $\underline{T}^{-1}$ are continuously differentiable. If we use a B-spline basis with $n \geq 2$ in (2.2), then $\underline{T}$ is continuously differentiable. (Musse *et al.* [61] addressed the case where $n = 1$.) By the implicit function theorem, if the Jacobian matrix of $\underline{T}$, denoted $\nabla \underline{T}$, is invertible everywhere, then near every point there exists a unique continuously differentiable local inverse. The determinant of the Jacobian for $\underline{T}$,

denoted $|\nabla \underline{T}|$, must be non-zero for diffeomorphic nonrigid image registration. Also for $\underline{T}$ to be orientation preserving, we want $|\nabla \underline{T}| > 0$.

Unfortunately, the condition $|\nabla \underline{T}| > 0$ everywhere does not by itself ensure that $\underline{T}$ is globally one-to-one. One way to ensure that $\underline{T}$ is invertible globally is to ensure that transformation maps the boundary of the domain onto itself [61, 68]. However, we do not enforce such boundary conditions in here because the field of view for thorax inhale and exhale CT images does not contain the whole body and there is usually missing anatomy in the superior-inferior directions.

3.1.3 Related work

The goal of diffeomorphic nonrigid image registration with the parametric representation of deformation (2.3) is to maximize the similarity metric (3.1) subject to the constraint

$$\underline{\alpha} \in C_0 \triangleq \{\underline{\alpha} : |\nabla \underline{T}(\underline{r}; \underline{\alpha})| > 0,\ \forall \underline{r} \in \mathbf{R}^3\}. \tag{3.2}$$

In general this is an impractical constraint except when using linear deformation models [38, 61, 68] because $\underline{r} \in \mathbf{R}^3$ so there are uncountably many conditions. One way to simplify (3.2) is to replace the "$\forall \underline{r}$" requirement with a set of voxel grid points [47, 87]:

$$C_1 \triangleq \{\underline{\alpha} : |\nabla \underline{T}(\underline{r}; \underline{\alpha})| > 0,\ \underline{r} \in \text{grid points}\}. \tag{3.3}$$

However, because $C_0 \subset C_1$, this does not guarantee local invertibility *between* grid points. Nevertheless the smoothness of B-spline bases helps regularize C_1 so using the constraint C_1 often provides fairly good results [47]. However, computing $|\nabla \underline{T}(\underline{r}; \underline{\alpha})|$ at all the grid points is computationally expensive.

Simplifying the condition $|\nabla \underline{T}(\underline{r}; \underline{\alpha})| > 0$ over $\mathbf{R}^3$ always involves smaller sets than C_0. Choi *et al.* [11] found box constraints for cubic B-spline deformation coefficients that

ensure invertibility:

$$C_2 \triangleq \{\underline{\alpha} : |\alpha_{i,j,k}^q| < m_q/K, \ \forall i, j, k\}, \tag{3.4}$$

where $K \approx 2.05$ in 2D and $K \approx 2.48$ in 3D. The set C_2 provides a sufficient condition for local invertibility because $C_2 \subset C_0$. However, C_2 is a very restrictive constraint set that allows only very small deformations. To achieve large deformations, Rueckert *et al.* [85] composed several transformations that each satisfied this condition.

Kim *et al.* [41–43] suggested a sufficient condition for ensuring invertibility of cubic B-spline deformations that allows a larger family of deformations. Instead of restricting the absolute values of the coefficients as in (3.4), this condition limits the *differences* of adjacent B-spline coefficients:

$$C_3 \triangleq \bigcap_{q \in \{x,y,z\}} \{\underline{\alpha} : |\alpha_{i+1,j,k}^q - \alpha_{i,j,k}^q| < m_q k_q, \quad |\alpha_{i,j+1,k}^q - \alpha_{i,j,k}^q| < m_q k_q,$$

$$|\alpha_{i,j,k+1}^q - \alpha_{i,j,k}^q| < m_q k_q, \ \forall i, j, k\}, \tag{3.5}$$

where $k_x + k_y + k_z < 1$. Although $C_3 \subset C_0$, this sufficient condition only allows large deformations with fairly small Jacobian determinant values. In particular, one can show that $1 - (k_x + k_y + k_z) \leq |\nabla \underline{T}(\underline{r}; \underline{\alpha})| \leq (1 + k_x)(1 + k_y)(1 + k_z) + (1 + k_x)k_y k_z + k_x(1 + k_y)k_z + k_x k_y(1 + k_z) \ \forall \underline{\alpha} \in C_3$ [41–43]. This means that C_3 does not allow acute volume changes locally. This is because the upper bound on the Jacobian determinant is determined by the lower bound design. For example, if we choose $k_q = 1/3$ so that the lower bound for the Jacobian determinant $|\mathbf{J}|$ is 0, then the upper bound for the Jacobian determinant value would be automatically determined to $76/27 \approx 2.8148$ which is fairly small [41]. The section 3.2 provides new broader sets of sufficient conditions.

3.2   Local invertibility condition

3.2.1   Lemmas

We first extend Kim's sufficient conditions for local invertibility to overcome two limitations [13, 15]. Firstly, a nth-order B-spline basis ($n \geq 1$) can be used instead of cubic B-spline basis for deformation modeling. Secondly, the upper bound of Jacobian determinant can be designed independently from the lower bound of Jacobian determinant.

Lemma 3.1. *For concise notation, denote the Jacobian* $\mathbf{J} = \nabla \underline{T}$ *of a 3D transformation as*

$$\mathbf{J} = \mathbf{I} + \begin{pmatrix} x_1 & x_2 & x_3 \\ x_4 & x_5 & x_6 \\ x_7 & x_8 & x_9 \end{pmatrix}.$$

Then the corresponding determinant is given by

$$\begin{aligned} |\mathbf{J}| &= (1 + x_1)(1 + x_5)(1 + x_9) + x_2 x_6 x_7 + x_3 x_4 x_8 - (1 + x_1) x_6 x_8 \\ &\quad -(1 + x_5) x_3 x_7 - (1 + x_9) x_2 x_4. \end{aligned} \tag{3.6}$$

Suppose that the elements of the 3D Jacobian determinant satisfy $x_i \in I_i$, $i = 1, \ldots, 9$ *where* $I_i \subset \mathbf{R}$ *are compact intervals. Then* $|\mathbf{J}|$ *achieves its global maximum and minimum values over* $I = I_1 \times \cdots \times I_9$ *and those maximum and minimum values are achieved for a point* x_i^* *for which* $x_i^* \in \{\max I_i, \min I_i\}$ *for* $\forall i = 1, \ldots, 9$.

The Appendices have the proofs of these Lemmas. This Lemma implies that we can determine the global minimum and maximum of $|\mathbf{J}|$ over the compact set I "simply" by calculating the 2^9 possible values of $|\mathbf{J}|$ at the vertices of I. (It is trivial to apply this Lemma to 2D cases.)

Kim *et al.* provided a specific formula for the 'possible' maximum and minimum of $|\mathbf{J}|$ for given ranges of each x_i value using Karush-Kuhn-Tucker conditions [41]. We suggest

next a generalization using Lemma 3.1.

Lemma 3.2. *Suppose that* $|x_i| \leq k_{q_i} < \frac{1}{2}$ *where* $q_i = x$ *for* $i = 2, 3$, $q_i = y$ *for* $i = 4, 6$ *and* $q_i = z$ *for* $i = 7, 8$. *Also suppose that* $-k_{p_i} \leq x_i \leq K_{p_i}$ *where* $p_i = x$ *for* $i = 1$, $p_i = y$ *for* $i = 5$ *and* $p_i = z$ *for* $i = 9$. *Then* $\min |\mathbf{J}| = 1 - (k_x + k_y + k_z)$ *and* $\max |\mathbf{J}| = (1 + K_x)(1 + K_y)(1 + K_z) + (1 + K_x)k_y k_z + k_x(1 + K_y)k_z + k_x k_y(1 + K_z)$. *In other words,*

$$1 - (k_x + k_y + k_z) \leq |\mathbf{J}| \leq (1 + K_x)(1 + K_y)$$

$$\cdot (1 + K_z) + (1 + K_x)k_y k_z + k_x(1 + K_y)k_z$$

$$+ k_x k_y(1 + K_z). \tag{3.7}$$

Kim's proposition was restricted to the case where $K_x = k_x$, $K_y = k_y$, and $K_z = k_z$. To ensure local invertibility, $k_x + k_y + k_z$ should be less than 1, where each k_q is positive, so that the lower bound in (3.7) is positive.

Kim *et al.* showed a second proposition about the relationship between the first partial derivative of deformation and adjacent deformation coefficients for the cubic B-spline basis case [41]. We show next that this relation is also valid for general nth-order B-spline bases ($n \geq 1$). We also generalize the bounds used by Kim *et al.* with Lemma 3.2 [13,15].

Lemma 3.3. *If* $b_m \leq \alpha_{i+1,j,k}^q - \alpha_{i,j,k}^q \leq b_M$ *for* $\forall i, j, k$, *then* $\frac{b_m}{m_x} \leq \frac{\partial}{\partial x} d^q(\underline{r}) \leq \frac{b_M}{m_x}$ *for* $\forall \underline{r}$ *where* $q \in \{x, y, z\}$ *Similarly, if* $b_m \leq \alpha_{i,j+1,k}^q - \alpha_{i,j,k}^q \leq b_M$ *for* $\forall i, j, k$, *then* $\frac{b_m}{m_y} \leq \frac{\partial}{\partial y} d^q(\underline{r}) \leq \frac{b_M}{m_y}$ *and if* $b_m \leq \alpha_{i,j,k+1}^q - \alpha_{i,j,k}^q \leq b_M$ *for* $\forall i, j, k$, *then* $\frac{b_m}{m_z} \leq \frac{\partial}{\partial z} d^q(\underline{r}) \leq \frac{b_M}{m_z}$ *for* $\forall \underline{r}$ *respectively.*

This Lemma limits the range of values of the first derivative of $\underline{d}(\underline{r})$ over $\mathbf{R}^3$ by restricting the differences of adjacent deformation coefficients. Combined, Lemmas 3.2 and 3.3 show that one can obtain a transformation $\underline{T}$ that is everywhere locally invertible by

maximizing a similarity metric subject to constraints on the *differences* between adjacent deformation coefficients, as summarized in the following Theorem.

Theorem 3.4. *Suppose* $0 \leq k_q < \frac{1}{2}$ *for* $q \in \{x, y, z\}$. *Define:*

$$C_4 \triangleq \{\underline{\alpha} :- m_x k_x \leq \alpha_{i+1,j,k}^x - \alpha_{i,j,k}^x \leq m_x K_x,$$

$$- m_y k_y \leq \alpha_{i,j+1,k}^y - \alpha_{i,j,k}^y \leq m_y K_y,$$

$$- m_z k_z \leq \alpha_{i,j,k+1}^z - \alpha_{i,j,k}^z \leq m_z K_z,$$

$$|\alpha_{i+1,j,k}^q - \alpha_{i,j,k}^q| \leq m_q k_q \textit{ for } q = y, z,$$

$$|\alpha_{i,j+1,k}^q - \alpha_{i,j,k}^q| \leq m_q k_q \textit{ for } q = x, z,$$

$$|\alpha_{i,j,k+1}^q - \alpha_{i,j,k}^q| \leq m_q k_q \textit{ for } q = x, y, \forall i, j, k\}.$$

In (2.3), if $\underline{\alpha} \in C_4$ *then* $|\mathbf{J}|$ *satisfies the bounds in (3.7)* $\forall \underline{r} \in \mathbf{R}^3$. *Moreover, if* $k_x + k_y + k_z < 1$, *then the transformation (2.3) is locally invertible everywhere.*

This theorem applies to deformations based on any nth-order B-spline basis. We set the lower and upper bounds for $|\mathbf{J}|$ by setting appropriate k_q and K_q values for $q \in \{x, y, z\}$.

3.2.2   Restrictions

Theorem 3.4 establishes that $\underline{\alpha} \in C_4$ is a simple sufficient condition for local invertibility. However, C_4 does not allow all possible locally invertible deformations, *i.e.*, $C_4 \subset C_0$. Then one can ask how restrictive this sufficient condition is.

Although C_4 allows for acute volume expansion, it precludes acute volume shrinkage. Figure 3.1 illustrates this limitation for a 1D transformation. The desired transformation maps $[0.0 \, 0.6]$ to $[0.3 \, 0.6]$, *i.e.*, $T(x) = x + d(x)$ where $d(x) = 0.3 - x/2$ (acute volume shrinkage). This deformation belongs to C_0 because $-1 < \frac{\partial d(x)}{\partial x} < \infty$. However if we impose the sufficient condition $-0.33 < \frac{\partial d(x)}{\partial x}$, then Figure 3.1 shows that acute volume shrinkage is precluded because the minimum derivative of the transformation is 0.67. The

constrained transformation maps $[0\ 0.6]$ to $[0.3\ 0.7]$ instead of $[0.3\ 0.6]$. More generally, when we choose k_x, k_y and k_z subject to $k_x + k_y + k_z < 1$ to ensure invertibility, C_4 imposes restrictions for acute volume changes in each direction.
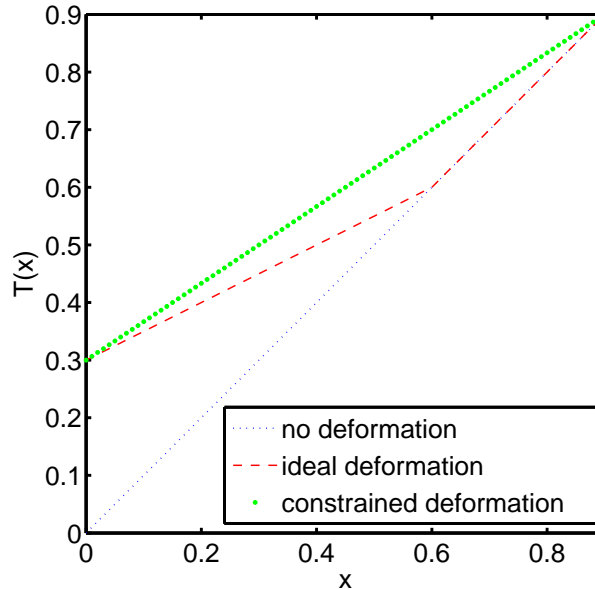
Figure 3.1: Illustration of limitation of C_4. The constrained transformation maps $[0\ 0.6]$ to $[0.3\ 0.7]$ instead of $[0.3\ 0.6]$.

The 2D case illustrates the solution space of C_4 in terms of Lemma 3.2. Lemma 3.2 is trivial for a 2D Jacobian determinant $|\mathbf{J}| = (1 + a)(1 + d) - bc$ where $\mathbf{J} = \begin{bmatrix} a & b \\ c & d \end{bmatrix}$. A deformation having a positive Jacobian determinant must satisfy $(1 + a)(1 + d) > bc$. We can introduce a free parameter k such that $|\mathbf{J}|$ is always positive if $(1 + a)(1 + d) > k$ and $bc < k$ for any k. Figure 3.2 visualizes the solution space for 2D invertible deformations in terms of a, b, c, d, and k. For fixed k, any values of (a, d) that lie above the upper line or below the lower line yield a positive Jacobian determinant if (b, c) lies between these lines. Lines vary as k varies. To allow acute volume shrinkage, we need k to be close to 0 as observed in Figure 3.1. However smaller k values imply more restrictive sets for (b, c).

Lemma 3.2 corresponds to fixing $k = k_x k_y$ such that $k_x + k_y < 1$ and $k_x \geq 0$, $k_y \geq 0$.

(a) $(1 + a)(1 + d) = k$

(b) $bc = k$
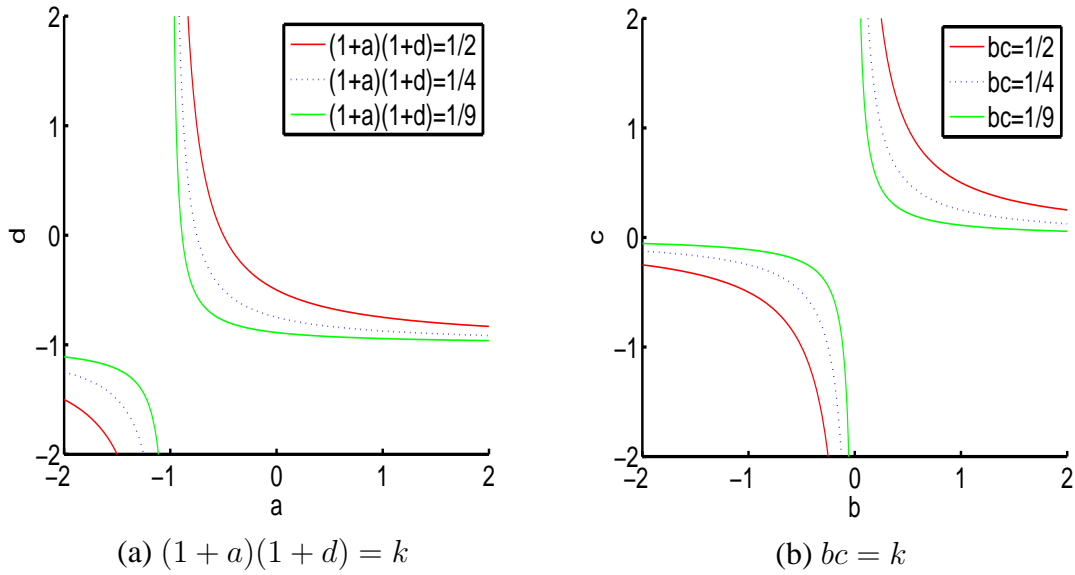
Figure 3.2: Solution space for 2D positive Jacobian determinant. Smaller k values admit smaller a, d values but preclude more values of b, c.

This yields the rectangular areas for a, b, c, d shown in Figure 3.3 (for $k_x = k_y = 1/2$ and $k = 1/4$). Thus Theorem 3.4 not only uses a fixed value for k, but also imposes restrictive box constraints on the deformation derivatives. However it still has a larger solution space than traditional box constraints on the B-spline coefficients such as [11]. Because k is fairly small, relaxing this sufficient condition may allow larger volume shrinkage [13, 15].

3.2.3 Concatenating transformations

Since C_4 is a restrictive sufficient condition, it may not contain all real deformations of interest. To allow larger deformations, we can concatenate multiple elemental transformations that belong to C_4, *i.e.*, let $\underline{T}(\underline{r}) = \underline{T}_N(\cdots(\underline{T}_2(\underline{T}_1(\underline{r}))))$ where each $\underline{T}_k$ satisfies C_4. Since each $\underline{T}_k$ is diffeomorphic, $\underline{T}$ is also diffeomorphic.

Rueckert *et al.* [85] used a box constraint C_2 [11] to guarantee that each elemental transformation is diffeomorphic. We use C_4 for our elemental transformations. This should require fewer elemental transformations because C_4 allows a larger solution space
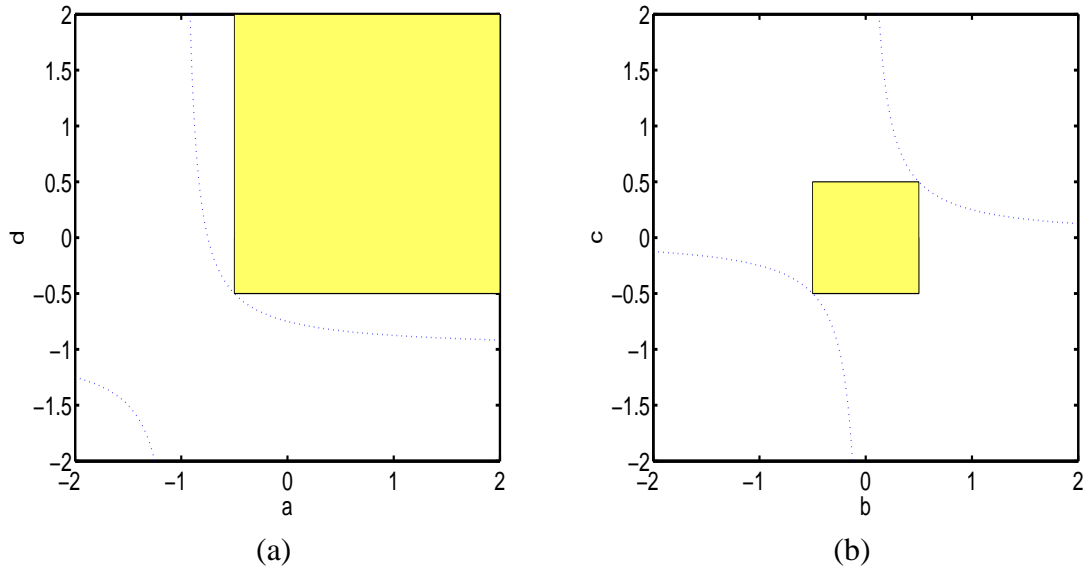
Figure 3.3: Local invertibility sufficient condition space in 2D, for $k = 1/4$, $k_x = k_y = 1/2$ and $K_x = K_y = \infty$. C_4 corresponds to using a fixed k value. (a) $a > -1/2$ and $d > -1/2$. (b) $|b| < 1/2$ and $|c| < 1/2$.

than C_2, as illustrated in the section 3.2.4.

3.2.4   2D simulation: warping a disk to a "C" shape

We applied several constrained nonrigid image registration methods to the challenging registration problem shown in Figure 3.4. We placed deformation knot points every 4th pixel, *i.e.*, $m_x = m_y = 4$. The data fit term used sum of squared differences. For optimization we used augmented Lagrangian multipliers [87] with the conjugate gradient method. Line search step size was determined by one step of Newton's method. We used fast B-spline interpolation [105–107] with a 4-level multiresolution scheme [108].

Figures 3.5 and 3.6 show the unconstrained registration and results of using C_1, C_2 and C_4. The unconstrained result in Figure 3.5(a) shows some unrealistic warping such as folding. Figure 3.5(b) shows the regularized deformed images with a Jacobian penalty based on C_1. This shows a more regular warp than Figure 3.5(a). However, C_1 allows a larger solution space than the ideal solution space C_0.

Source   Target

(a) 2D source image   (b) 2D target image

Figure 3.4: Images for illustrating 2D nonrigid registration.

Figures 3.6(a) and (b) show the limitation of using a single warp based on C_2 and C_4 respectively. The sufficient conditions C_2 and C_4 do not contain the complicated diffeomorphic transformation needed to map the source image to the target image in Figure 3.4. However, this warp can be achieved satisfactorily by composing just 3 warps that each belong to C_4, as shown in Figure 3.8. In contrast, to achieve a satisfactory warp by composing transformations that lie in the box constraint C_2 [11, 85] required about 30 concatenations, as shown in Figure 3.7. For larger and more complicated deformations, our proposed constraint C_4 can be used as a simple elemental transformation to provide diffeomorphic composite transformations.

3.2.5 Larger sufficient condition: Lemma

Section 3.2.2 showed that C_4 is a restrictive solution space mainly because it uses a fixed k globally and allows a rectangular instead of curved areas. In this section, we show that Lemma 3.3 can be used to find another sufficient condition for the local invertibility that has flexible k values locally and allows curved covered areas.

No constraint

No constraint

(a) No constraint.

Jacobian constraint

Jacobian penalty

(b) Jacobian constraint C_1.
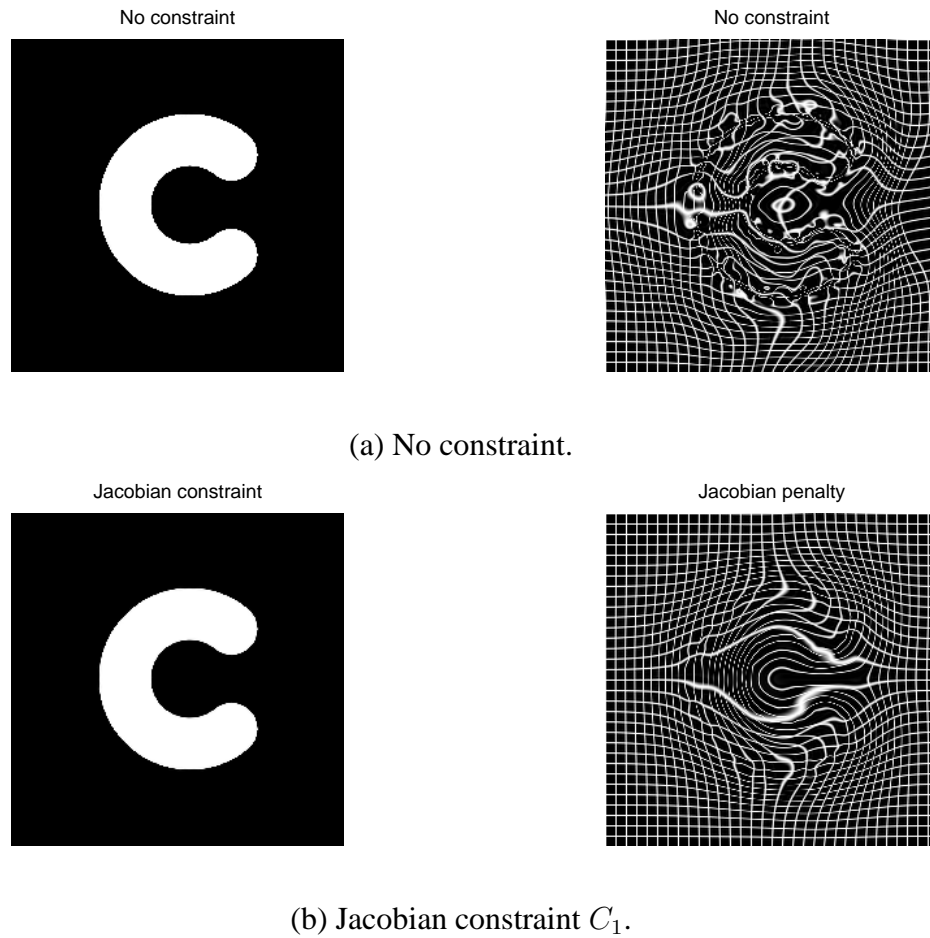
Figure 3.5: Deformed images (left) and their warped grids (right)

Box constraint

Box constraint

(a) Box constraint C_2.

Proposed constraint
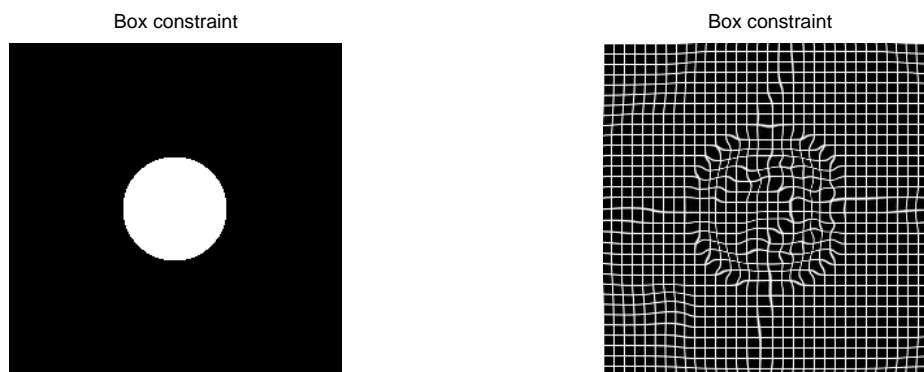
Proposed constraint
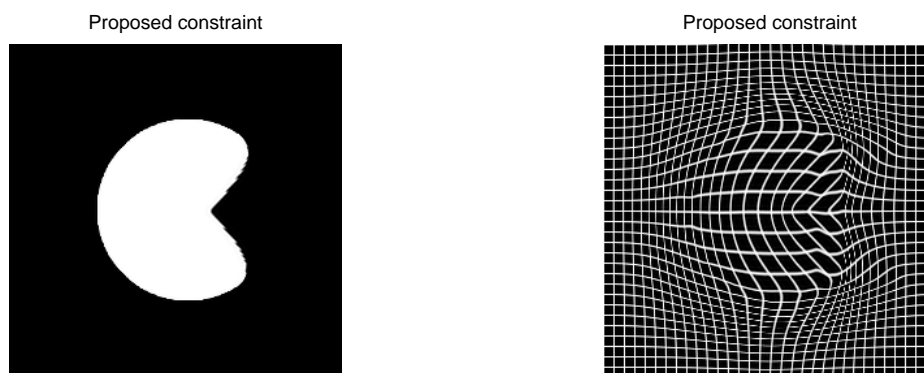
(b) Proposed constraint C_4.

Figure 3.6: Deformed images (left) and their warped grids (right)
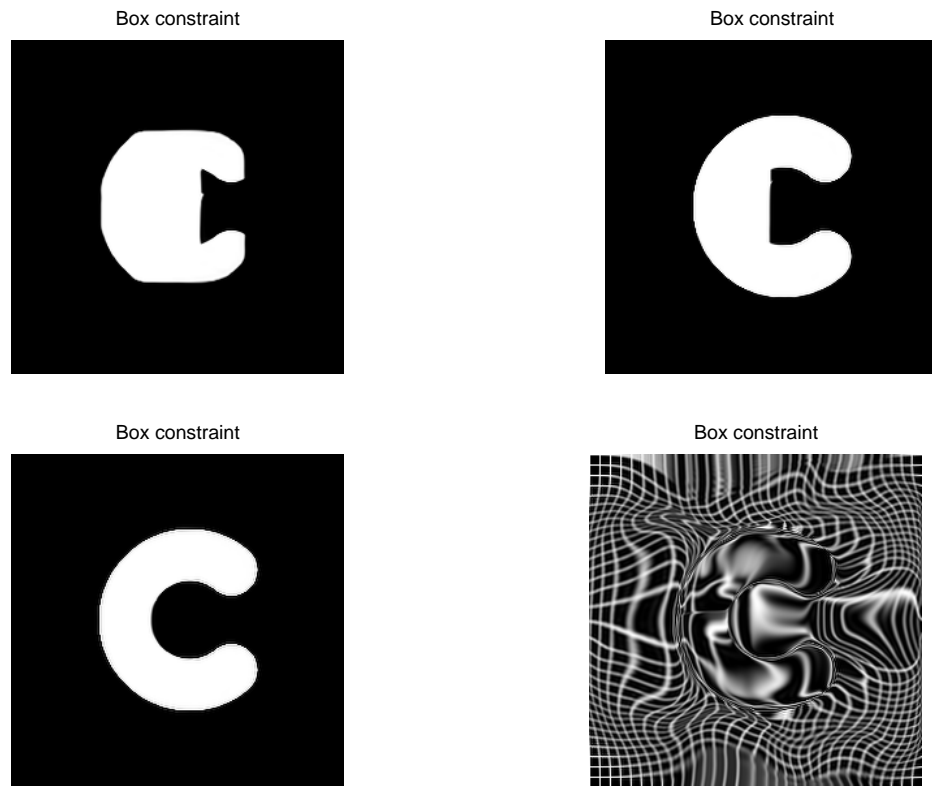
Figure 3.7: 10, 20, 30 compositions of box constraint C_2 and a warped grid of 30 compositions.
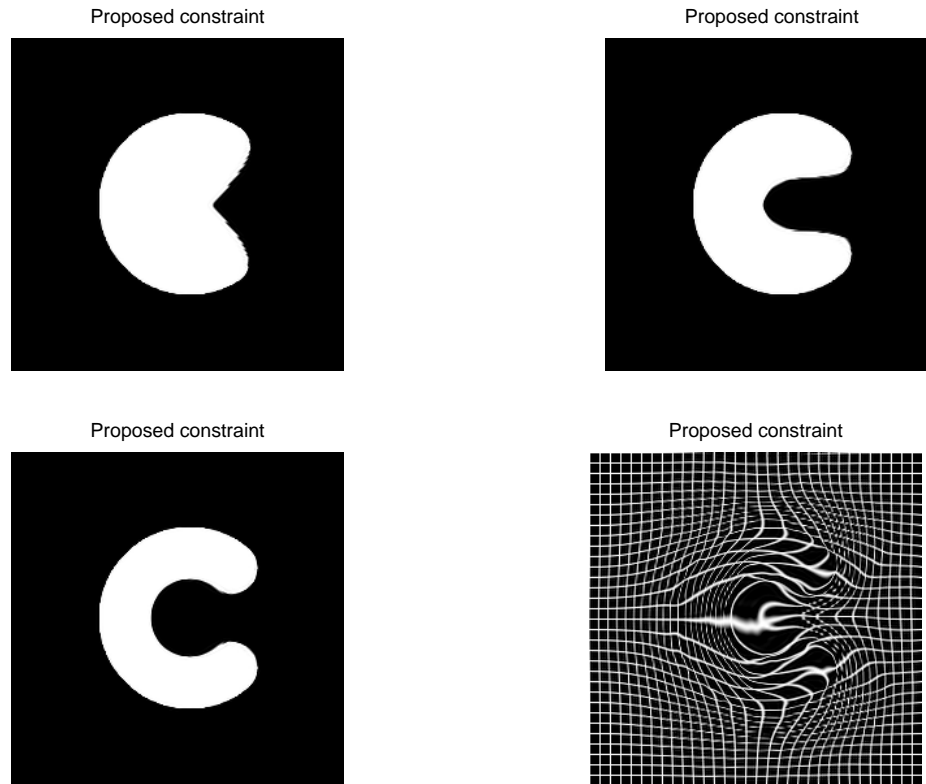
Figure 3.8: 1, 2, 3 compositions of proposed constraint C_4 and a warped grid of 3 compositions. Proposed constraint requires much less transformations to achieve a satisfiable deformation than the box constraint.

Lemma 3.5. *For 2D deformation, if*

$$m_x m_y m_J \le \det H_{i,j,i',j'} \le m_x m_y M_J$$

for $\forall (i,j)$, $i' = i - n + 1, ..., i + n$ *and* $j' = j - n, ..., j + n - 1$ *where*

$$H_{i,j,i',j'} = \begin{pmatrix} m_x + \alpha^x_{i+1,j} - \alpha^x_{i,j} & \alpha^x_{i',j'+1} - \alpha^x_{i',j'} \\ \alpha^y_{i+1,j} - \alpha^y_{i,j} & m_y + \alpha^y_{i',j'+1} - \alpha^y_{i',j'} \end{pmatrix},$$

then $m_J \le |\mathbf{J}|\,(\underline{r}\,) \le M_J$ *for* $\forall \underline{r}$.

Similarly, for 3D deformation, if

$$m_x m_y m_z m_J \le \det K_{i,j,k,i',j',k',i'',j'',k''} \le m_x m_y m_z M_J$$

for $\forall (i,j,k)$, $i' = i - n + 1, ..., i + n$, $j' = j - n, ..., j + n - 1$, $k' = k - n, ..., k + n$, $i'' = i - n + 1, ..., i + n$, $j'' = j - n, ..., j + n$ *and* $k'' = k - n, ..., k + n - 1$ *where*

$$K_{i,j,k,i',j',k',i'',j'',k''} \triangleq \tag{3.8}$$

$$\begin{pmatrix} m_x + \alpha^x_{i+1,j,k} - \alpha^x_{i,j,k} & \alpha^x_{i',j'+1,k'} - \alpha^x_{i',j',k'} & \alpha^x_{i'',j'',k''+1} - \alpha^x_{i'',j'',k''} \\ \alpha^y_{i+1,j,k} - \alpha^y_{i,j,k} & m_y + \alpha^y_{i',j'+1,k'} - \alpha^y_{i',j',k'} & \alpha^y_{i'',j'',k''+1} - \alpha^y_{i'',j'',k''} \\ \alpha^z_{i+1,j,k} - \alpha^z_{i,j,k} & \alpha^z_{i',j'+1,k'} - \alpha^z_{i',j',k'} & m_z + \alpha^z_{i'',j'',k''+1} - \alpha^z_{i'',j'',k''} \end{pmatrix}$$

, then $m_J \le |\mathbf{J}| \le M_J$ *for* $\forall \underline{r}$.

This sufficient condition has much larger solution space than the solution space Theorem 3.4 has. However, the number of constraints are $(2n)^2$ for 2D deformation and $(2n)^4(2n+1)^2$ for 3D deformation for each voxel. For 3D deformation and cubic B-spline basis, we would have 63504 conditions for each voxel. This seems prohibitive for practical use such as penalty methods or constrained optimization methods because there are too many constraints. This optimization is very challenging and it is not addresses in this thesis.

3.3 Simple regularizer based on local invertibility condition

3.3.1 Proposed simple regularizer

If we want to strictly ensure local invertibility, then we maximize a similarity metric subject to the linear constraints $\underline{\alpha} \in C_4$. However, to simplify the computation, we can relax the invertibility condition by using a penalty method [13,15,47]. In a penalty method we maximize an objective function that is the similarity metric minus a penalty function that encourages the invertibility condition, but does not enforce it strictly.

We propose to construct a penalty function based on the following piecewise quadratic function:

$$
p(t; \zeta_1, \zeta_2) = \begin{cases} \frac{1}{2}(t - \zeta_1)^2, & t < \zeta_1 \\ 0, & \zeta_1 \leq t \leq \zeta_2 \\ \frac{1}{2}(t - \zeta_2)^2, & \zeta_2 < t, \end{cases}
$$

which is illustrated in Figure 3.9. The argument t denotes a difference between two adjacent deformation coefficients. This function does not strictly constrain such differences, but its first and second derivatives are simple and convenient for use in optimization algorithms such as conjugate gradient. The final new penalty function is

$$
\begin{aligned}
R(\underline{\alpha}) \quad = \quad & \sum_{q \in \{x,y,z\}} \sum_{i,j,k} \\
& \left[p(\alpha_{i+1,j,k}^q - \alpha_{i,j,k}^q; \zeta_1^{q,x}, \zeta_2^{q,x}) \right. \\
& + p(\alpha_{i,j+1,k}^q - \alpha_{i,j,k}^q; \zeta_1^{q,y}, \zeta_2^{q,y}) \\
& \left. + p(\alpha_{i,j,k+1}^q - \alpha_{i,j,k}^q; \zeta_1^{q,z}, \zeta_2^{q,z}) \right],
\end{aligned} \tag{3.9}
$$

where $\zeta_1^{q,r} = -m_q k_q$ for $\forall r \in \{x, y, z\}$, $\zeta_2^{q,r} = m_q k_q$ for $r \neq q$ and $\zeta_2^{q,r} = m_q K_q$ for $r = q$. Note that choosing $\zeta_1 = \zeta_2 = 0$ would correspond to a quadratic roughness penalty over B-spline coefficients, which is akin to encouraging the volume preserving condition

$|\mathbf{J}| = 1, \ \forall \underline{r}.$

Being based on the somewhat restrictive solution space C_4, the new penalty method can encourage the local invertibility on the whole continuous domain with a fast and memory efficient implementation. This implementation is possible because C_4 does not require additional B-spline interpolations beyond the interpolations needed for the data fitting term. It also encourages the smoothness of deformations inherently because it constrains the differences between adjacent deformation coefficients. In contrast, using C_0 or C_1 is much more expensive for one transformation.
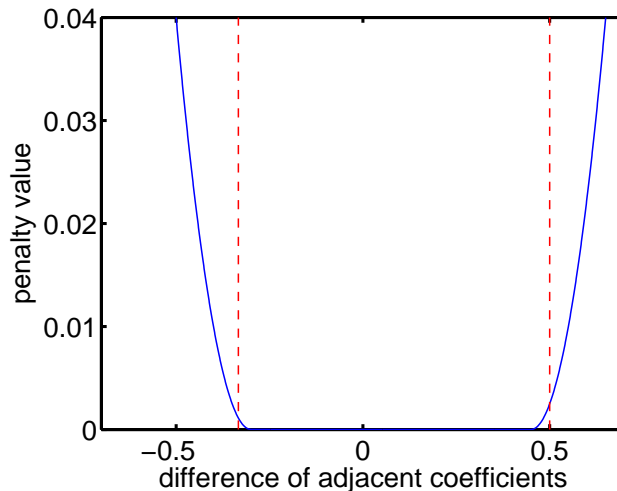
Figure 3.9: A variant of quadratic penalty function (solid) and real constraints (dashed) used with constraint set C_4.

3.3.2 Incorporating *a priori* knowledge of motions

For diffeomorphic transformations using Theorem 3.4, the usual choice would be $k_x = k_y = k_z = 1/3 - \epsilon$ for some small ϵ. However, if we have *a priori* knowledge about the deformation, then we can assign each k_q accordingly. For instance, for registering thorax inhale and exhale images, we can assign $k_x = k_y = 1/4 - \epsilon$ and $k_z = 1/2 - \epsilon$ because the deformation in the z direction is larger due to diaphragm motion, whereas the deformations in the x and y directions are smaller. With this design, C_4 allows 50%

local shrinkage along z and 75% local shrinkage along x and y instead of allowing 67% shrinkage in each direction. We can use this sufficient condition for the proposed simple regularizer to encourage local invertibility of the deformation.

3.3.3   2D simulation: expansion and shrinkage

We applied nonrigid image registration to the 256×256 images in Figure 3.10 using no constraint, a Jacobian penalty based on C_1, a quadratic roughness penalty [112], a regularizer based on Kim's constraint C_3, and our proposed penalty method based on C_4. Figure 3.10 has an expanding circle and a shrinking ellipse to illustrate the difference between C_3 and C_4. Since we have *a priori* knowledge about vertical motion, we investigated two sets of parameters in C_4: a symmetric way with $k_x = k_y = 1/2 - 0.01 \times 1/2$ as well as an asymmetric way with $k_x = 0.35 - 0.01 \times 0.35 < k_y = 0.65 - 0.65 \times 0.01$.

We placed deformation knot points every 4th pixel. The data fit term used sum of squared differences. For optimization we used the conjugate gradient method. Line search step size was determined by one step of Newton's method. We used fast B-spline interpolation and the 4-level multiresolution scheme as in III-D. We ran 200 iterations for each level or ran until the l_0 norm of the gradient is less than the machine accuracy. We checked the local invertibility by computing Jacobian determinant values on a grid 10 times finer than the image resolution.

Figure 3.11 quantifies the tradeoff between image similarity and local invertibility for the 5 different registration methods for a range of regularization parameters. The horizontal axis is the root mean square (RMS) difference between the deformed image and the target image (log scale) and the vertical axis is the number of the finer (10 times) voxel grid points having a non-positive Jacobian determinant (log scale). We took a log after adding 1 for the number of non-positive Jacobian determinant since the lowest number of

it is 0.

For the unconstrained case, the RMS difference was 0.0109 and the number of negative Jacobian determinants was 497644. As the regularization parameters decrease, the RMS differences and the number of negative Jacobian determinants of all other methods approached closely to these values. This is expected because the unconstrained case is the same as any other penalty method with regularization parameter 0.

(a) 2D source image   (b) 2D target image
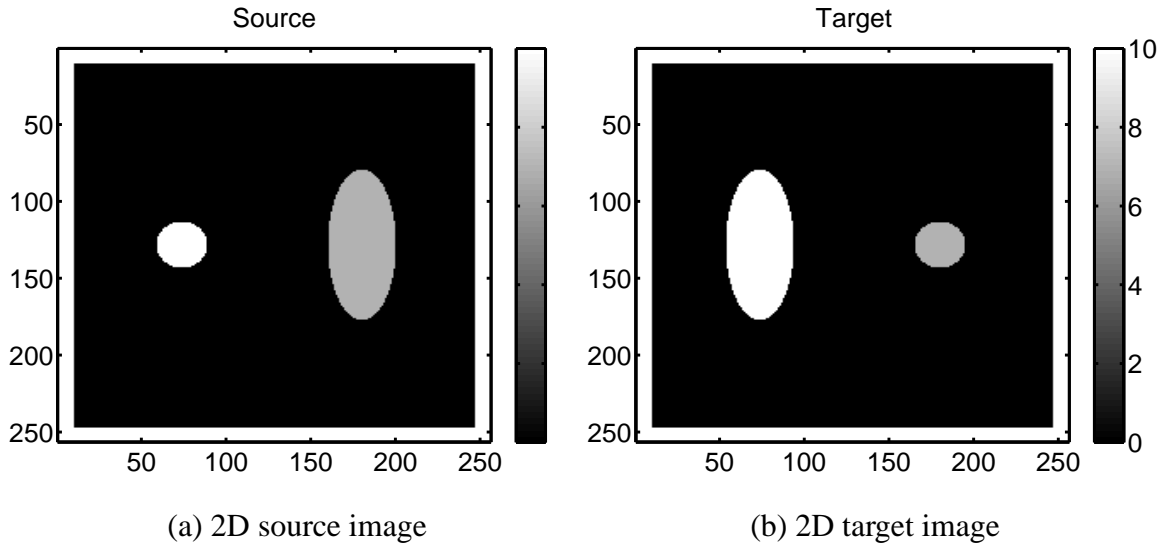
Figure 3.10: Images for illustrating expansion and shrinkage.

As we increased the regularization parameters, the number of negative Jacobian determinants "generally" decreases, eventually towards zero, although not always monotonically. The RMS differences also "generally" increase as the regularization parameters increase for most methods except Jacobian penalty. This is because the Jacobian constraint C_1 contains the original constraint C_0 and it does not restrict the deformation so that it can achieve low RMS difference for strong penalty parameters. For properly chosen regularization parameters, symmetric/asymmetric proposed simple penalties show fairly good performance compared to Kim's or quadratic penalty methods based on more restrictive sufficient conditions (Kim's: $K_x = k_x$, $K_y = k_y$ and quadratic: $K_x = k_x = 0$,
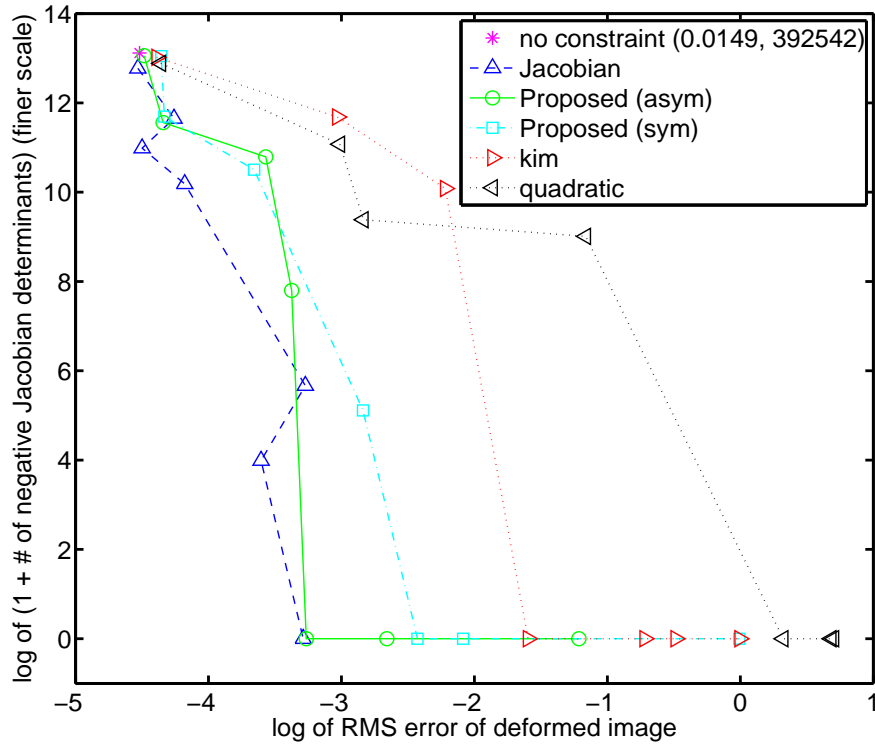
Figure 3.11: RMS difference and negative Jacobian determinant trade-off for different regularization parameters. (log scale)

Table 3.1: The best RMS difference for each method with zero negative Jabocian determinant in 2D simulation.

Jacobian	New (asym)	New (sym)	Kim	Quadratic
0.0373	0.0360	0.0454	0.2026	0.6091

$K_y = k_y = 0$).

Table 3.1 shows the best RMS difference of image for each method with zero non-positive Jabocian determinant values over the 10 times finer grid. The proposed simple penalty with *a priori* motion information performed well compared to Jacobian penalty. However, as the regularization method depends on more restrictive condition, the RMS difference is larger. It clearly shows that a quadratic penalty oversmoothes the deformations.

Our proposed asymmetric penalty performed a little better than Jacobian penalty in

these experiments. However, our proposed penalty may not always perform better. It depends on the convergence, regularization parameter, image structure and so on. Since the data fitting term is non-convex, local minima may affect the result, too. However, for simpler cases like in Figure 3.10 our proposed regularization method may perform close to the Jacobian penalty method. In the section 3.3.4, we apply both methods to the 3D real CT images of a patient.

3.3.4   3D real CT images

We applied our proposed regularization method (3.9) to the problem of registering 3D breath-hold X-ray CT images of a real oncology patient scanned at inhale and at exhale. These images are useful for radiation treatment planning. The image size was $396 \times 256 \times 128$ as shown in Figures 3.12 and 3.13. We chose $k_x = k_y = 1/4 - 0.01 \times 1/4$ and $k_z = 1/2 - 0.01 \times 1/2$ because we expect the deformation in the z direction to be larger than the deformations in the x and y directions due to diaphragm motion.

We used the same methods as in Section IV-C except for the multiresolution scheme. For the first 3 levels of multiresolution, the knot spacing was every 8 pixels for downsampled images, and for the last level of multiresolution the knot spacing was every 4 pixels. We ran 120 iterations at each level to see the convergence properties. The regularization parameter that multiplies (3.9) was chosen experimentally to achieve the minimum value of data fitting term such that all Jacobian values on the image grid were positive.

Figure 3.14 shows the difference images between the target image and the deformed images. As expected, the difference image for unconstrained registration in Figure 3.14(a) has smaller values than the constrained difference images in Figures 3.14(b) and (c). The RMS difference for unconstrained registration was the smallest, which was 19.9 HU. The RMS errors of the Jacobian penalty (25.9 HU) and the proposed penalty (29.2 HU) were
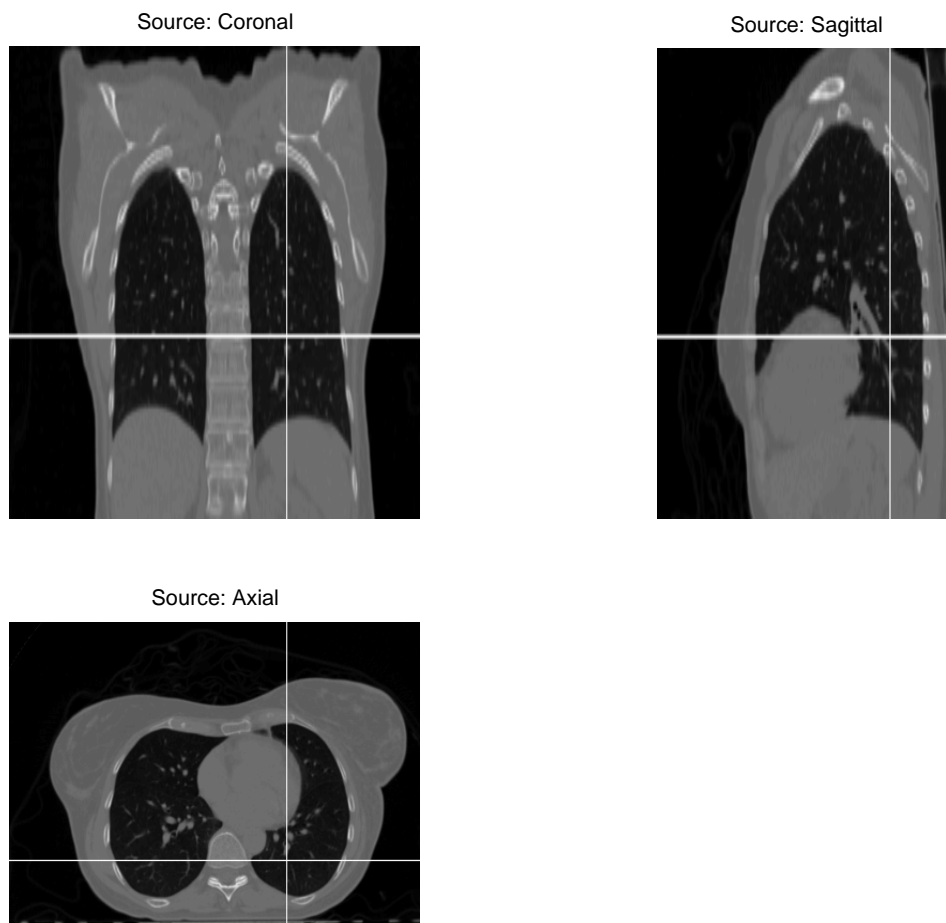
Figure 3.12: 3D source (exhale) X-ray CT image.
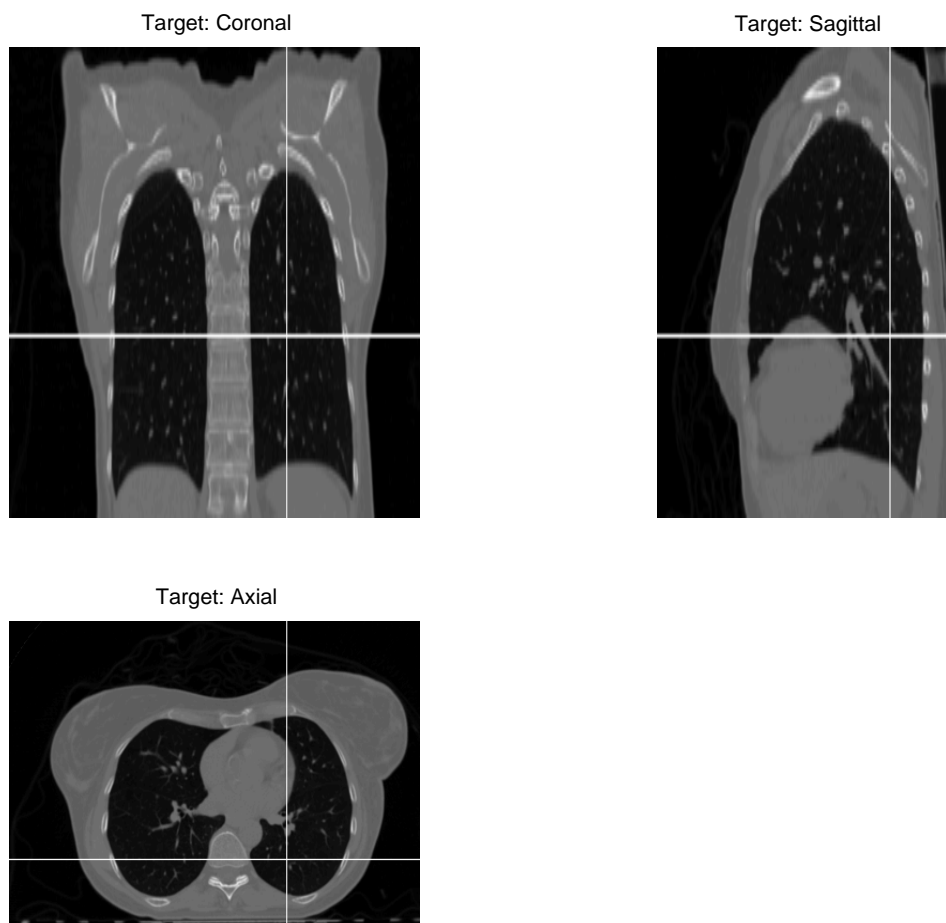
Figure 3.13: 3D target (inhale) X-ray CT image.

Table 3.2: Computational cost at the finest level

Method	CPU time per iteration (sec)
Unconstrained	25.7
Jacobian penalty	81.1
Proposed method	27.4

somewhat higher. However, Figure 3.15(a) shows that unconstrained registration yields an unrealistic warped grid. The number of negative Jacobian determinant voxels was 316914 out of 12582912 voxels. Figure 3.15(c) shows a smoother warp than Figure 3.15(b) because our proposed penalty method is based on C_4 which is a smaller set than C_1. Our proposed method has smoothness property implicitly because it restricts the range of the differences between adjacent B-spline coefficients.

The proposed penalty method was much faster and more memory efficient than the traditional Jacobian penalty method per iteration. If one uses the sum of squared error as the data fitting term and penalizes negative Jacobian determinant values on each image grid point in 3D with cubic B-splines, then the interpolations needed to compute the gradients of the direct Jacobian penalty function require about 1.8 times more operations than the interpolations needed for the gradient of the data fitting term. Table 3.2 shows the computational cost for one iteration at the last (finest) level of the multiresolution procedure. Our proposed method requires only slightly more time per iteration than unconstrained registration, and much less time than using a Jacobian penalty. Furthermore, in this simulation, the traditional Jacobian penalty method required about twice as much memory as our proposed method because it must store the interpolation results for the Jacobian gradient. Figure 3.16 shows the convergence of each method.

We could compose a coarse resolution warp based on (3.9) with one full sequence of coarse-to-fine warp based on (3.9) to reduce RMS differences further with only slight increase in computation.

3.4 Discussion

We proposed a new condition (Theorem 3.4) that is sufficient to ensure the local invertibility of transformations based on B-splines. Its limitation can be overcome by using composite transformations. This proposed sufficient condition can be used with constrained optimization such as augmented Lagrangian multiplier method [87] or Dykstra's cyclic projection method [41].

We showed that the proposed sufficient condition is more general than other simple sufficient conditions that ensure local invertibility everywhere such as box constraint [11]. When used in composite transformations, it requires many fewer transformations to achieve comparable deformations [85].

We also relaxed our local invertibility condition by a simple quadratic-like penalty. This approach achieves more flexible image matching compared to other penalty methods based on more restrictive local invertibility conditions. For practical use in a thorax image registration, we used a single transformation with a simple quadratic-like penalty that encourages $\underline{\alpha} \in C_4$. This gave a fairly good deformation with no negative Jacobian determinant values on image voxel grid points. This approach is much simpler and faster than the traditional Jacobian determinant penalty and is more memory efficient.

Some application areas require not only local invertibility, but also require computing the inverse transformation. One approach is to estimate both forward and backward image registration parameters with consistency regularizer [12]. Using both consistency regularizer and our proposed regularizer can be interesting future work.

Another interesting future work is implementing Lemma 3.5. It will allow much larger sufficient condition compared to the proposed sufficient condition C_4, but the optimization is challenging.

No constraint: Coronal

No constraint: Sagittal

(a) No constraint

Jacobian penalty: Coronal

Jacobian penalty: Sagittal

(b) Jacobian penalty

Proposed method: Coronal

Proposed method: Sagittal
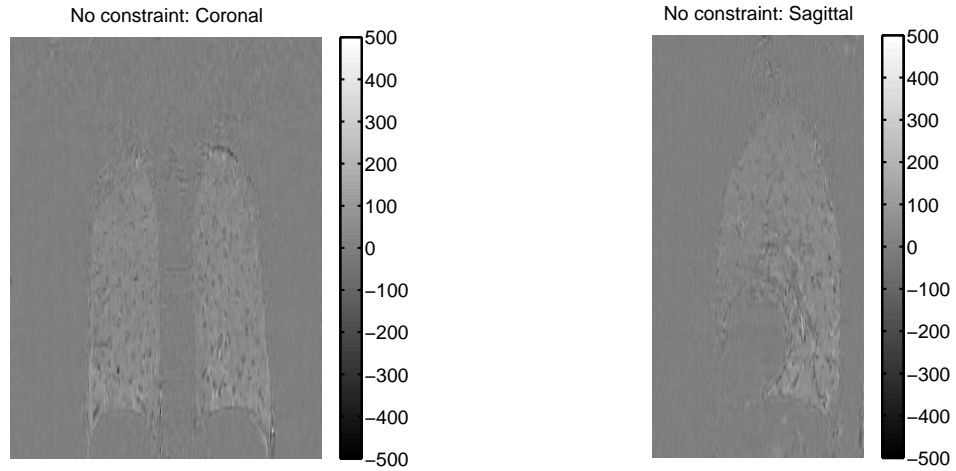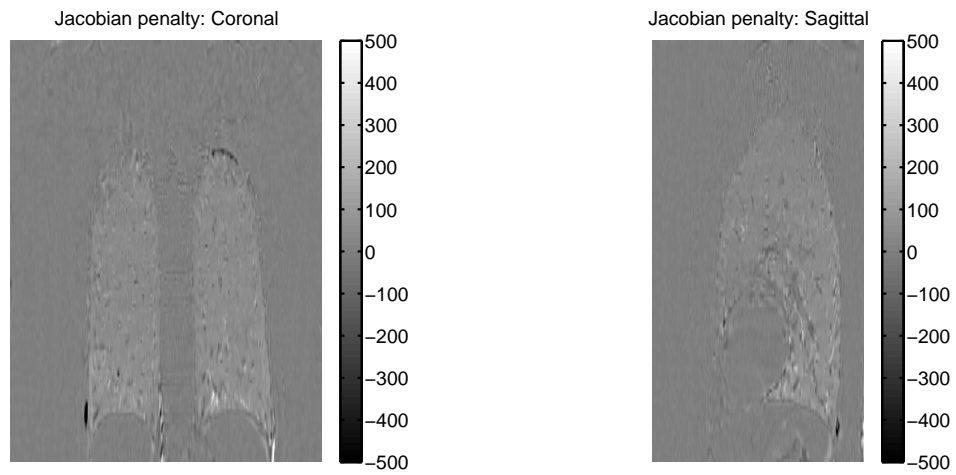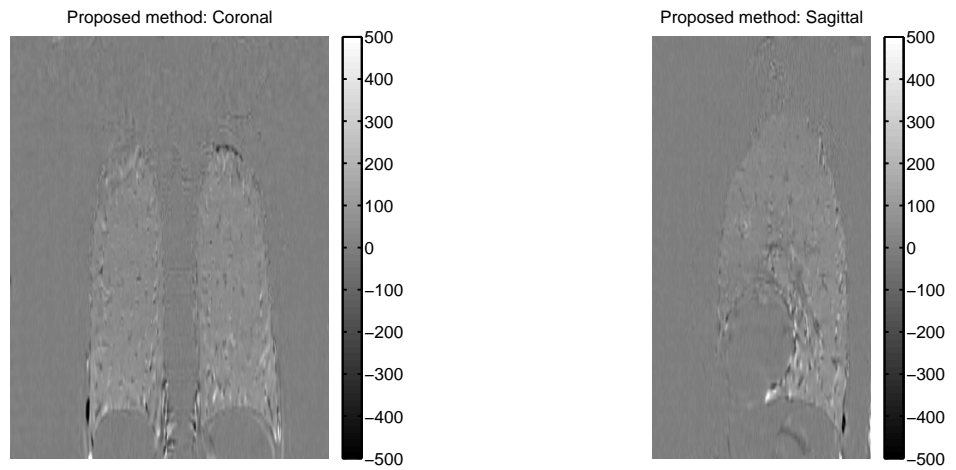
(c) Proposed penalty

Figure 3.14: Differences between 3D target and deformed images.

No constraint: Coronal

No constraint: Sagittal

(a) No constraint

Jacobian penalty: Coronal

Jacobian penalty: Sagittal

(b) Jacobian penalty

Proposed method: Coronal

Proposed method: Sagittal
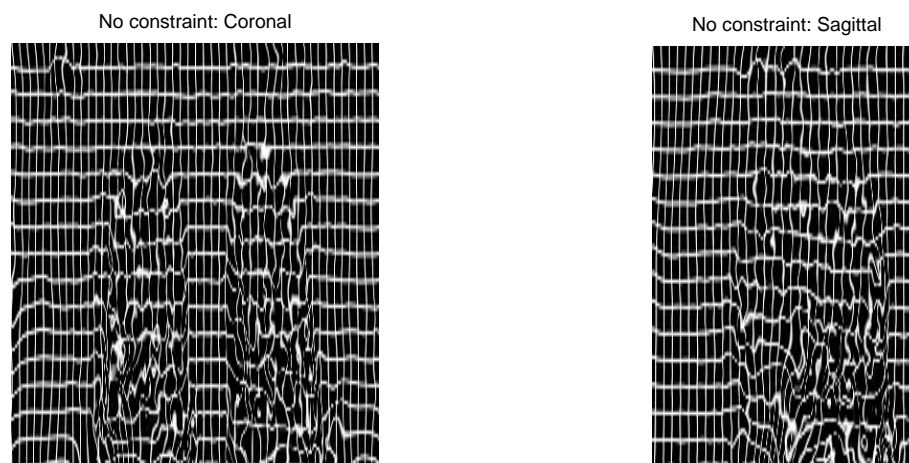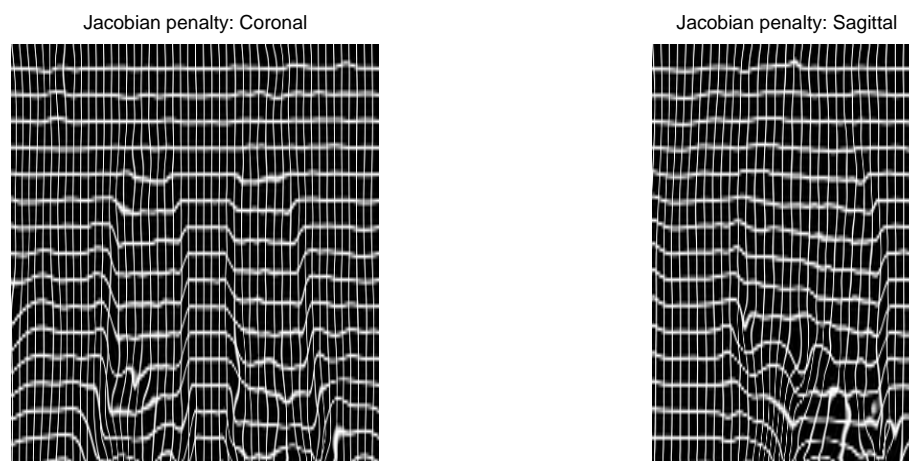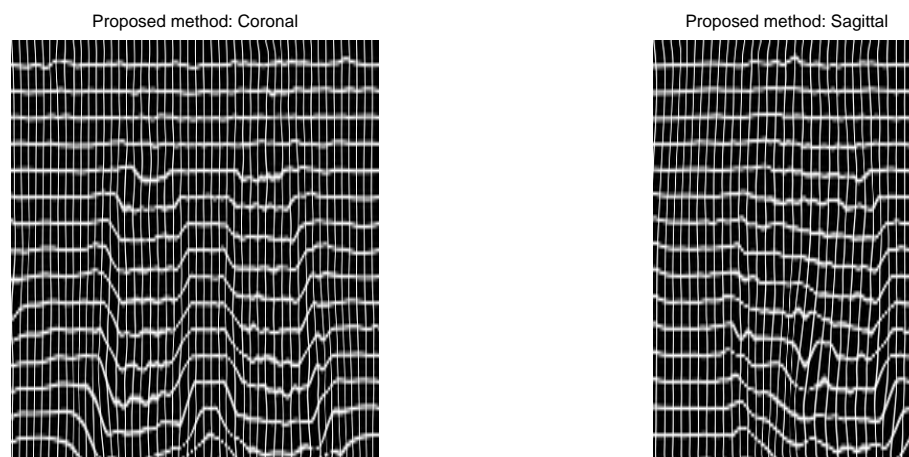
(c) Proposed penalty

Figure 3.15: Warped grids for 3D inhale-exhale registration.
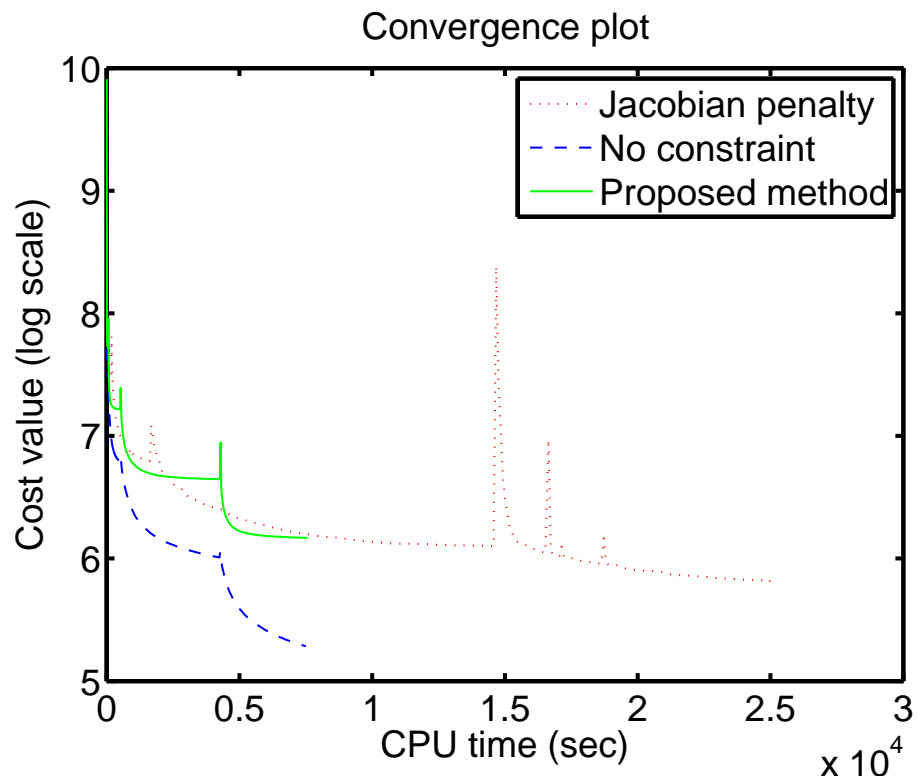
Figure 3.16: Convergence of each method.

CHAPTER 4

Regularization for nonrigid motions: rigidity and sliding [2]

Nonrigid image registration is a key tool in medical imaging. It provides more flexible image matching than rigid transformation, but suffers by its ill-posedness, often resulting in unrealistic deformations [18]. There has been a lot of research on regularizing or constraining deformations with reasonable motion priors such as smoothness of deformations, the invertibility of deformations [13, 15, 38, 41, 68, 80, 87] and the rigid deformations of rigid objects (or tissues) [55, 56, 60, 84, 93]. Many papers have investigated each constraint separately.

Both invertible deformations and rigid deformations of rigid tissues are reasonable constraints in respiratory motion estimation because breathing motion is invertible and some rigid structures such as bones are present. Since smoothness motion regularizer or motion invertibility regularizer usually cause bone warping in ribs, it is only natural to use both motion priors together in the image registration of human respiratory motion. Combining both regularizers seems straight forward, but both motion regularizers cause conflicts in some areas near the interface between the rib cage and the diaphragm. In these areas, motion invertibility prior and tissue rigidity prior penalize deformations in opposite ways.

---

[2]This chapter is based on [17].

In chapter 3, we proposed a simple piecewise quadratic penalty that encourages the local invertibility of motions [13, 17]. In this chapter, we propose to relax this motion regularizer by using a Geman-type function [8, 26]. As we use the rigid motion constraint for rigid tissues together [56, 84, 93], this allows for deformations to be piecewise smooth instead of globally smooth. With small sacrifice of regularity, this relaxed motion invertibility regularizer allows the motion regularizer based on tissue rigidity to improve the bone rigistration [17]. This also permits better matching between deformed and target images and deformations to be discontinuous in the area of the interface between the rib cage and the diaphragm.

We applied this Geman-type penalty function only to the x- and y-direction partial derivatives of the z-direction deformation to address the sliding motion of the diaphragm. $192 \times 128 \times 128$ 3D CT inhale and exhale images of a real patient were used to show the benefits of this new penalty method.

4.1 Background

Figure 4.1 shows zoomed coronal CT images of a real patient at exhalation and inhalation. The diaphragm slid down as the patient inhaled while his/her rib bones stayed at a similar position. Smoothness motion prior and motion invertibility prior encourage the connectivity between rib bones and diaphragm to be maintained. Usually the ribs near the diaphragm in an exhale image go down together with the diaphragm as a patient inhales. Since the ribs are relatively small structures, the image matching data fitting term is not strong enough to allow the ribs to stay still.

The rigid motion prior of rigid structures such as bones can correct the bone warps. However, when we use both the motion invertibility prior and the tissue rigidity prior together, the motion invertibility prior encourages some rib bones to go down and the

Figure 4.1: Coronal views of 3D exhale and inhale images of a real patient. Connectivity between diaphragm and rib bones is not preserved since diaphragm is sliding down while rib bones remain at the similar location.

tissue rigidity prior encourages the rib bones to stay in position. This causes conflicts. Figure 4.2 shows the number of negative Jacobian determinant values when we apply both motion regularizers together. As expected, most negative Jacobian determinant values are near the interface between the diaphragm and the rib cage.

4.2   Method

4.2.1   A simple penalty that encourages local invertibility

We briefly review the motion invertibility regularizer in chapter 3 [13, 15].

Theorem 4.1. *Suppose* $0 \leq k_q < 1/2$ *for* $q \in \{x, y, z\}$. *Define:*

$$C_4 \equiv \{\underline{\alpha} : - m_x k_x \leq \alpha_{i+1,j,k}^x - \alpha_{i,j,k}^x \leq m_x K_x,$$

$$- m_y k_y \leq \alpha_{i,j+1,k}^y - \alpha_{i,j,k}^y \leq m_y K_y,$$

$$- m_z k_z \leq \alpha_{i,j,k+1}^z - \alpha_{i,j,k}^z \leq m_z K_z,$$

$$|\alpha_{i+1,j,k}^q - \alpha_{i,j,k}^q| \leq m_q k_q \, for \, q = y, z,$$

$$|\alpha_{i,j+1,k}^q - \alpha_{i,j,k}^q| \leq m_q k_q \, for \, q = x, z,$$

$$|\alpha_{i,j,k+1}^q - \alpha_{i,j,k}^q| \leq m_q k_q \, for \, q = x, y, \quad \forall i, j, k\}.$$
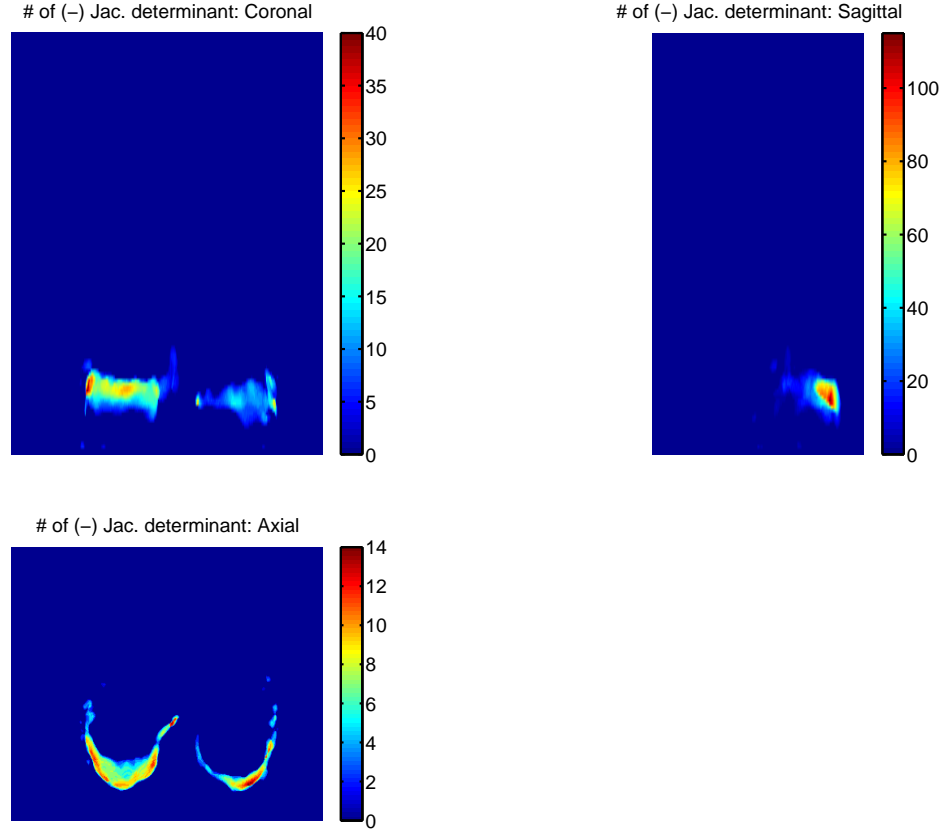
Figure 4.2: Coronal, sagittal and axial views of the number of negative Jacobian determinant values when we use motion invertibility prior and tissue rigidity prior together.

In (2.3), if $\underline{\alpha} \in C_4$ then the Jacobian determinant of $\underline{T}$ satisfies the bounds

$$1 - (k_x + k_y + k_z) \leq \det \nabla \underline{T}(\underline{r}) \leq (1 + K_x)(1 + K_y)(1 + K_z)$$

$$+ (1 + K_x)k_y k_z + k_x(1 + K_y)k_z + k_x k_y(1 + K_z)$$

for $\forall \underline{r} \in \mathbf{R}^3$. Moreover, if $k_x + k_y + k_z < 1$, then the transformation (2.3) is locally invertible everywhere.

Based on Theorem 4.1, we proposed the following simple penalty that encourages

local invertibility:

$$
\begin{aligned}
R_I(\underline{\alpha}) \;=\; & \sum_{q \in \{x,y,z\}} \sum_{i,j,k} \Big[p(\alpha^q_{i+1,j,k} - \alpha^q_{i,j,k}; \zeta^{q,x}_1, \zeta^{q,x}_2) \\
& + p(\alpha^q_{i,j+1,k} - \alpha^q_{i,j,k}; \zeta^{q,y}_1, \zeta^{q,y}_2) \\
& + p(\alpha^q_{i,j,k+1} - \alpha^q_{i,j,k}; \zeta^{q,z}_1, \zeta^{q,z}_2) \Big]
\end{aligned}
\tag{4.1}
$$

where $\zeta^{q,s}_1 = -m_q k_q$ for $\forall s \in \{x,y,z\}$, $\zeta^{q,s}_2 = m_q k_q$ for $s \neq q$ and $\zeta^{q,s}_2 = m_q K_q$ for $s = q$. The function p is defined by

$$
p(t; \zeta_1, \zeta_2) =
\begin{cases}
\frac{1}{2}(t - \zeta_1)^2, & t \leq \zeta_1 \\[2mm]
0, & \zeta_1 < t \leq \zeta_2 \\[2mm]
\frac{1}{2}(t - \zeta_2)^2, & \text{otherwise.}
\end{cases}
\tag{4.2}
$$

All parameters k_q, K_q are determined based on Theorem 4.1 and $k_x + k_y + k_z < 1$ allows (4.1) to be a penalty that encourages local invertibility. [13, 15].

4.2.2 A tissue rigidity penalty

Staring *et al.* [93] and Modersitzki [60] defined a rigid transformation as follows.

Definition 4.2. A transformation $\underline{T}(\underline{r})$ is rigid if it is linear, *i.e.*, $\partial^2_{i_1,i_2}\underline{T} = 0$ for all $i_1, i_2 \in \{x, y, z\}$, orthogonal, *i.e.*, $\nabla\underline{T}'\nabla\underline{T} = I$, and orientation preserving for $\forall \underline{r} \in \mathbf{R}^3$, *i.e.*, $\det \nabla\underline{T} = 1$.

Using all three constraints requires high computational complexity for calculating the first and second order derivatives of transformation. Since we apply an invertibility constraint which encourages $\det \nabla\underline{T} > 0$, the orthogonal property $\nabla\underline{T}'\nabla\underline{T} = I$ implies orientation preserving $\det \nabla\underline{T} = 1$. We do not also use linear property $\partial^2_{i_1,i_2}\underline{T} = 0$ since it is not a dominant term according to the simulation of Staring *et al.* [93]. It is also not

desirable to compute the second order partial derivatives since it is computationally demanding. Thus, we only use the orthogonal property, following Loeckxx *et al.* [56] and Ruan *et al.* [84]. So, our rigidity penalty function is

$$R_R(\underline{\alpha}) = \sum_{\underline{r}} \gamma(f(\underline{r})) ||\nabla \underline{T}(\underline{r})^T \nabla \underline{T}(\underline{r}) - I||^2_{Frob}, \qquad (4.3)$$

where $|| \cdot ||_{Frob}$ is a Frobenius norm and $\gamma(x) = \tanh((x - 1200)/10)/2 + 1/2$.

Ruan *et al.* [84] calculates the Jacobian values on all image voxels and Staring *et al.* [93] suggests to calculate only on all knot points instead of all image voxels. This choice depends on the scale of images. If a lower resolution image can capture the topology of bone structure well, then we can calculate Jacobian values on all the knot points only. However, if the original image has poor resolution, then we may have to calculate all Jacobian values on all image voxels.

Since the number of voxels containing bone structure is usually much smaller than the number of voxels for the whole body, we can save more computation time by calculating the tissue rigidity contraint only for voxels containing rigid tissues. We do not calculate $||\nabla \underline{T}(\underline{r})^T \nabla \underline{T}(\underline{r}) - I||^2_{Frob}$ if $\gamma(f(\underline{r})) < \epsilon$.

4.2.3 A proposed relaxed invertibility penalty

Since using both motion invertibility penalty (4.1) and tissue rigidity penalty (4.3) causes conflicts near the diaphragm and the rib cage, we propose to relax the motion invertibility penalty (4.1). However, since sliding of the diaphragm in respiratory motion occurs mainly in the z-direction deformation, we only relax the invertibility penalty for the x- and y- differences of z-direction deformation by using a Geman-type function [26]. We replace some of the $p(\cdot)$ terms in (4.1) as follows:

$$
\begin{aligned}
p(c^z_{i+1,j,k} - c^z_{i,j,k}; \zeta^{z,x}_1, \zeta^{z,x}_2) &\quad to \quad g(c^z_{i+1,j,k} - c^z_{i,j,k}; \zeta^{z,x}_1, \zeta^{z,x}_2, \alpha_0) \\
p(c^z_{i,j+1,k} - c^z_{i,j,k}; \zeta^{z,y}_1, \zeta^{z,y}_2) &\quad to \quad g(c^z_{i,j+1,k} - c^z_{i,j,k}; \zeta^{z,y}_1, \zeta^{z,y}_2, \alpha_0)
\end{aligned}
\qquad (4.4)
$$

where

$$g(t; \zeta_1, \zeta_2, \alpha_0) = \begin{cases} \frac{1}{2}(\alpha_0 - \zeta_1)^2, & t \leq \alpha_0 \\[2mm] \frac{1}{2}(t - \zeta_1)^2, & \alpha_0 < t \leq \zeta_1 \\[2mm] 0, & \zeta_1 < t \leq \zeta_2 \\[2mm] \frac{1}{2}(t - \zeta_2)^2, & \zeta_2 < t \leq \alpha_1 \\[2mm] \frac{1}{2}(\alpha_1 - \zeta_2)^2, & \text{otherwise.} \end{cases} \tag{4.5}$$

Therefore, the modified invertibility regularizer $\tilde{R}_I(\underline{\alpha})$ is

$$\begin{aligned}
\tilde{R}_I(\underline{\alpha}) = & \sum_{q \in \{x,y\}} \sum_{i,j,k} \Big[p(\alpha_{i+1,j,k}^q - \alpha_{i,j,k}^q; \zeta_1^{q,x}, \zeta_2^{q,x}) \\
& + p(\alpha_{i,j+1,k}^q - \alpha_{i,j,k}^q; \zeta_1^{q,y}, \zeta_2^{q,y}) \\
& + p(\alpha_{i,j,k+1}^q - \alpha_{i,j,k}^q; \zeta_1^{q,z}, \zeta_2^{q,z}) \Big] \\
& + g(\alpha_{i+1,j,k}^z - \alpha_{i,j,k}^z; \zeta_1^{z,x}, \zeta_2^{z,x}, \alpha_0) \\
& + g(\alpha_{i,j+1,k}^z - \alpha_{i,j,k}^z; \zeta_1^{z,y}, \zeta_2^{z,y}, \alpha_0) \\
& + p(\alpha_{i,j,k+1}^z - \alpha_{i,j,k}^z; \zeta_1^{z,z}, \zeta_2^{z,z})
\end{aligned} \tag{4.6}$$

Figure 4.2.3 depicts p and g functions.

4.2.4 Graduated non-convexity (GNC) method

Our proposed penalties change the problem in (3.1) as follows:

$$\hat{\underline{\alpha}} = \arg\max_{\underline{\alpha}} \Psi[g(\cdot), f(\underline{T}(\cdot; \underline{\alpha}))] - \beta_I \tilde{R}_I(\underline{\alpha}) - \beta_R R_R(\underline{\alpha}). \tag{4.7}$$

The proposed penalty function (4.5) is non-convex and it may cause local minima during the optimization. Blake *et al.* describe a graduated non-convexity (GNC) method as an optimization method with Geman-type function [8]. It changes the shape of a function g from an almost convex function to a Geman function as optimization proceeds. We used a GNC method combined with a conjugate gradient method to optimize the cost function
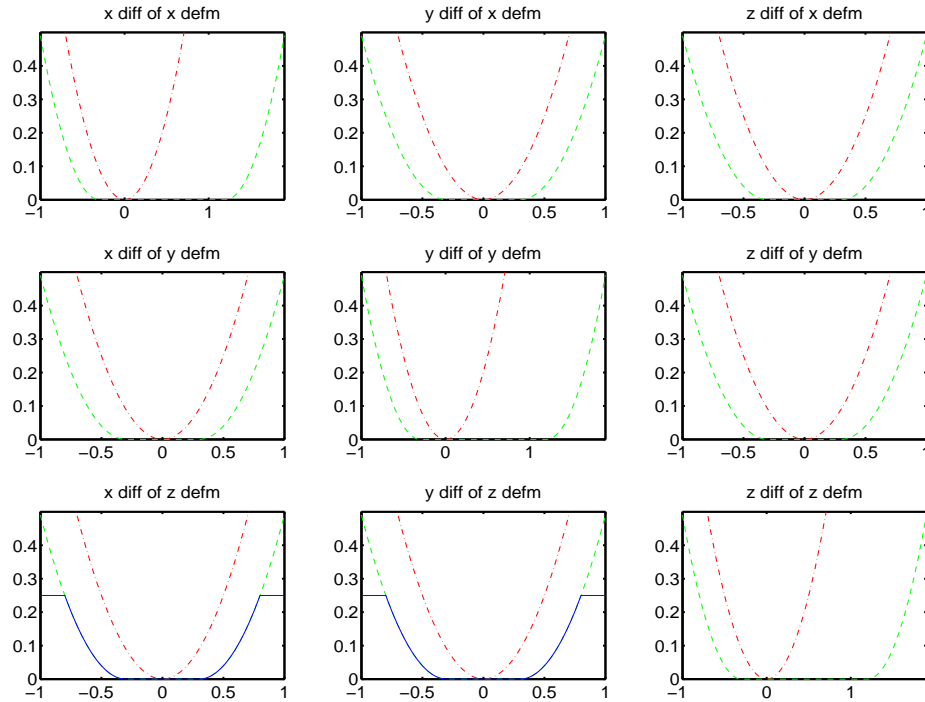
Figure 4.3: A quadratic-like penalty for invertibility constraint and a Geman-like penalty to relax invertibility constraint.

(4.7).

4.3 Simulation results

4.3.1 Experiment setup

We investigated $192 \times 128 \times 128$ 3D CT inhalation and exhalation images of a real patient shown in Figures 3.12 and 3.13. We used a 3rd-order B-spline basis for deformation and deformation knots for every 4 voxels. The sum of the squared difference was used for the data fitting term. We did not use a multi-resolution for this experiment since the lower resolution image seemed to lose detailed information about the rib cage and our rigidity penalty did not seem to work well with poor resolution information. We performed 300

Table 4.1: Negative Jacobian determinant values and data fitting RMS error

Method	# of (-) Jacobian determinant	Data fitting RMS error (HU)
No constraint	122597	30.59
Invertibility	0	36.26
Rigidity	0	38.13
Relaxed	341	38.11
Source	3145728	207.28

iterations of the conjugate gradient method with 4 cycles of GNC [8].

4.3.2   Local invertibility and image matching

Figures 4.4, 4.5, 4.6, and 4.7 show the deformed images for each method. No constraint case is the best case in terms of matching the deformed image to the target image. The rest of the results of each method shows plausible deformed images.

Table 4.1 shows these image matchings in a quantitative way. The data fitting RMS error of and between source and target images is 207.28 HU and no constraint case results in 30.59 HU after 300 iterations. However, this also results in 122597 voxel points of negative Jacobian determinant values among 3145728 voxels. Figures 4.8 and 4.9 show projection views of these negative Jacobian determinants.

Applying invertibility penalty [13, 15] (Invertibility) alone and both invertibility and rigidity penalties (Rigidity) achieved 0 negative Jacobian determinant values. However, due to the constraints applied, the data fidelity RMS error values are higher than a case with no constraints. Our proposed method (Relaxed) has 341 negative Jacobian determinant values among 3145728 voxels. This is natural because we intend to allow discontinuities near the interface between the diaphragm and the rib cage. Figure 4.9 shows that the discontinuities appear near the area we expected for most of the cases. This method also achieved a better data fidelity RMS error value (38.11 HU) than the Rigidity method (38.13 HU) since we relaxed an invertibility penalty.

No constraint: Coronal

No constraint: Sagittal

No constraint: Axial
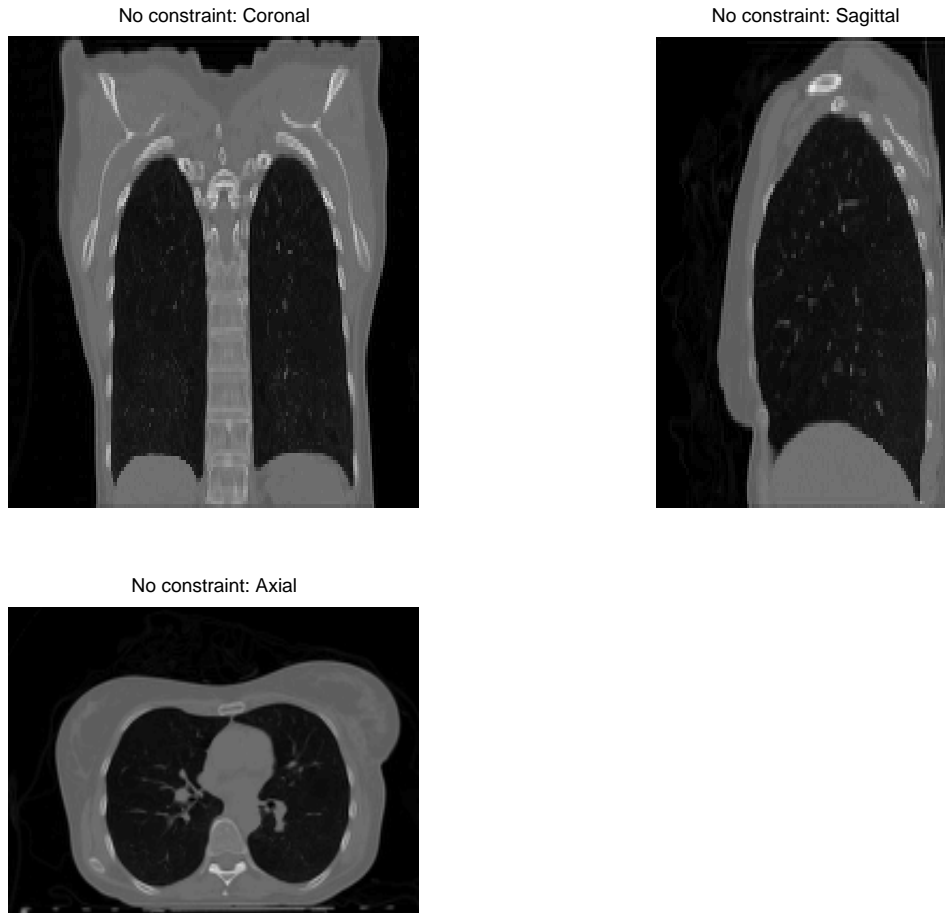
Figure 4.4: Coronal, sagittal and axial views of 3D deformed images with no constraint.
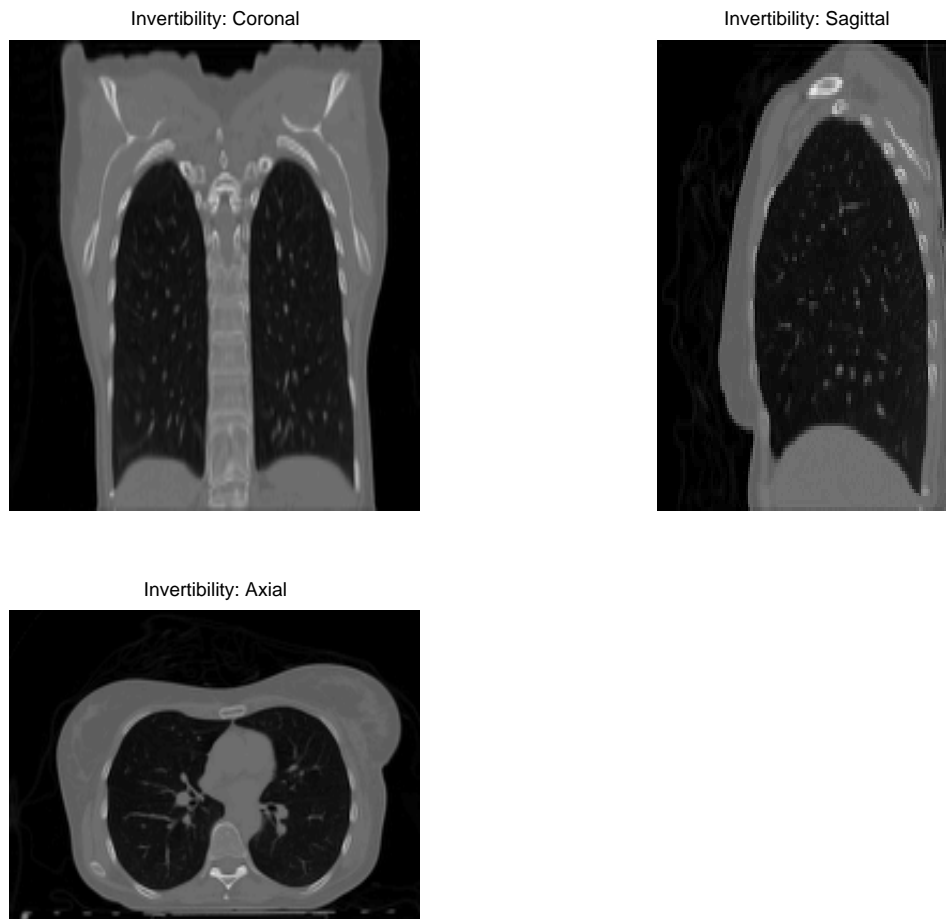
Figure 4.5: Coronal, sagittal and axial views of 3D deformed images with and the invertibility penalty

Ridigity: Coronal

Ridigity: Sagittal

Ridigity: Axial
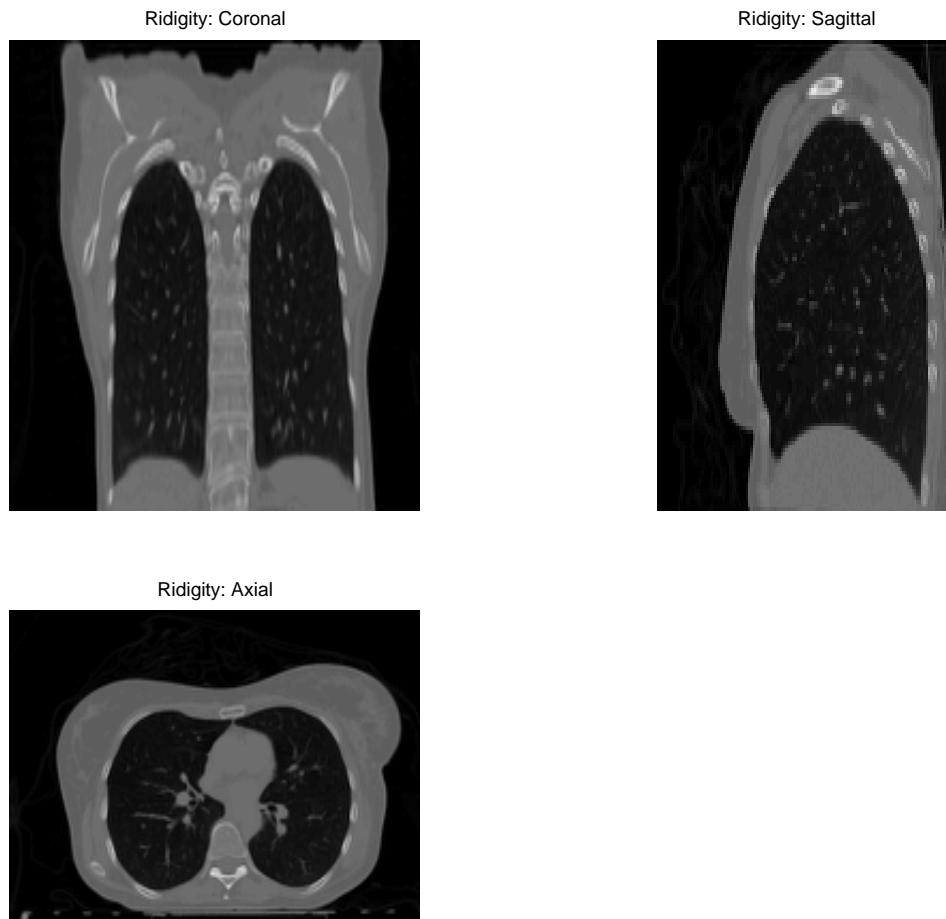
Figure 4.6: Coronal, sagittal and axial views of 3D deformed images with the invertibility and rigidity penalties.
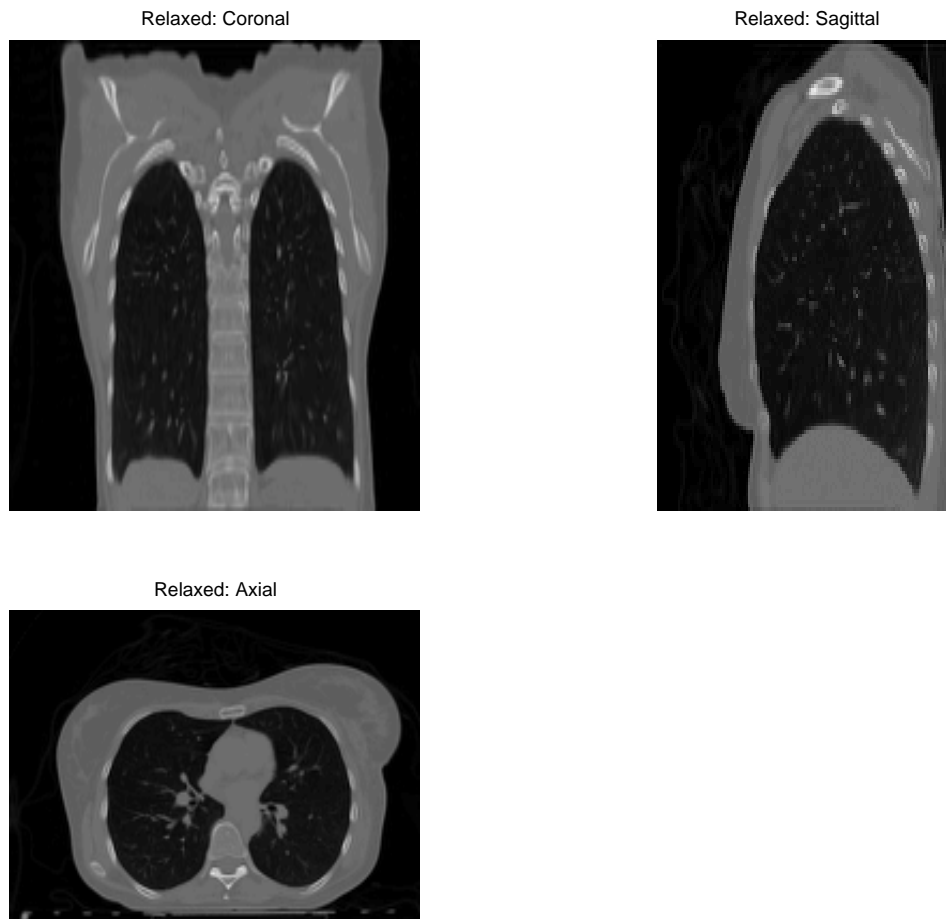
Figure 4.7: Coronal, sagittal and axial views of 3D deformed images with the proposed relaxed invertibility and rigidity penalties.
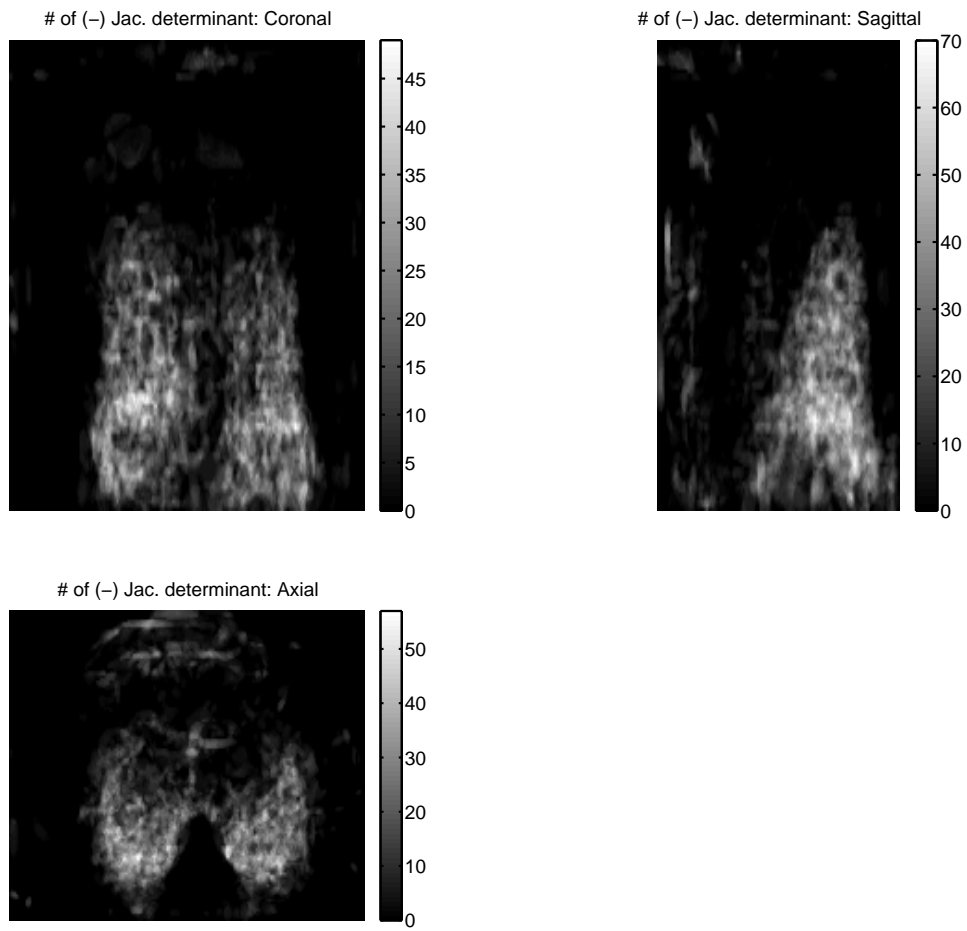
Figure 4.8: Projected coronal, sagittal and axial views of the number of non-positive Jacobian determinant values in no constraint.
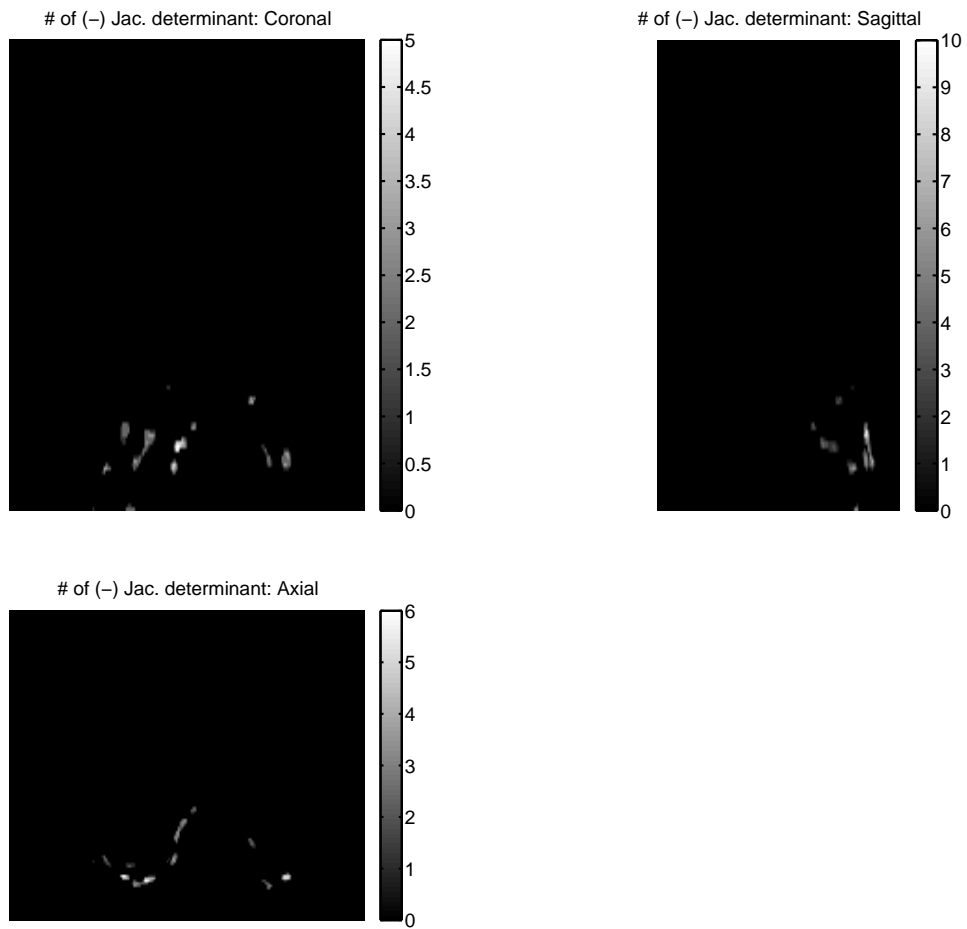
Figure 4.9: Projected coronal, sagittal and axial views of the number of non-positive Jacobian determinant values in the proposed method. Most of negative values in proposed method are near inbetween the rib cage and the diaphragm.

4.3.3 Improved bone registration

Figure 4.4 shows a deformed image very close to an original target image. Bones near the diaphragm in the Invertibility case and the Rigidity case show clear bone warps due to the sliding motion of the diaphragm. In the Rigidity case, too strong rigidity penalty parameter causes the image intensity mismatch between the deformed image and the target image. Whereas too weak rigidity penalty parameter results in more bone warpings. The right rib bone in coronal views went downward in both cases, and the spinal bones are stretched due to a sliding effect. However, Figure 4.7 shows that the bone moving / stretching is corrected. Figure 4.10 shows 3D bone structures for each method and shows that our proposed method corrects bone warps significantly more compared to the invertibility method or the rigidity method.

4.3.4 Sliding effect

Figures 4.12 and 4.13 show quiver plots of deformations for each method in coronal and sagittal views. The no constraint case shows very localized deformations. However, in the case of invertibility penalty, the nearby deformation field is affected by a major downward motion of the diaphragm and we can even observe strong arrows outside the body and inside the spine. However, our proposed method reduced the magnitude of arrows outside the body (and on rib bones) and inside the spine. It seems more realistic to have discontinuous motions near these areas.

4.4 Discussion

This chapter introduces a new relaxed invertibility penalty method as an extension of our previous work [13, 15]. We applied it to a 3D respiratory image registration problem with a rigidity penalty which reduced bone warps significantly with a small sacrifice of lo-

cal invertibility and data fidelity. Estimated deformation near the diaphragm seems more realistic in terms of its discontinuity. However, the determination of parameters for a Geman function may depend on individual patients and investigating this with more patients will be an interesting future study.

Due to the width of the support of cubic B-splines, cubic B-spline based image registration might not be the best way to implement tissue rigidity penalty. Rigid constraint near the support of this basis seems to lead to less flexible data fitting in the area of tissues near bones. More general settings in rigidity penalty [60] and in sliding treatment [83] seem to be another promising future study.

No constraint
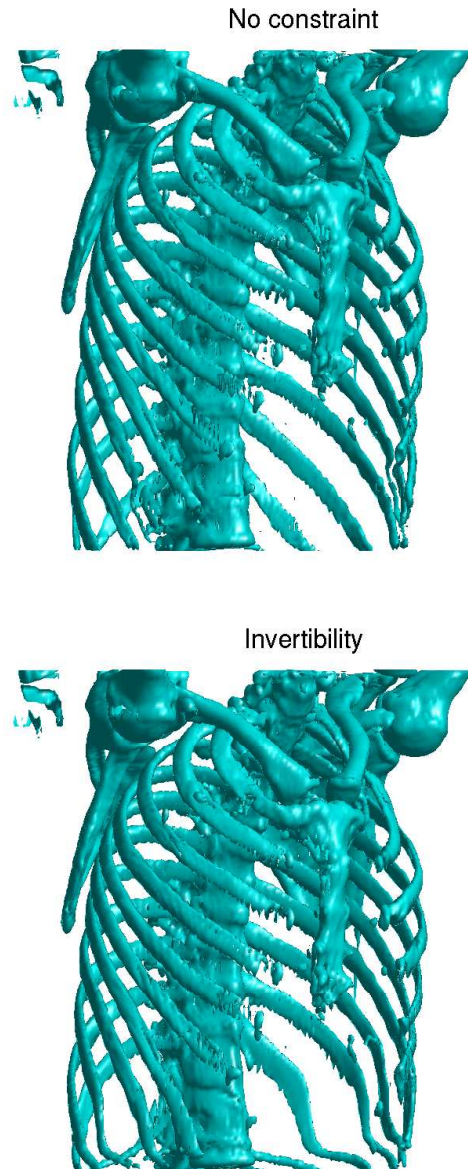
Invertibility

Figure 4.10: 3D bone structures of deformed images for No constraint and Invertibility.

Rigidity

Relaxed
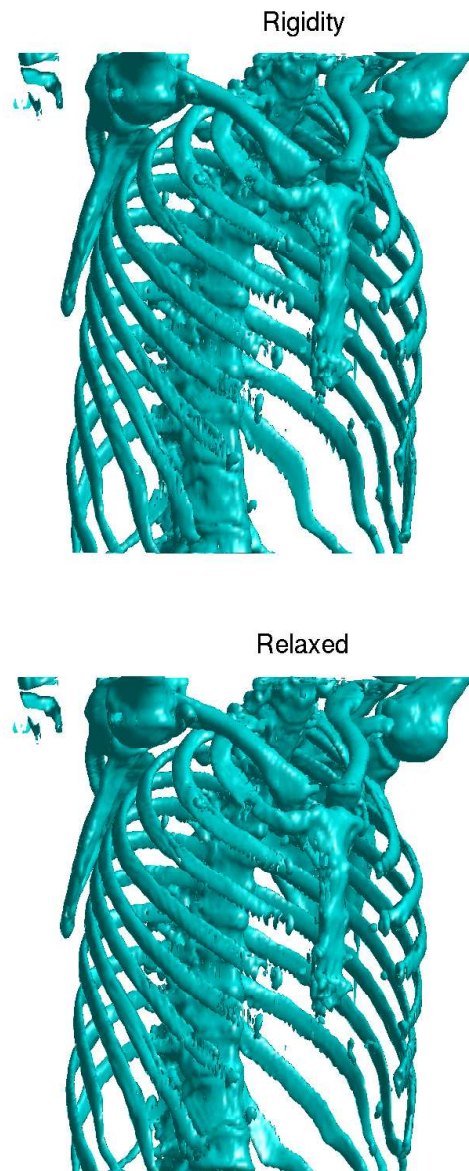
Figure 4.11: 3D bone structures of deformed images for Invertibiliry / Rigidity and Proposed method.

(a) No conatraint

(b) Invertibility

(c) Invertibility / Rigidity

(d) Proposed method

Figure 4.12: Zoomed coronal views of deformed images (LEFT) by using no constraint, invertibility penalty (Invertibility), invertibility / rigidity penalty (Rigidity), and relaxed invertibility / rigidity penalty (Relaxed) and their quiver plots (RIGHT).
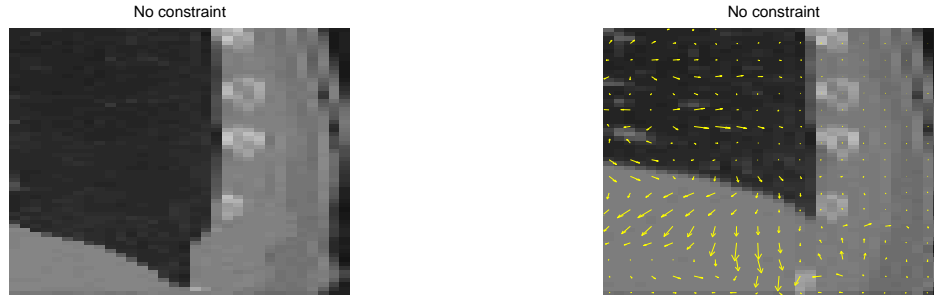
(a) No constraint

(b) Invertibility

(c) Invertibility / Rigidity
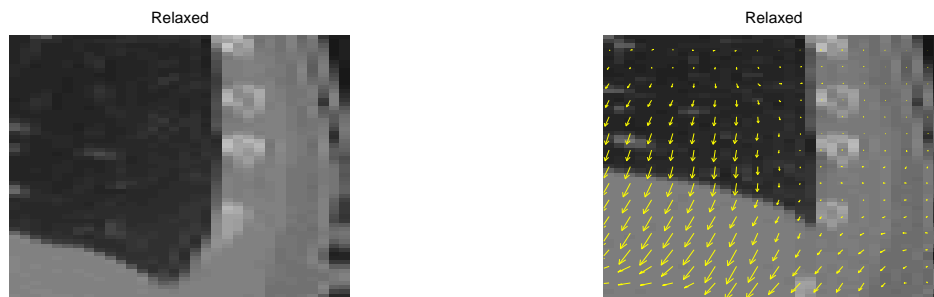
(d) Proposed method

Figure 4.13: Zoomed sagittal views of deformed images (LEFT) by using no constraint, invertibility penalty (Invertibility), invertibility / rigidity penalty (Rigidity), and relaxed invertibility / rigidity penalty (Relaxed) and their quiver plots (RIGHT).

CHAPTER 5

Spatial resolution and noise properties in regularized motion-compensated image reconstruction methods [3]

MCIR methods have great potential to improve image quality in the presence of subject motion. Unlike gated image reconstruction methods [62, 77], MCIR methods use all collected data and unlike an ungated image reconstruction [59], it uses motion information to avoid motion artifacts. There has been a lot of research on MCIR models for different medical imaging modalities to compensate mainly for cardiac or respiratory motion [14, 35, 52, 53, 57, 69, 75, 100].

MCIR methods differ in terms of how they incorporate motion information into image reconstruction frameworks. Many MCIR models have been proposed and investigated: post-reconstruction motion correction (PMC) [6, 19, 46, 103], motion-compensated temporal regularization (MTR) [9, 27, 29, 31, 57], and the parametric motion model (PMM) [14, 35, 52, 53, 69, 75, 100]. Even though each MCIR method has been well-studied separately, there has been less research on the comparison of different MCIR methods. Manjeshwar *et al.* [58] and Thielemans *et al.* [102] compared PMC and PMM in terms of lesion detectibility. Asma *et al.* also compared PMC and PMM theoretically in terms of the bias and covariance of them [5]. However, the analysis used a conventional kappa approxima-

---

[3]This chapter is based on [16].

tion [24] for the noise comparison so it was limited. Zibetti *et al.* compared MTR and PMM empirically in the super-resolution (SR) application [113, 115].

The spatial resolution and noise analyses for different MCIR models may be the first step for the *fair* comparison of them. Only after we approximately match the spatial resolutions of different MCIR methods, it is meaningful to compare their noise performance. The spatial resolution and noise properties have been well-studied for for static image reconstruction [1, 23, 24, 74, 89, 94] and dynamic image reconstruction [4]. This chapter investigates the spatial resolution and noise properties of PMC, PMM, and MTR carefully, extending [24] to MCIR methods [16]. For known nonrigid motion, we analyse the statistical properties of different MCIR models and compare them. This analysis can be an initial step to the performance analysis of joint MCIR methods. This analysis may be still useful since known motion may be reasonably realistic for some multi-modal medical imaging applications such as PET/CT [2, 53] and PET/MR.

This chapter is organized as follows. Section 5.1 studies three different MCIR models and estimators [25, 35, 46, 57, 115]. It shows how one estimator is related to another estimator. Section 5.2 investigates the spatial resolution properties of each MCIR estimator and discusses the spatial regularizer designs that provide approximately uniform spatial resolution and resolution matching. Section 5.3 derives the noise properties with given uniform spatial resolution and compares them. Section 5.4 shows some 2D tomography (PET) simulations with known nonrigid motion to illustrate the theory.

5.1 Motion-compensated image reconstructions

We consider three different types of MCIR methods: post-reconstruction motion correction (PMC) [6, 19, 34, 46, 103], parametric motion model (PMM) [7, 14, 20, 25, 35, 52–54, 65, 66, 69, 75, 79, 100] and motion-compensated temporal regularization (MTR) [9, 27,

57, 113, 115]. Here we treat the nonrigid motion information as predetermined (known). One can determine the motion information from the measurements $\boldsymbol{y}_m$ or from other measurements, *e.g.*, from CT in PET/CT system or MR in PET/MR system.

5.1.1 Post-reconstruction motion correction (PMC)

Often one can reconstruct each image $\hat{\boldsymbol{f}}_m$ from the corresponding measurement $\boldsymbol{y}_m$ based on (2.1) and some prior knowledge (*e.g.*, a smoothness prior). For simplicity, here we focus on a penalized weighted least square (PWLS) estimator [22] with a quadratic penalty as follows:

$$\hat{\boldsymbol{f}}_m = \underset{\boldsymbol{f}_m}{\operatorname{argmin}} \|\boldsymbol{y}_m - \boldsymbol{A}_m \boldsymbol{f}_m\|_{\boldsymbol{W}_m}^2 + \eta \|\boldsymbol{C}_m \boldsymbol{f}_m\|_2^2 \tag{5.1}$$

where $\boldsymbol{W}_m$ is a weight matrix that approximates the inverse of the covariance of $\boldsymbol{y}_m$, η is a spatial regularization parameter, and typically $\boldsymbol{C}_m$ is a finite-difference matrix. The analysis is easily generalized to other noise models [24].

The estimators $\hat{\boldsymbol{f}}_m$ in (5.1) can be expressed as:

$$\hat{\boldsymbol{f}}_m = [\boldsymbol{F}_m + \eta \boldsymbol{R}_m]^{-1} \boldsymbol{A}_m' \boldsymbol{W}_m \boldsymbol{y}_m, \quad m = 1, \cdots, M \tag{5.2}$$

where

$$\boldsymbol{F}_m \triangleq \boldsymbol{A}_m' \boldsymbol{W}_m \boldsymbol{A}_m \tag{5.3}$$

and $\boldsymbol{R}_m \triangleq \boldsymbol{C}_m' \boldsymbol{C}_m$. Once $\hat{\boldsymbol{f}}_1, \dots \hat{\boldsymbol{f}}_M$ are reconstructed, one way to improve the SNR would be to average all of them. However, the resulting image would be contaminated by motion blur.

One way to reduce motion artifacts is to use the motion information to map each image $\boldsymbol{f}_m$ to a single image. Without loss of generality, we chose $\boldsymbol{f}_1$ as our target image to

reconstruct. Then, using (2.10) and (5.2), a natural definition for the PMC approach is

$$\hat{\boldsymbol{f}}_{\mathrm{PMC}} \triangleq \frac{1}{M} \sum_{m=1}^{M} \boldsymbol{T}_{1,m} \hat{\boldsymbol{f}}_m \tag{5.4}$$

$$= \frac{1}{M} \sum_{m=1}^{M} \boldsymbol{T}_{1,m} [\boldsymbol{F}_m + \eta \boldsymbol{R}_m]^{-1} \boldsymbol{A}_m' \boldsymbol{W}_m \boldsymbol{y}_m.$$

For later convenience, we use (2.13) to rewrite (5.4) as follows

$$\hat{\boldsymbol{f}}_{\mathrm{PMC}} = \frac{1}{M} \sum_{m=1}^{M} [\breve{\boldsymbol{F}}_m + \eta \breve{\boldsymbol{R}}_m]^{-1} \boldsymbol{T}_{m,1}' \boldsymbol{A}_m' \boldsymbol{W}_m \boldsymbol{y}_m \tag{5.5}$$

where $\breve{\boldsymbol{F}}_m \triangleq \boldsymbol{T}_{m,1}'\boldsymbol{F}_m\boldsymbol{T}_{m,1}$ and $\breve{\boldsymbol{R}}_m \triangleq \boldsymbol{T}_{m,1}'\boldsymbol{R}_m\boldsymbol{T}_{m,1}$.

5.1.2 Parametric motion model (PMM)

For PMM, we first need to choose a reference image frame among $\{\boldsymbol{f}_1, \cdots, \boldsymbol{f}_M\}$. Without loss of generality, we assume that $\boldsymbol{f}_1$ is our reference image frame. Then, combining the measurement model (2.1) with (2.10) yields a new measurement model that depends only on the image $\boldsymbol{f}_1$ instead of the all images $\boldsymbol{f}_m$:

$$\boldsymbol{y}_m = \boldsymbol{A}_m \boldsymbol{T}_{m,1} \boldsymbol{f}_1 + \boldsymbol{\epsilon}_m, \quad m = 1, \ldots, M.$$

Stacking up these models yields the overall model

$$\boldsymbol{y}_{\mathrm{c}} = \boldsymbol{A}_{\mathrm{d}} \boldsymbol{T}_{\mathrm{c}} \boldsymbol{f}_1 + \boldsymbol{\epsilon}_{\mathrm{c}}, \tag{5.6}$$

where

$$\boldsymbol{y}_{\mathrm{c}} = [\boldsymbol{y}_1', \cdots, \boldsymbol{y}_M']',$$

$$\boldsymbol{A}_{\mathrm{d}} = \mathrm{diag}\{\boldsymbol{A}_1, \cdots, \boldsymbol{A}_M\},$$

$$\boldsymbol{T}_{\mathrm{c}} = [\boldsymbol{T}_{1,1}', \cdots, \boldsymbol{T}_{M,1}']',$$

$$\boldsymbol{\epsilon}_{\mathrm{c}} = [\boldsymbol{\epsilon}_1', \cdots, \boldsymbol{\epsilon}_M']'.$$

The PWLS estimator for the measurement model (5.6) is

$$
\begin{aligned}
\hat{\boldsymbol{f}}_{\text{PMM}} &= \operatorname*{argmin}_{\boldsymbol{f}_1} \|\boldsymbol{y}_{\text{c}} - \boldsymbol{A}_{\text{d}}\boldsymbol{T}_{\text{c}}\boldsymbol{f}_1\|^2_{\boldsymbol{W}_{\text{d}}} + \eta\|\boldsymbol{C}_1\boldsymbol{f}_1\|^2_2 \\
&= [\boldsymbol{T}'_{\text{c}}\boldsymbol{F}_{\text{d}}\boldsymbol{T}_{\text{c}} + \eta\boldsymbol{R}_1]^{-1}\boldsymbol{T}'_{\text{c}}\boldsymbol{A}'_{\text{d}}\boldsymbol{W}_{\text{d}}\boldsymbol{y}_{\text{c}},
\end{aligned}
\tag{5.7}
$$

where $\boldsymbol{W}_{\text{d}}$ is a weight matrix that approximates the inverse of the covariance of $\boldsymbol{y}_{\text{c}}$, *i.e.*, $\boldsymbol{W}_{\text{d}} = \operatorname{diag}\{\boldsymbol{W}_1, \cdots, \boldsymbol{W}_M\}$ and $\boldsymbol{F}_{\text{d}} \triangleq \boldsymbol{A}'_{\text{d}}\boldsymbol{W}_{\text{d}}\boldsymbol{A}_{\text{d}}$, which is a block-diagonal matrix of $\boldsymbol{F}_m$, *i.e.*, $\operatorname{diag}\{\boldsymbol{F}_1, \cdots, \boldsymbol{F}_M\}$. Note that

$$
\boldsymbol{F}_{\text{c}} \triangleq \boldsymbol{T}'_{\text{c}}\boldsymbol{F}_{\text{d}}\boldsymbol{T}_{\text{c}} = \sum_{m=1}^{M} \boldsymbol{T}'_{m,1}\boldsymbol{F}_m\boldsymbol{T}_{m,1} = \sum_{m=1}^{M} \breve{\boldsymbol{F}}_m.
$$

Then, one can rewrite (5.7) as follows:

$$
\hat{\boldsymbol{f}}_{\text{PMM}} = \left[\sum_{m=1}^{M} \breve{\boldsymbol{F}}_m + \eta\boldsymbol{R}_1\right]^{-1} \sum_{m=1}^{M} \boldsymbol{T}'_{m,1}\boldsymbol{A}'_m\boldsymbol{W}_m\boldsymbol{y}_m.
\tag{5.8}
$$

5.1.3   Motion-compensated temporal regularization (MTR)

The MTR method exploits the motion information that matches two adjacent images as a penalty:

$$
\|\boldsymbol{f}_{m+1} - \boldsymbol{T}_{m+1,m}\boldsymbol{f}_m\|^2_2.
\tag{5.9}
$$

where $m = 1, \cdots, M - 1$. This penalty is added to the cost function in (5.1) to define the MTR cost function.

Equations (5.1) and (5.9) can be represented in a simpler vector-matrix notation. First, rewrite (2.1) as follows:

$$
\boldsymbol{y}_{\text{c}} = \boldsymbol{A}_{\text{d}}\boldsymbol{f}_{\text{c}} + \boldsymbol{\epsilon}_{\text{c}},
\tag{5.10}
$$

where $\boldsymbol{f}_{\text{c}} = [\boldsymbol{f}'_1, \cdots, \boldsymbol{f}'_M]'$. One can use (5.10) with any statistical image reconstruction objective function. We focus here on PWLS as follows:

$$
\begin{aligned}
\hat{\boldsymbol{f}}_{\text{c}} &= \operatorname*{argmin}_{\boldsymbol{f}_{\text{c}}} \|\boldsymbol{y}_{\text{c}} - \boldsymbol{A}_{\text{d}}\boldsymbol{f}_{\text{c}}\|^2_{\boldsymbol{W}_{\text{d}}} + \eta\|\boldsymbol{C}_{\text{d}}\boldsymbol{f}_{\text{c}}\|^2_2 + \zeta\|\boldsymbol{T}_{\text{circ}}\boldsymbol{f}_{\text{c}}\|^2_2 \\
&= \boldsymbol{H}^{-1}_{\text{MTR}}\boldsymbol{A}'_{\text{d}}\boldsymbol{W}_{\text{d}}\boldsymbol{y}_{\text{c}},
\end{aligned}
\tag{5.11}
$$

where $C_d = \operatorname{diag}\{C_1, \cdots, C_M\}$, ζ is a temporal regularization parameter,

$$
\boldsymbol{T}_{\mathrm{circ}} \triangleq \begin{bmatrix} -\boldsymbol{T}_{2,1} & \boldsymbol{I} & & \\ & \ddots & \ddots & \\ & & -\boldsymbol{T}_{M,M-1} & \boldsymbol{I} \end{bmatrix}, \tag{5.12}
$$

and $\boldsymbol{H}_{\mathrm{MTR}} \triangleq \boldsymbol{F}_d + \eta \boldsymbol{C}_d' \boldsymbol{C}_d + \zeta \boldsymbol{T}_{\mathrm{circ}}' \boldsymbol{T}_{\mathrm{circ}}$. Therefore,

$$
\begin{aligned}
\hat{\boldsymbol{f}}_{\mathrm{MTR}} &= \begin{bmatrix} \boldsymbol{I} & \boldsymbol{0} & \cdots & \boldsymbol{0} \end{bmatrix} \hat{\boldsymbol{f}}_c \\
&= \begin{bmatrix} \boldsymbol{I} & \boldsymbol{0} & \cdots & \boldsymbol{0} \end{bmatrix} \boldsymbol{H}_{\mathrm{MTR}}^{-1} \boldsymbol{A}_d' \boldsymbol{W}_d \boldsymbol{y}_c.
\end{aligned} \tag{5.13}
$$

We may also modify $\boldsymbol{T}_{\mathrm{circ}}$ for periodic (or pseudo-periodic) image sequences by assuming that $\boldsymbol{T}_{M+1,M} \triangleq \boldsymbol{T}_{1,M}$ and $\boldsymbol{f}_{M+1} \triangleq \boldsymbol{f}_1$.

5.1.4 Limits of MTR estimator for ζ

The temporal regularization term (5.9) in (5.11) will increase the correlation between the estimators $\hat{c}_i$ and $\hat{c}_j$ for $i \neq j$ as ζ increases. We investigate the limiting behavior of the MTR estimator as $\zeta \to 0$ and as $\zeta \to \infty$.

It is easy to see the limit of $\hat{\boldsymbol{f}}_c$ as $\zeta \to 0$ since

$$
\boldsymbol{H}_{\mathrm{MTR}} \to \boldsymbol{F}_d + \eta \boldsymbol{C}_d' \boldsymbol{C}_d \triangleq \boldsymbol{F}_{\mathrm{MTR}}
$$

where $\boldsymbol{F}_{\mathrm{MTR}}$ is block-diagonal. The inverse of $\boldsymbol{F}_{\mathrm{MTR}}$ is $\boldsymbol{F}_{\mathrm{MTR}}^{-1} = \operatorname{diag}\{(\boldsymbol{F}_m + \eta \boldsymbol{R}_m)^{-1}\}_{m=1}^M$. Therefore, the MTR estimator $\hat{\boldsymbol{f}}_c$ will be

$$
\hat{\boldsymbol{f}}_c \to \boldsymbol{F}_{\mathrm{MTR}}^{-1} \boldsymbol{A}_d' \boldsymbol{W}_d \boldsymbol{y}_c = \begin{bmatrix} \hat{\boldsymbol{f}}_1 \\ \vdots \\ \hat{\boldsymbol{f}}_M \end{bmatrix}, \tag{5.14}
$$

and therefore, $\hat{\boldsymbol{f}}_{\mathrm{MTR}} \to \hat{\boldsymbol{f}}_1$ as $\zeta \to 0$. In other words, as $\zeta \to 0$, the MTR estimator for each frame is the same as separate (single frame) image reconstruction in (5.1).

$\hat{\boldsymbol{f}}_{\mathrm{c}}$ has more interesting behavior as $\zeta \to \infty$. To see this, we need to treat the null space of $\boldsymbol{R}_{\mathrm{circ}} \triangleq \boldsymbol{T}_{\mathrm{circ}}'\boldsymbol{T}_{\mathrm{circ}}$ carefully. Since $\boldsymbol{R}_{\mathrm{circ}}$ is symmetric nonnegative definite, it has an orthonormal eigen-decomposition of the form

$$\boldsymbol{R}_{\mathrm{circ}} = [\boldsymbol{U}_1 \quad \boldsymbol{U}_0] \begin{bmatrix} \boldsymbol{\Sigma}_1 & \boldsymbol{0} \\ \boldsymbol{0} & \boldsymbol{0} \end{bmatrix} [\boldsymbol{U}_1 \quad \boldsymbol{U}_0]'$$

where $\boldsymbol{U}_1$, $\boldsymbol{U}_0$ are unitary matrices and $\boldsymbol{\Sigma}_1 \succ \boldsymbol{0}$. The columns of the matrix $\boldsymbol{U}_0$ span the null space of $\boldsymbol{R}_{\mathrm{circ}}$. From the definition of $\boldsymbol{T}_{\mathrm{circ}}$, it is easy to see that the null space of $\boldsymbol{R}_{\mathrm{circ}}$ consists of images that satisfiy the following condition:

$$\begin{align}
\boldsymbol{f}_2 &= \boldsymbol{T}_{2,1}\boldsymbol{f}_1 \tag{5.15} \\
\boldsymbol{f}_3 &= \boldsymbol{T}_{3,2}\boldsymbol{T}_{2,1}\boldsymbol{f}_1 \\
&\vdots \\
\boldsymbol{f}_M &= \boldsymbol{T}_{M,M-1}\cdots\boldsymbol{T}_{2,1}\boldsymbol{f}_1,
\end{align}$$

for any image $\boldsymbol{f}_1$. In other words, the $MN \times MN$ matrix $\boldsymbol{R}_{\mathrm{circ}}$ has a null space of at least dimension N. In contrast, the spatial regularizer $\boldsymbol{C}_{\mathrm{d}}$ usually has a null space only of dimension 1. A system of equations (5.15) becomes

$$\boldsymbol{f}_{\mathrm{c}} = \begin{bmatrix} \boldsymbol{T}_{2,1} \\ \boldsymbol{T}_{3,2}\boldsymbol{T}_{2,1} \\ \vdots \\ \boldsymbol{T}_{M,M-1}\cdots\boldsymbol{T}_{2,1} \end{bmatrix} \boldsymbol{f}_1 \triangleq \tilde{\boldsymbol{T}}_{\mathrm{c}}\boldsymbol{f}_1. \tag{5.16}$$

When we add a periodic condition

$$\boldsymbol{f}_1 = \boldsymbol{T}_{1,M}\boldsymbol{f}_M \tag{5.17}$$

to (5.12), we assume that (5.17) is linearly dependent on (5.15). In this case, $\boldsymbol{R}_{\mathrm{circ}}$ still has a null space of at least dimension N. We can construct the matrix $\boldsymbol{U}_0$ as follows:

$$\boldsymbol{U}_0 = \tilde{\boldsymbol{T}}_{\mathrm{c}}\left(\tilde{\boldsymbol{T}}_{\mathrm{c}}'\tilde{\boldsymbol{T}}_{\mathrm{c}}\right)^{-1/2} \triangleq \tilde{\boldsymbol{T}}_{\mathrm{c}}\boldsymbol{S} \tag{5.18}$$

where $\tilde{T}_{\mathrm{c}}^{'}\tilde{T}_{\mathrm{c}} \succ 0$ because $\tilde{T}_{\mathrm{c}}^{'}\tilde{T}_{\mathrm{c}} = I + \sum_{m=2}^{M}(T_{m,m-1}\cdots T_{2,1})'T_{m,m-1}\cdots T_{2,1}$ and I is positive definite. Thus, S is invertible.

Under the usual assumption that F_1 and R_1 have disjoint null spaces, one can verify that

$$B \triangleq U_0' F_{\mathrm{MTR}} U_0 \succ 0.$$

To proceed, we express F_{MTR} as follows:

$$[U_1 \quad U_0]' F_{\mathrm{MTR}} [U_1 \quad U_0] = \begin{bmatrix} N & M' \\ M & B \end{bmatrix}.$$

Note that even though Σ_1 is diagonal, N and B are not diagonal in general. Thus,

$$[F_{\mathrm{MTR}} + \zeta R_{\mathrm{circ}}]^{-1} = U \begin{bmatrix} N + \zeta\Sigma_1 & M' \\ M & B \end{bmatrix}^{-1} U'$$

where $U = [U_1 \quad U_0]$. By Schur complement [28], we have

$$[F_{\mathrm{MTR}} + \zeta R_{\mathrm{circ}}]^{-1} =$$

$$U \begin{bmatrix} \Delta & -\Delta M' B^{-1} \\ -B^{-1} M \Delta & B^{-1} + B^{-1} M \Delta M' B^{-1} \end{bmatrix} U'$$

where $\Delta = [N + \zeta\Sigma_1 - M'B^{-1}M]^{-1}$. Since Σ_1 is positive definite, $\Delta \to 0$ as $\zeta \to \infty$. Thus,

$$H_{\mathrm{MTR}}^{-1} = [F_{\mathrm{MTR}} + \zeta R_{\mathrm{circ}}]^{-1} \to U_0 B^{-1} U_0'. \tag{5.19}$$

Therefore, the MTR estimator $\hat{f}_{\mathrm{c}}$ becomes

$$\hat{f}_{\mathrm{c}} \to \tilde{T}_{\mathrm{c}}[\tilde{T}_{\mathrm{c}}^{'} F_{\mathrm{MTR}} \tilde{T}_{\mathrm{c}}]^{-1} \tilde{T}_{\mathrm{c}}^{'} A_{\mathrm{d}}' W_{\mathrm{d}} y_{\mathrm{c}} \tag{5.20}$$

as $\zeta \to \infty$. In other words, the MTR estimator $\hat{f}_{\mathrm{c}}$ goes to

$$\begin{aligned} \hat{f}_{\mathrm{c}} &\to \tilde{T}_{\mathrm{c}}[F_{\mathrm{c}} + \eta\tilde{R}_{\mathrm{c}}]^{-1} \tilde{T}_{\mathrm{c}}^{'} A_{\mathrm{d}}' W_{\mathrm{d}} y_{\mathrm{c}} \tag{5.21} \\ &= \tilde{T}_{\mathrm{c}} \left[\sum_{m=1}^{M} \breve{F}_m + \eta\breve{R}_m \right]^{-1} \sum_{m=1}^{M} T_{m,1}' A_m' W_m y_m \end{aligned}$$

where $\tilde{\boldsymbol{R}}_\mathrm{c} = \tilde{\boldsymbol{T}}_\mathrm{c}{}'\boldsymbol{C}_\mathrm{d}'\boldsymbol{C}_\mathrm{d}\tilde{\boldsymbol{T}}_\mathrm{c}$.

The dimension of the null space for $\boldsymbol{R}_\mathrm{circ}$ is greater than or equal to the dimension of $\boldsymbol{f}_1$. Therefore, (5.21) may always have the nonzero estimated image and is not biased due to large ζ.

5.1.5   Comparison of different MCIR estimators

Observing the limit behavior of the MTR estimator shows that MTR estimator (5.14) is equivalent to a separate PWLS estimator (5.2) as $\zeta \to 0$. For $\zeta \to \infty$ case, we can show the relationship between (5.20) and (5.8) as we assume that $\boldsymbol{T}_{j,i}$ is transitive. In this case, $\tilde{\boldsymbol{T}}_\mathrm{c}$ becomes $\boldsymbol{T}_\mathrm{c}$. In practice, getting exactly transitive deformations is challenging [90]. Then, we can show that

$$\hat{\boldsymbol{f}}_\mathrm{MTR} \to \hat{\boldsymbol{f}}_\mathrm{PMM} \quad \text{as} \quad \zeta \to \infty, \tag{5.22}$$

when $\eta = 0$. If the regularizers $\boldsymbol{R}_1$ and $\sum_{m=1}^{M} \breve{\boldsymbol{R}}_m$ are designed carefully, then (5.22) may be true for $\eta \neq 0$. So, for known motion, the MTR estimators $\hat{\boldsymbol{f}}_\mathrm{c}$ for all frames can be obtained by simple warps of $\hat{\boldsymbol{f}}_\mathrm{PMM}$ as follows:

$$\hat{\boldsymbol{f}}_\mathrm{c} = \boldsymbol{T}_\mathrm{c}\hat{\boldsymbol{f}}_\mathrm{PMM} \tag{5.23}$$

when $\zeta \to \infty$.

For PMC estimator (5.4), we used an unweighted average of the motion corrected estimators of all frames. The MTR estimator for $\zeta \to \infty$ (and the PMM estimator) can be interpreted as a *weighted* average of all estimators from all frames as follows:

$$\begin{aligned}
\hat{\boldsymbol{f}}_\mathrm{MTR} \quad &\to \quad \left[\sum_{m=1}^{M} \breve{\boldsymbol{F}}_m + \eta\breve{\boldsymbol{R}}_m\right]^{-1} \sum_{m=1}^{M} \boldsymbol{T}_{m,1}'\boldsymbol{A}_m'\boldsymbol{W}_m\boldsymbol{y}_m \\
&= \quad \sum_{m=1}^{M} \boldsymbol{\Gamma}_m\boldsymbol{T}_{1,m}(\boldsymbol{F}_m + \eta\boldsymbol{R}_m)^{-1}\boldsymbol{A}_m'\boldsymbol{W}_m\boldsymbol{y}_m \\
&= \quad \sum_{m=1}^{M} \boldsymbol{\Gamma}_m\hat{\boldsymbol{f}}_m,
\end{aligned} \tag{5.24}$$

where the weighting matrices are given by

$$\mathbf{\Gamma}_m \triangleq \left[\sum_{l=1}^{M} \breve{\boldsymbol{F}}_l + \eta \breve{\boldsymbol{R}}_l \right]^{-1} (\breve{\boldsymbol{F}}_m + \eta \breve{\boldsymbol{R}}_m).$$

The PMM and MTR with large ζ give more weight to estimators $\hat{\boldsymbol{f}}_m$ depending on factors such as high certainty (Fisher information matrix $\boldsymbol{F}_m$), motion $\boldsymbol{T}_{m,1}$ and regularization.

5.2 Spatial resolution properties

Spatial resolution depends on many factors in an imaging system, so analyzing it usually requires system-specific information. In this section, we provide a way to match the spatial resolutions of each MCIR method so that we can fairly compare the noise properties with the same (or similar) bias. Since it is hard to deal with the many different factors that cause spatial resolution non-uniformity, we focus on an ideal tomography system for our analysis, *i.e.*, no detector blur.

For the analysis in this section, we assume $\boldsymbol{A}_m = \boldsymbol{A}_0$ for all m, but we allow the warp $\boldsymbol{T}_{m,1}$ and the statistical weights $\boldsymbol{W}_m$ to differ for each m. Some PET and CT scans satisfy these assumptions. We also assume that we are using the first-order difference matrix $\boldsymbol{C}_m$ as a spatial regularizer (penalizing x and y directions in 2D).

5.2.1 Separate image reconstruction

Since we will be providing methods to approximately match the spatial resolution of MCIR methods with the spatial resolution of a reconstructed image of each frame separately, we first briefly review the methods for providing uniform spatial resolution of a separate image reconstruction [24].

The expected value of (5.2) for m is

$$\mathsf{E}\{\hat{\boldsymbol{f}}_m\} = [\boldsymbol{F}_m + \eta \boldsymbol{R}_m]^{-1} \boldsymbol{F}_m \boldsymbol{f}_m. \tag{5.25}$$

We are interested in the local impulse response (LIR) at jth pixel and the corresponding LIR l_m^j can be obtained from the expected value of the estimator as follows:

$$l_m^j = [\boldsymbol{F}_m + \eta \boldsymbol{R}_m]^{-1} \boldsymbol{F}_m \delta^j. \tag{5.26}$$

A continuous-space analogue to rewrite (5.26) as the local frequency response at jth pixel is as follows [89]:

$$\frac{\omega_m^j(\Phi)/|\rho|}{\omega_m^j(\Phi)/|\rho| + \eta R_m^j(\rho, \Phi)} \tag{5.27}$$

$\omega_m^j(\Phi)$ is a weight from $\boldsymbol{W}_m$, and $R_m^j(\rho, \Phi)$ is from $\boldsymbol{C}_m$. When $\boldsymbol{C}_m$ is the first-order difference matrix $\boldsymbol{C}_0$, then $R_m^j(\rho, \Phi) = (2\pi\rho)^2$. Note that this local frequency response (5.27) depends on $\omega_m^j(\Phi)$, which is local shift variant.

To approximately provide uniform spatial resolution, we apply spatial regularizers [24] $\boldsymbol{C}_m$ such that

$$\boldsymbol{C}_m \triangleq \boldsymbol{C}_0 \boldsymbol{D}(\underline{\kappa}_m) \tag{5.28}$$

where

$$[\underline{\kappa}_m]_j \triangleq \sqrt{[\boldsymbol{A}_0' \boldsymbol{W}_m \mathbf{1}]_j / [\boldsymbol{A}_0' \mathbf{1}]_j}, \tag{5.29}$$

and $\mathbf{1} = \begin{bmatrix} 1 & 1 & \cdots & 1 \end{bmatrix}'$. Note that we assumed $\boldsymbol{A}_m = \boldsymbol{A}_0$ for all m. Since we can approximate

$$\boldsymbol{F}_m = \boldsymbol{A}_0' \boldsymbol{W}_m \boldsymbol{A}_0 \approx \boldsymbol{D}(\underline{\kappa}_m) \boldsymbol{A}_0' \boldsymbol{A}_0 \boldsymbol{D}(\underline{\kappa}_m) = \boldsymbol{D}(\underline{\kappa}_m) \boldsymbol{F}_0 \boldsymbol{D}(\underline{\kappa}_m), \tag{5.30}$$

(5.25) becomes

$$\mathsf{E}\{\hat{\boldsymbol{f}}_m\} \approx \boldsymbol{D}(\underline{\kappa}_m)^{-1} [\boldsymbol{F}_0 + \eta \boldsymbol{R}_0]^{-1} \boldsymbol{F}_0 \boldsymbol{D}(\underline{\kappa}_m) \boldsymbol{f}_m \tag{5.31}$$

where $\boldsymbol{F}_0 = \boldsymbol{A}_0' \boldsymbol{A}_0$ and $\boldsymbol{R}_0 = \boldsymbol{C}_0' \boldsymbol{C}_0$. Note that (5.30) is a local approximation near jth pixel where we are interested in and since $\underline{\kappa}_m$ values are smoothly varying, the approximation in (5.30) is reasonable. Then, one can cancel out $\boldsymbol{D}(\underline{\kappa}_m)^{-1}$ and $\boldsymbol{D}(\underline{\kappa}_m)$ in (5.31) since one can approximate $[\boldsymbol{F}_0 + \eta \boldsymbol{R}_0]^{-1} \boldsymbol{F}_0$ as nearly diagonal. Therefore, using the modified

regularizer in (5.28),

$$E\{\hat{\boldsymbol{f}}_m\} \approx [\boldsymbol{F}_0 + \eta\boldsymbol{R}_0]^{-1}\boldsymbol{F}_0\boldsymbol{f}_m \tag{5.32}$$

and the corresponding local frequency response of a continuous-space analogue for (5.32)

becomes

$$\frac{1/|\rho|}{1/|\rho| + \eta(2\pi\rho)^2}, \tag{5.33}$$

which is now local shift invariant. We use this form below when considering the effects of

motion.

5.2.2 Post-reconstruction motion correction

The expected value of the PMC estimator (5.4) is the sum of each expected value $\hat{\boldsymbol{f}}_m$

since the expectation operator is linear. So, the expected value of $\hat{\boldsymbol{f}}_{\mathrm{PMC}}$ is

$$E\{\hat{\boldsymbol{f}}_{\mathrm{PMC}}\} = \frac{1}{M}\sum_{m=1}^{M}\boldsymbol{T}_{1,m}[\boldsymbol{F}_m + \eta\boldsymbol{R}_m]^{-1}\boldsymbol{F}_m\boldsymbol{f}_m \tag{5.34}$$

since $E\{\boldsymbol{y}_m\} = \boldsymbol{A}_m\boldsymbol{f}_m$. Applying the modified spatial regularizer $\boldsymbol{C}_m$ in (5.28) for each

frame of (5.34) and using (5.32) shows that

$$E\{\hat{\boldsymbol{f}}_{\mathrm{PMC}}\} \approx \frac{1}{M}\sum_{m=1}^{M}\boldsymbol{T}_{1,m}[\boldsymbol{F}_0 + \eta\boldsymbol{R}_0]^{-1}\boldsymbol{F}_0\boldsymbol{T}_{m,1}\boldsymbol{f}_1 \tag{5.35}$$

where we substitute $\boldsymbol{f}_m$ with $\boldsymbol{T}_{m,1}\boldsymbol{f}_1$.

Since the original system response $[\boldsymbol{F}_0 + \eta\boldsymbol{R}_0]^{-1}\boldsymbol{F}_0$ is sandwiched in between $\boldsymbol{T}_{1,m}$

and $\boldsymbol{T}_{m,1}$ operators in (5.35), the nature of the system response may change due to mo-

tion effects. We are interested in nonrigid motion and assume that the motion is locally

affine. Since the original system response is space invariant, without loss of generality,

we assume the local linear transformation at the jth pixel. However, dealing with general

linear transformations poses a challenge that may require designing a regularizer with dif-

ferent weights according along different directions [89, 94]. We discuss this challenge in

Appendix C.2.

The system response (5.33) with the modified spatial regularizer is space and rotation invariant. However, the spatial resolution property will change a lot for the scaling motion. To see this effect clearly, we consider the scaling motion in polar coordinate.

When we assume that

$$(\mathcal{T}_{m,1}f_1)(r,\phi) \approx f_1(r/s_{mj}, \phi) \tag{5.36}$$

where r belongs to a small neighborhood of the jth pixel, $\mathcal{T}_{m,1}$ is a continuous-space analogue of $\boldsymbol{T}_{m,1}$, and $f_1(r, \phi)$ is a continuous-space analogue of $\boldsymbol{f}_1$ in polar coordinate. s_{mj} is a scaling factor at jth voxel, we can express the local frequency response of a continuous-space analogue for (5.35) as follows:

$$\frac{1/|\rho/s_{mj}|}{1/|\rho/s_{mj}| + \eta(2\pi\rho/s_{mj})^2}$$
$$= \frac{1/|\rho|}{1/|\rho| + \eta/|s_{mj}|^3(2\pi\rho)^2}. \tag{5.37}$$

Note that in practice, the measurement matrix $\boldsymbol{A}_m$ may contain a blur function and a scaling factor s_{mj} may alter that function. This may cause (5.37) to be incorrect. In this paper, we neglect blur in the measurement matrix $\boldsymbol{A}_m$ for simplicity.

Therefore, (5.37) suggests that each $\boldsymbol{C}_m$ should include a factor of $|s_{mj}|^3$ to maintain the uniform spatial resolution. When we set

$$\boldsymbol{C}_m \triangleq \boldsymbol{C}_0\boldsymbol{D}([\underline{\kappa}_m]_j|s_{mj}|^{3/2}), \tag{5.38}$$

the system response (5.37) becomes (5.33). Therefore,

$$\mathsf{E}\{\hat{\boldsymbol{f}}_{\mathrm{PMC}}\} \approx [\boldsymbol{F}_0 + \eta\boldsymbol{R}_0]^{-1}\boldsymbol{F}_0\boldsymbol{f}_1 \approx \mathsf{E}\{\hat{\boldsymbol{f}}_1\}. \tag{5.39}$$

This example shows that a simple local scaling motion can alter the spatial resolution because it alters the regularization parameter η by $\eta/|s_{mj}|^3$. Therefore, the spatial resolution in each frame may change after each goes through $\boldsymbol{T}_{1,m}$ operator. Equation (5.38)

suggests that we need an extra term $|s_{mj}|^{3/2}$ to approximately provide uniform spatial resolution for local expanding or shrinking s_{mj}.

5.2.3 Parametric motion model

From (5.8), the expected value of $\hat{\boldsymbol{f}}_{\mathrm{PMM}}$ is given by

$$\mathsf{E}\{\hat{\boldsymbol{f}}_{\mathrm{PMM}}\} = \left[\sum_{m=1}^{M} \breve{\boldsymbol{F}}_m + \eta\boldsymbol{R}_1\right]^{-1} \sum_{m=1}^{M} \breve{\boldsymbol{F}}_m \boldsymbol{f}_1. \qquad (5.40)$$

Since $\boldsymbol{T}'_{m,1} \approx \boldsymbol{T}_{1,m}\boldsymbol{D}(|\nabla\boldsymbol{T}_{m,1}|_j)$ (see Appendix C.1) and $\boldsymbol{D}(|\nabla\boldsymbol{T}_{m,1}|_j) = \boldsymbol{D}(1/|s_{mj}|^2)$ from (5.36), equation (5.40) becomes

$$\mathsf{E}\{\hat{\boldsymbol{f}}_{\mathrm{PMM}}\} = \left[\sum_{m=1}^{M} \boldsymbol{D}(|s_{mj}|^2)\tilde{\boldsymbol{F}}_m + \eta\boldsymbol{R}_1\right]^{-1} \sum_{m=1}^{M} \boldsymbol{D}(|s_{mj}|^2)\tilde{\boldsymbol{F}}_m \boldsymbol{f}_1 \qquad (5.41)$$

where $\tilde{\boldsymbol{F}}_m \triangleq \boldsymbol{T}_{1,m}\boldsymbol{F}_m\boldsymbol{T}_{m,1}$. Thus, the local frequency response of a continuous-space analogue for (5.41) is

$$\frac{\sum_{m=1}^{M} |s_{mj}|^2 \omega_m^j(\Phi)/|\rho/s_{mj}|}{\sum_{m=1}^{M} |s_{mj}|^2 \omega_m^j(\Phi)/|\rho/s_{mj}| + \eta(2\pi\rho)^2}$$
$$= \frac{\sum_{m=1}^{M} |s_{mj}|^3 \omega_m^j(\Phi)/|\rho|}{\sum_{m=1}^{M} |s_{mj}|^3 \omega_m^j(\Phi)/|\rho| + \eta(2\pi\rho)^2}. \qquad (5.42)$$

This suggests that we can achieve uniform spatial resolution by using

$$\boldsymbol{C}_1 \triangleq \boldsymbol{C}_0\mathrm{diag}\{\underline{\nu}\} \qquad (5.43)$$

where

$$[\underline{\nu}]_j \triangleq \sqrt{\sum_{m=1}^{M} |s_{mj}|^3 [\boldsymbol{T}_{1,m}\underline{\kappa}_m]_j^2}. \qquad (5.44)$$

Using (5.43), the local frequency response (5.42) approximates (5.33). In other words, the expected value of $\hat{\boldsymbol{f}}_{\mathrm{PMM}}$ becomes approximately

$$\mathsf{E}\{\hat{\boldsymbol{f}}_{\mathrm{PMM}}\} \approx [\boldsymbol{F}_0 + \eta\boldsymbol{R}_0]^{-1}\boldsymbol{F}_0\boldsymbol{f}_1 \approx \mathsf{E}\{\hat{\boldsymbol{f}}_1\}, \qquad (5.45)$$

which is also the same as $\mathsf{E}\{\hat{\boldsymbol{f}}_{\mathrm{PMC}}\}$.

5.2.4 Motion-compensated temporal regularization

The expected value of the MTR estimator $\hat{\boldsymbol{f}}_{\mathrm{c}}$ in (5.13) is as follows:

$$\mathsf{E}\{\hat{\boldsymbol{f}}_{\mathrm{c}}\} = [\boldsymbol{F}_{\mathrm{MTR}} + \zeta \boldsymbol{R}_{\mathrm{circ}}]^{-1} \boldsymbol{F}_{\mathrm{d}} \boldsymbol{f}_{\mathrm{c}}. \tag{5.46}$$

Since it is not easy to see the spatial resolution property of $\hat{\boldsymbol{f}}_{\mathrm{c}}$ in (5.46), we investigated the spatial resolution properties as $\zeta \to 0$ and $\zeta \to \infty$.

The limiting behavior of $\hat{\boldsymbol{f}}_{\mathrm{c}}$ as $\zeta \to 0$ in (5.14) shows that

$$\mathsf{E}\{\hat{\boldsymbol{f}}_{\mathrm{c}}\} \to \begin{bmatrix} \mathsf{E}\{\hat{\boldsymbol{f}}_1\} \\ \vdots \\ \mathsf{E}\{\hat{\boldsymbol{f}}_M\} \end{bmatrix}. \tag{5.47}$$

This is the same as the expected value of the individually reconstructed image $\hat{\boldsymbol{f}}_m$ from each measurement $\boldsymbol{y}_m$. Therefore, $\mathsf{E}\{\hat{\boldsymbol{f}}_{\mathrm{MTR}}\} \to \mathsf{E}\{\hat{\boldsymbol{f}}_1\}$ as $\zeta \to 0$. In this case, using the regularizer (5.38) for each frame provides approximately uniform spatial resolution effectively for frame 1, *i.e.*, a frame for $\hat{\boldsymbol{f}}_{\mathrm{MTR}}$. Then, what will happen for the spatial resolution as $\zeta \to \infty$?

The limit of the expected value $\mathsf{E}\{\hat{\boldsymbol{f}}_{\mathrm{c}}\}$ is approximately

$$\mathsf{E}\{\hat{\boldsymbol{f}}_{\mathrm{c}}\} \to \boldsymbol{T}_{\mathrm{c}} [\boldsymbol{F}_{\mathrm{c}} + \eta \boldsymbol{R}_{\mathrm{c}}]^{-1} \boldsymbol{F}_{\mathrm{c}} \boldsymbol{f}_1 \tag{5.48}$$

as $\zeta \to \infty$ because of (5.20). So,

$$\mathsf{E}\{\hat{\boldsymbol{f}}_{\mathrm{MTR}}\} \to [\boldsymbol{F}_{\mathrm{c}} + \eta \boldsymbol{R}_{\mathrm{c}}]^{-1} \boldsymbol{F}_{\mathrm{c}} \boldsymbol{f}_1. \tag{5.49}$$

The local frequency response of (5.49) with the regularizer (5.38) is

$$\frac{\sum_{m=1}^{M} \omega_m^j(\Phi)/|\rho/s_{mj}|}{\sum_{m=1}^{M} \omega_m^j(\Phi)/|\rho/s_{mj}| + \eta \omega_m^j(\Phi)|s_{mj}|^3 (2\pi\rho/s_{mj})^2}$$

and it becomes

$$\frac{\sum_{m=1}^{M} |s_{mj}| \omega_m^j(\Phi)/|\rho|}{\sum_{m=1}^{M} |s_{mj}| \omega_m^j(\Phi)/|\rho| + \eta |s_{mj}| \omega_m^j(\Phi)(2\pi\rho)^2} = \frac{1/|\rho|}{1/|\rho| + \eta(2\pi\rho)^2}. \tag{5.50}$$

which is the same as (5.33). Therefore, (5.50) shows that

$$\mathsf{E}\{\hat{\boldsymbol{f}}_{\mathrm{MTR}}\} \rightarrow [\boldsymbol{F}_0 + \eta \boldsymbol{R}_0]^{-1} \boldsymbol{F}_0 \boldsymbol{f}_1 = \mathsf{E}\{\hat{\boldsymbol{f}}_1\} \tag{5.51}$$

as $\zeta \rightarrow \infty$. This is approximately the same local frequency response as the PMC and PMM estimators. However, the mean of other frames in $\hat{\boldsymbol{f}}_{\mathrm{c}}$ may not converge to $\mathsf{E}\{\hat{\boldsymbol{f}}_1\}$. This shows that using $\boldsymbol{R}_1$ in (5.8) has the equivalent effect of using $\boldsymbol{R}_{\mathrm{c}}$ in (5.21).

5.3   Noise properties

Since noise properties of an estimator depend on the spatial resolution properties induced by the regularizer, we focus on the modified regularizers that provide approximately uniform spatial resolution as explained in the previous section. In this section, we assume that $\boldsymbol{W}_m = \mathsf{Cov}\{\boldsymbol{y}_m\}^{-1}$ for all m since it is a usual choice for PWLS reconstruction [22]. We also assume that all measurements $\boldsymbol{y}_m$ for all m are independent, *i.e.*, $\mathsf{Cov}\{\hat{\boldsymbol{f}}_m, \hat{\boldsymbol{f}}_n\} = 0$ for all $m \neq n$. (This does not hold in parallel MRI due to coil couples, but is reasonable in most often tomographic imaging systems.)

5.3.1   Post-reconstruction motion correction

The covariance of the PWLS estimator of a single frame $\hat{\boldsymbol{f}}_m$ is straightforward from (5.2) as follows:

$$\mathsf{Cov}\{\hat{\boldsymbol{f}}_m\} = [\boldsymbol{F}_m + \eta \boldsymbol{R}_m]^{-1} \boldsymbol{F}_m [\boldsymbol{F}_m + \eta \boldsymbol{R}_m]^{-1}. \tag{5.52}$$

When we apply the modified regularizer (5.28) to $\boldsymbol{R}_m$, (5.52) becomes

$$\mathsf{Cov}\{\hat{\boldsymbol{f}}_m\} = \boldsymbol{D}(\underline{\kappa}_m)^{-1} \boldsymbol{\Omega}_0 \boldsymbol{D}(\underline{\kappa}_m)^{-1}, \tag{5.53}$$

where

$$\boldsymbol{\Omega}_0 \triangleq [\boldsymbol{F}_0 + \eta \boldsymbol{R}_0]^{-1} \boldsymbol{F}_0 [\boldsymbol{F}_0 + \eta \boldsymbol{R}_0]^{-1}.$$

By imposing uniform spatial resolution, we have non-uniform noise variance (when $\boldsymbol{W}_m$ is nonuniform) due to $\boldsymbol{D}(\underline{\kappa}_m)^{-1}$. $\boldsymbol{D}(\underline{\kappa}_m)$ depends on the measurement covariance $\mathsf{Cov}\{\boldsymbol{y}_m\}$.

Because we assume that all measurements $\boldsymbol{y}_m$ are independent, the covariance of the PMC estimator (5.4) is

$$
\begin{aligned}
\mathsf{Cov}\{\hat{\boldsymbol{f}}_{\mathrm{PMC}}\} &= \frac{1}{M^2}\sum_{m=1}^{M}\boldsymbol{T}_{1,m}\mathsf{Cov}\{\hat{\boldsymbol{f}}_m\}\boldsymbol{T}_{1,m}{}' \qquad\qquad (5.54)\\
&= \sum_{m=1}^{M}\boldsymbol{D}(|\nabla\boldsymbol{T}_{m,1}|_j^{1/2})\boldsymbol{T}_{1,m}\mathsf{Cov}\{\hat{\boldsymbol{f}}_m\}\boldsymbol{T}_{m,1}\boldsymbol{D}(|\nabla\boldsymbol{T}_{m,1}|_j^{1/2})
\end{aligned}
$$

because of (C.2). In our example, $\boldsymbol{D}(|\nabla\boldsymbol{T}_{m,1}|_j) = \boldsymbol{D}(1/s_{mj}^2)$. When we apply (5.38) to $\boldsymbol{R}_m$, equation (5.54) can be approximated

$$
\mathsf{Cov}\{\hat{\boldsymbol{f}}_{\mathrm{PMC}}\} \approx \frac{1}{M^2}\sum_{m=1}^{M}\boldsymbol{D}([\tilde{\underline{\kappa}}_m^{-1}]_j/s_{mj})\boldsymbol{\Omega}_0\boldsymbol{D}([\tilde{\underline{\kappa}}_m^{-1}]_j/s_{mj}), \qquad\qquad (5.55)
$$

where $\tilde{\underline{\kappa}}_m^{-1} \triangleq \boldsymbol{T}_{1,m}\underline{\kappa}_m^{-1}$.

5.3.2 Parametric motion model

The covariance of the PMM estimator (5.7) is

$$
\mathsf{Cov}\{\hat{\boldsymbol{f}}_{\mathrm{PMM}}\} = [\boldsymbol{F}_{\mathrm{c}} + \eta\boldsymbol{R}_1]^{-1}\boldsymbol{F}_{\mathrm{c}}[\boldsymbol{F}_{\mathrm{c}} + \eta\boldsymbol{R}_1]^{-1}. \qquad\qquad (5.56)
$$

When we apply (5.43) to $\boldsymbol{R}_1$ and re-write $\boldsymbol{F}_{\mathrm{c}} + \eta\boldsymbol{R}_1$, then

$$
\boldsymbol{F}_{\mathrm{c}} + \eta\boldsymbol{R}_1 = \sum_{m=1}^{M}\boldsymbol{D}(s_{mj}^2)\boldsymbol{D}(\boldsymbol{T}_{1,m}\underline{\kappa}_m^2)(\boldsymbol{F}_0 + \eta\boldsymbol{R}_0), \qquad\qquad (5.57)
$$

where $\underline{\kappa}_m^2$ is a vector of the elements $[\underline{\kappa}_m]_j^2$. Therefore, (5.56) becomes

$$
\mathsf{Cov}\{\hat{\boldsymbol{f}}_{\mathrm{PMM}}\} = \boldsymbol{D}(\tilde{\underline{\nu}})^{-1}\boldsymbol{\Omega}_0\boldsymbol{D}(\tilde{\underline{\nu}})^{-1} \qquad\qquad (5.58)
$$

where

$$
[\tilde{\underline{\nu}}]_j \triangleq \sqrt{\sum_{m=1}^{M}s_{mj}^2[\boldsymbol{T}_{1,m}\underline{\kappa}_m]_j^2}.
$$

5.3.3 Motion-compensated temporal regularization

The covariance matrix of the MTR estimator $\hat{\boldsymbol{f}}_{\mathrm{c}}$ is

$$\mathsf{Cov}\{\hat{\boldsymbol{f}}_{\mathrm{c}}\} = \boldsymbol{H}_{\mathrm{MTR}}^{-1}\boldsymbol{F}_{\mathrm{d}}\boldsymbol{H}_{\mathrm{MTR}}^{-1}. \tag{5.59}$$

We study the limits of (5.59) as $\zeta \to 0$ and $\zeta \to \infty$.

For $\zeta \to 0$, since $\boldsymbol{H}_{\mathrm{MTR}} \to \boldsymbol{F}_{\mathrm{MTR}}$ which is block-diagonal, (5.59) goes to

$$\mathsf{Cov}\{\hat{\boldsymbol{f}}_{\mathrm{c}}\} \to \begin{bmatrix} \mathsf{Cov}\{\hat{\boldsymbol{f}}_1\} & & \\ & \ddots & \\ & & \mathsf{Cov}\{\hat{\boldsymbol{f}}_M\} \end{bmatrix}. \tag{5.60}$$

Thus, $\mathsf{Cov}\{\hat{\boldsymbol{f}}_{\mathrm{MTR}}\} \to \mathsf{Cov}\{\hat{\boldsymbol{f}}_1\}$ as $\zeta \to 0$.

For $\zeta \to \infty$, (5.59) becomes

$$\mathsf{Cov}\{\hat{\boldsymbol{f}}_{\mathrm{c}}\} \to \boldsymbol{T}_{\mathrm{c}}[\boldsymbol{F}_{\mathrm{c}} + \eta\boldsymbol{R}_{\mathrm{c}}]^{-1}\boldsymbol{F}_{\mathrm{c}}[\boldsymbol{F}_{\mathrm{c}} + \eta\boldsymbol{R}_{\mathrm{c}}]^{-1}\boldsymbol{T}_{\mathrm{c}}', \tag{5.61}$$

i.e., the covariance of $\hat{\boldsymbol{f}}_{\mathrm{MTR}}$ goes to

$$\mathsf{Cov}\{\hat{\boldsymbol{f}}_{\mathrm{MTR}}\} \to [\boldsymbol{F}_{\mathrm{c}} + \eta\boldsymbol{R}_{\mathrm{c}}]^{-1}\boldsymbol{F}_{\mathrm{c}}[\boldsymbol{F}_{\mathrm{c}} + \eta\boldsymbol{R}_{\mathrm{c}}]^{-1}. \tag{5.62}$$

Assuming that each $\boldsymbol{R}_m$ uses (5.38), it is easy to show that

$$\mathsf{Cov}\{\hat{\boldsymbol{f}}_{\mathrm{MTR}}\} \to \mathsf{Cov}\{\hat{\boldsymbol{f}}_{\mathrm{PMM}}\}$$

since $\boldsymbol{R}_{\mathrm{c}}$ in (5.62) is equivalent to $\boldsymbol{R}_1$ in (5.56) when (5.38) is applied to $\boldsymbol{R}_{\mathrm{c}}$.

5.3.4 Comparison of noise properties in MCIR methods

The covariance of PMM (5.58) is the same as the covariance of MTR for $\zeta \to \infty$, as expected because $\hat{\boldsymbol{f}}_{\mathrm{MTR}} \to \hat{\boldsymbol{f}}_{\mathrm{PMM}}$ as $\zeta \to \infty$. However, the covariance of PMC (5.55) has a different form. These two forms lead to two main differences in terms of noise performance.

First, the covariance of PMM (5.58) is smaller than the covariance of PMC (5.55) when there are frames with significantly different noise levels. To illustrate this point, without the loss of generality, consider the effects of various values of $\underline{\kappa}_1$.

As $\underline{\kappa}_1 \to \infty$, frame 1 has significantly better SNR than other frames and it is desirable to emphasize the information from frame 1. However, in this case, the covariance of PMC (5.55) shows that

$$\mathsf{Cov}\{\hat{\boldsymbol{f}}_{\mathrm{PMC}}\} \to \frac{1}{M^2} \sum_{m=2}^{M} \boldsymbol{D}\left(\frac{1}{s_{mj}[\tilde{\underline{\kappa}}_m]_j}\right) \boldsymbol{\Omega}_0 \boldsymbol{D}\left(\frac{1}{s_{mj}[\tilde{\underline{\kappa}}_m]_j}\right)$$

as $\underline{\kappa}_1 \to \infty$. Therefore, $\mathsf{Cov}\{\hat{\boldsymbol{f}}_{\mathrm{PMC}}\}$ may not have zero covariance. However, since $\tilde{\nu} \to \infty$ as $\underline{\kappa}_1 \to \infty$, the covariance of PMM (5.58) becomes

$$\mathsf{Cov}\{\hat{\boldsymbol{f}}_{\mathrm{PMM}}\} \to \boldsymbol{0}.$$

This shows that $\hat{\boldsymbol{f}}_{\mathrm{PMM}}$ automatically emphasizes the information from the most informative frames. $\hat{\boldsymbol{f}}_{\mathrm{MTR}}$ has the same property for $\zeta \to \infty$.

As $\underline{\kappa}_1 \to 0$, the information from frame 1 is contaminated by extreme noise. In this case, (5.55) shows that

$$\mathsf{Cov}\{\hat{\boldsymbol{f}}_{\mathrm{PMC}}\} \to \infty.$$

A simple average is not effective at rejecting outliers. In contrast, as $\underline{\kappa}_1 \to 0$,

$$[\tilde{\underline{\nu}}]_j \to \sqrt{\sum_{m=2}^{M} s_{mj}^2 [\boldsymbol{T}_{1,m}\underline{\kappa}_m]_j^2} = \sqrt{\sum_{m=2}^{M} s_{mj}^2 [\tilde{\underline{\kappa}}_m]_j^2}$$

and the covariance of PMM still has a finite value. This shows that $\hat{\boldsymbol{f}}_{\mathrm{PMM}}$ is less easily contaminated by frames with poor statistics. $\mathsf{Cov}\{\hat{\boldsymbol{f}}_{\mathrm{MTR}}\}$ also has the same property for large ζ value.

Secondly, the variance of PMM is lower than the variance of PMC. Both PMM and PMC covariances consist of $\boldsymbol{\Omega}_0$ matrix and diagonal matrices. We compare the variances of PMM and PMC by comparing such diagonal elements. When we have $b_m \triangleq$

$s_{mj}^2[\boldsymbol{T}_{1,m}\boldsymbol{\kappa}_m]_j^2$, the jth diagonal element of the PMM covariance is

$$\frac{1}{\sum_{m=1}^{M} b_m}[\boldsymbol{\Omega}_0]_{jj},$$

and the jth diagonal element of the PMC covariance is

$$\frac{1}{M^2}\sum_{m=1}^{M}\frac{1}{b_m}[\boldsymbol{\Omega}_0]_{jj}.$$

By Cauchy-Schwartz inequality,

$$M^2 = \left(\sum_{m=1}^{M}\sqrt{b_m}/\sqrt{b_m}\right)^2 \leq \sum_{m=1}^{M} b_m \sum_{m=1}^{M} 1/b_m,$$

which shows that

$$\mathsf{Var}\{\hat{\boldsymbol{f}}_{\mathrm{PMM}}\} \leq \mathsf{Var}\{\hat{\boldsymbol{f}}_{\mathrm{PMC}}\}. \tag{5.63}$$

Asma *et al.* [5] also showed (5.63), but only for the unregularized case. Since we have spatial regularization designed to approximately provide uniform spatial resolution, we can show (5.63) even for regularized case. PMC also can achieve the same level of noise performance since PMM is a weighted version of PMC as we showed in (5.24). For MTR estimator, the variance of it becomes $\mathsf{Var}\{\hat{\boldsymbol{f}}_{\mathrm{MTR}}\} \rightarrow \mathsf{Var}\{\hat{\boldsymbol{f}}_{\mathrm{PMM}}\}$ as $\zeta \rightarrow \infty$.

5.4 Simulation results

5.4.1 Simulation setting

Figure 5.1 shows four image frames of a 2D object with known motion (scaling, rotating and translating). The original image has 160×160 samples with 3.4mm pixel width. We forward-projected these original images using the CTI 931 PET scanner geometry / detector response with 160 detector samples, 3.375 mm spacing, 192 angular views, and 3.375 mm strip width. We used 250K mean true coincidences for each frame (1M total) with 10% random coincidences. We ignored attenuation in this simulation to see the effect of the theory clearly because attenuation depends on object size.
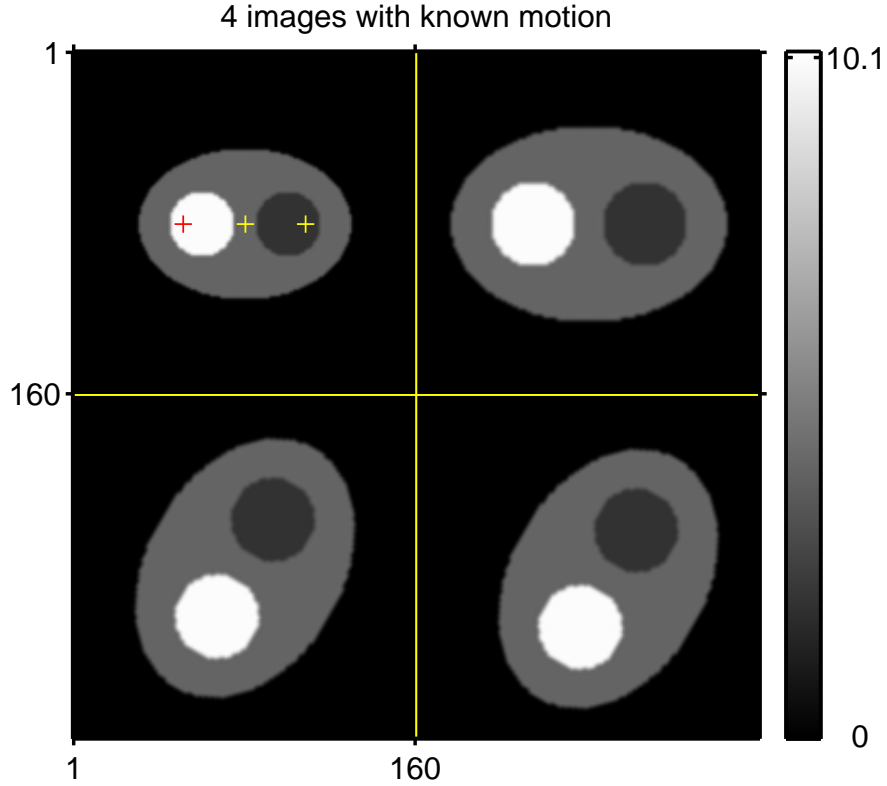
Figure 5.1: Four true image frames $\boldsymbol{f}_1, \ldots, \boldsymbol{f}_4$ with scaling, rotation and translation. Three impulses are placed at $+$ marks.

5.4.2 Spatial resolution matching

We computed the local impulse response (LIR) of each method by reconstructing images from noiseless projection data as suggested in [24]. We located three impulses at frame 1 ($+$ marks in figure 5.1) and warped the original image into each frame. Our target full width of half maximum (FWHM) was 1.9 pixels.

Figure 5.2 (a) shows the LIR of PWLS 1 (circle) from a single frame (separate) image reconstruction with a conventional κ in (5.28) at the hot region. This is our target LIR for all three MCIR methods. Figure 5.2 also shows the LIR of PMCo, *i.e.*, PMM with a conventional κ in (5.28). It shows that a conventional κ may cause spatial resolution mismatch due to scaling motion. However, LIR of the PMC with our modified κ in (5.38)

(a) LIRs of PMC

(b) LIRs of PMM
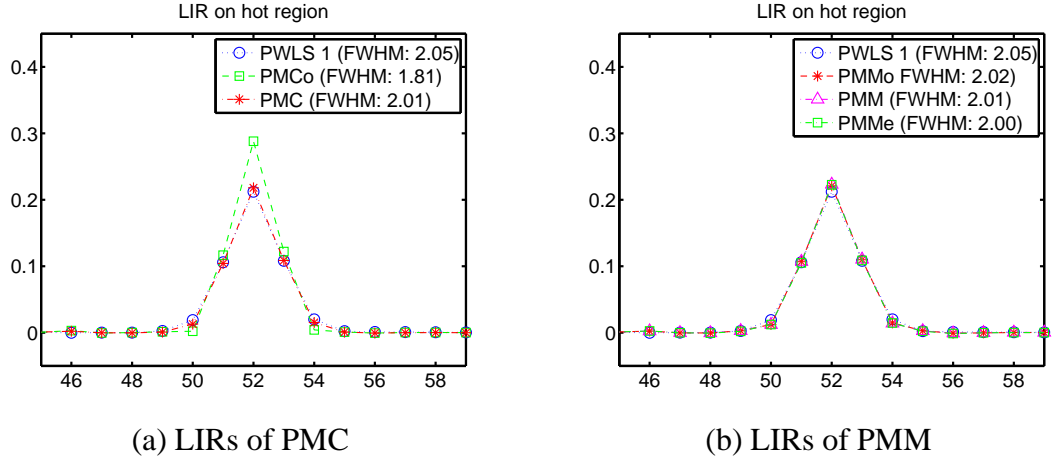
Figure 5.2: Profiles of LIRs at hot region. For (a), PWLS 1 is from a single frame and it is the target LIR. PMCo uses a conventional static κ. PMC uses a proposed regularizer. For (b), PMMo uses a conventional κ of frame 1 multiplied by the number of frames. PMM uses a proposed ν. PMMe uses an equivalent regularizer $\boldsymbol{R}_{\mathrm{c}}$ from MTR.

can compensate for the spatial resolution mismatch. LIRs at other areas show almost identical results.

Figure 5.2 (b) shows LIRs of PMM with three different regularizers. All regularizers show close matching with PWLS 1 within 0.1 pixel error. PMMo performs very well compared to other proposed regularizers. It seems that the scaling factor compensates for the effect of κs from other frames in (5.43), but PMMo only used a conventional κ of frame 1 multiplied by 4. However, with noise, PMMo may perform poorly since it estimates κ from one frame, not from all frames as seen in (5.43).

Lastly, figure 5.3 (a) and (b) shows LIRs of MTR with different values of ζ. MTRo with a conventional κ in (5.28) shows that there would be resolution mismatch due to scaling as ζ increases. However, MTR with the proposed regularizer in (5.38) shows that LIRs are matching well within 0.1 pixel error for different ζ values. It seems that $\zeta = 1$ is large enough to see the effect of $\zeta \to \infty$. We can also notice that PMMe in figure 5.2 (b) and MTR with $\zeta = 1$ have the same FWHM (1.84 pixels). This result explains (5.21) well.

(a) MTR with (5.28)　　　　　(b) MTR with (5.38)
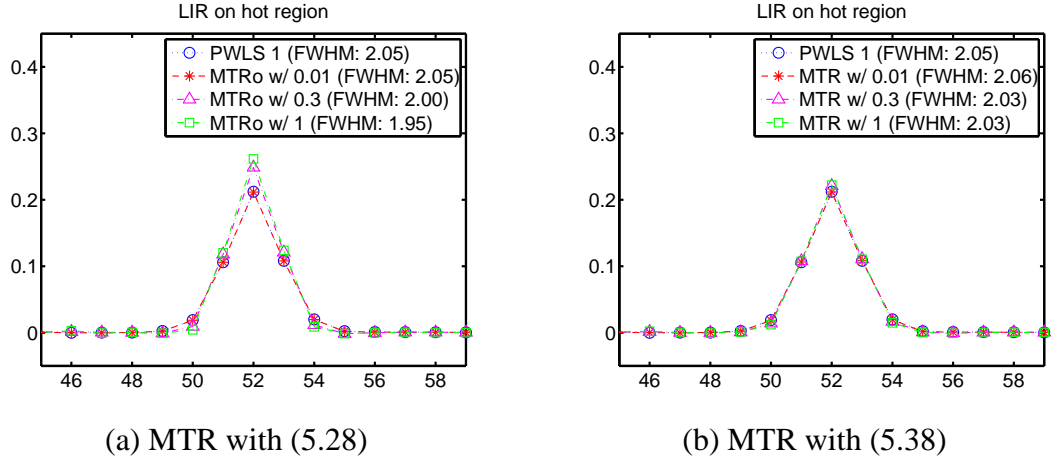
Figure 5.3: Profiles of LIRs at hot region. MTRo is with a conventional κ. MTR is with the proposed regularizer (5.38).

5.4.3 Reconstructed images and variances

Figure 5.4 (a) shows an image that is reconstructed by (5.1) from a single realization. Since the measurement of one frame has a low photon count (250K), it has a poor quality. Figure 5.4 (b) shows the result when we use all photon counts (1M), but without motion correction. Motion artifacts are observed in the result. Figures 5.4 (c) and (d) show reconstructed images of PMC and PMM. Compared to (a) and (b), both (c) and (d) show improved image quality in terms of noise and reduction of motion artifacts.

Figures 5.5 (a), (b) and (c) show reconstructed images of MTR with different ζ values (0.01, 0.3, 1). (a) looks similar to figure 5.4 (a), but a little better because ζ is not completely 0. As ζ increses, reconstructed images is getting closer to the result of PMM in figure 5.4 (c). Figure 5.5 (d) shows a reconstructed image of PMM with $\boldsymbol{R}_{c}$. This looks very close to reconstructed images of PMM with $\boldsymbol{R}_1$ and MTR for large ζ. In practice, ζ does not have to be ∞, but $\zeta = 1$ is large enough relative to other terms in (5.11).

Lastly, figure 5.6 shows that the standard deviation of MCIR methods are lower than the standard deviation of PWLS single frame reconstruction.
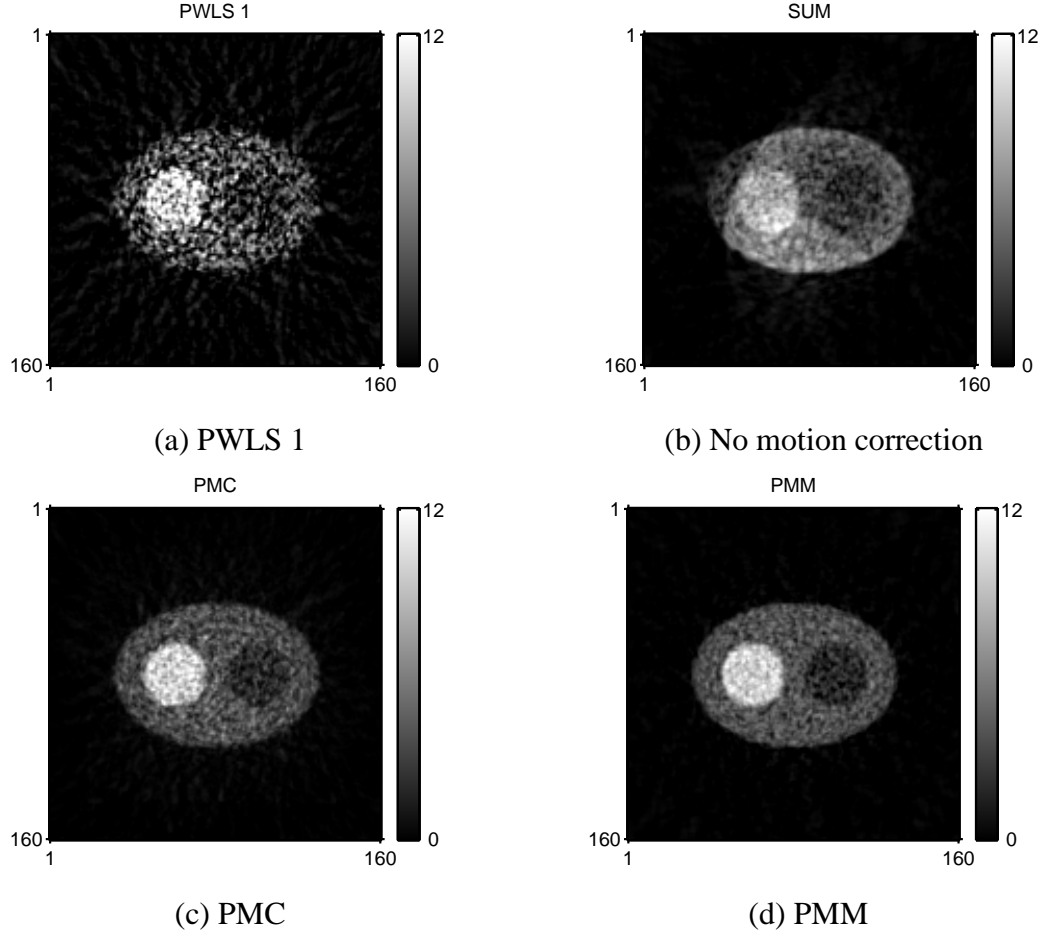
Figure 5.4: Reconstructed images from a single realization. (a) is a PWLS reconstructed image from frame 1. (b) is a reconstructed image from all frames without motion correction. (c) is a PMC reconstructed image. (d) is a PMM reconstructed image.

5.5 Discussion

We investigated three different MCIR methods and their spatial resolution and noise properties. Analyses show that MTR is equivalent to PMM as $\zeta \to \infty$ with given motion and is also equivalent to PWLS 1 as $\zeta \to 0$.

When we use MTR with given periodic motions, it is important to make sure that warps are transitive. Otherwise, we may have an additional condition for null space of R_{circ}, $f_1 = T_{1,M} f_M$, which may not depend on (5.15).

This analysis can help to understand the joint estimation problem of image and motion

(a) MTR with $\zeta = 0.01$ 　　　　　　　(b) MTR with $\zeta = 0.3$

(c) MTR with $\zeta = 1$ 　　　　　　　(d) PMM with $\boldsymbol{R}_{\mathrm{c}}$
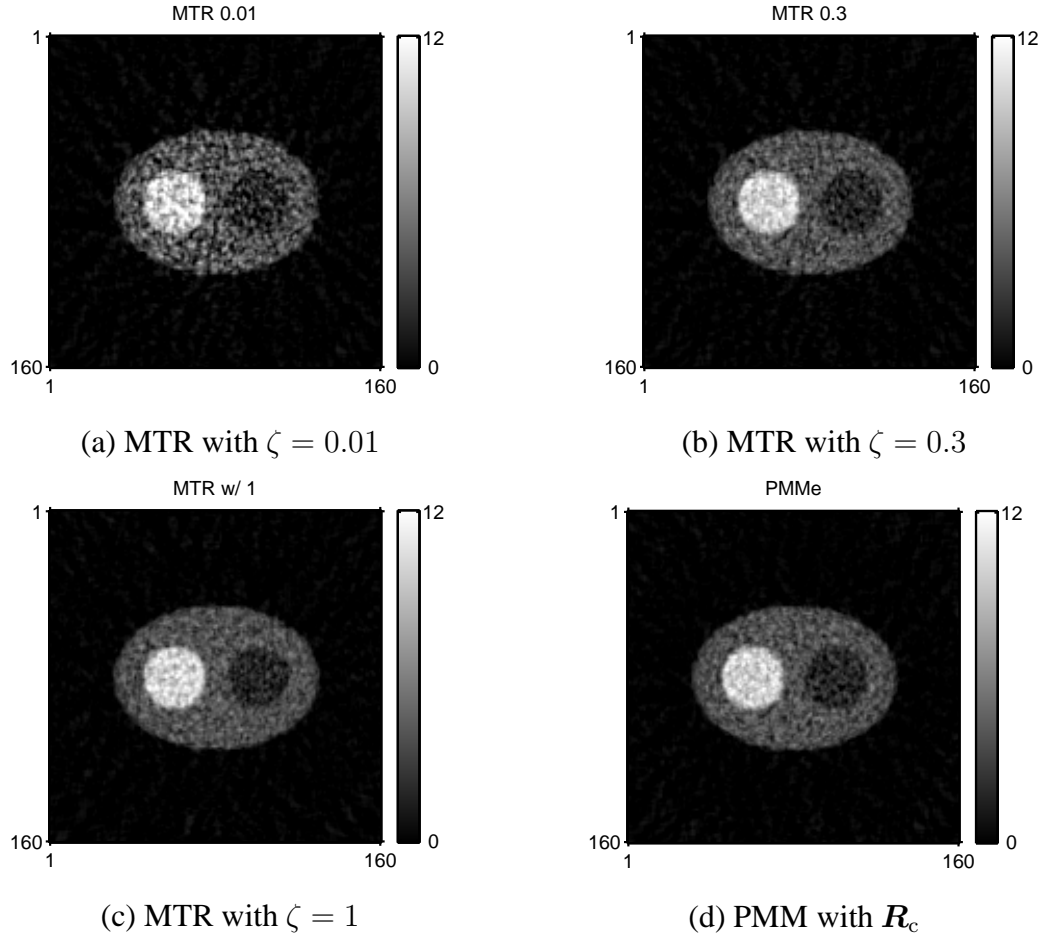
Figure 5.5: MTR reconstructed images from a single realization with different ζ. As ζ increases, it approached to a PMM reconstructed image with a regularizer $\boldsymbol{R}_{\mathrm{c}}$.

in each MCIR model. For example, since the Jacobian determinant values of estimated deformations may change the spatial resolution properties, it is very important to have a good motion prior in the joint estimation with MCIR methods.

We also showed that PMM and MTR (for large ζ) are equivalent to PMC with special weights for sum. It is important to be rigorous in terms of statistical principle when we model the reality to achieve better statistical properties. PMC can be a natural choice when we have multiple reconstructed images, but PMM and MTR with large ζ shows that PMC needs specific weights to achieve better noise property with the same resolution.

Lastly, spatial resolution analysis for MCIR methods is very challenging in practice.
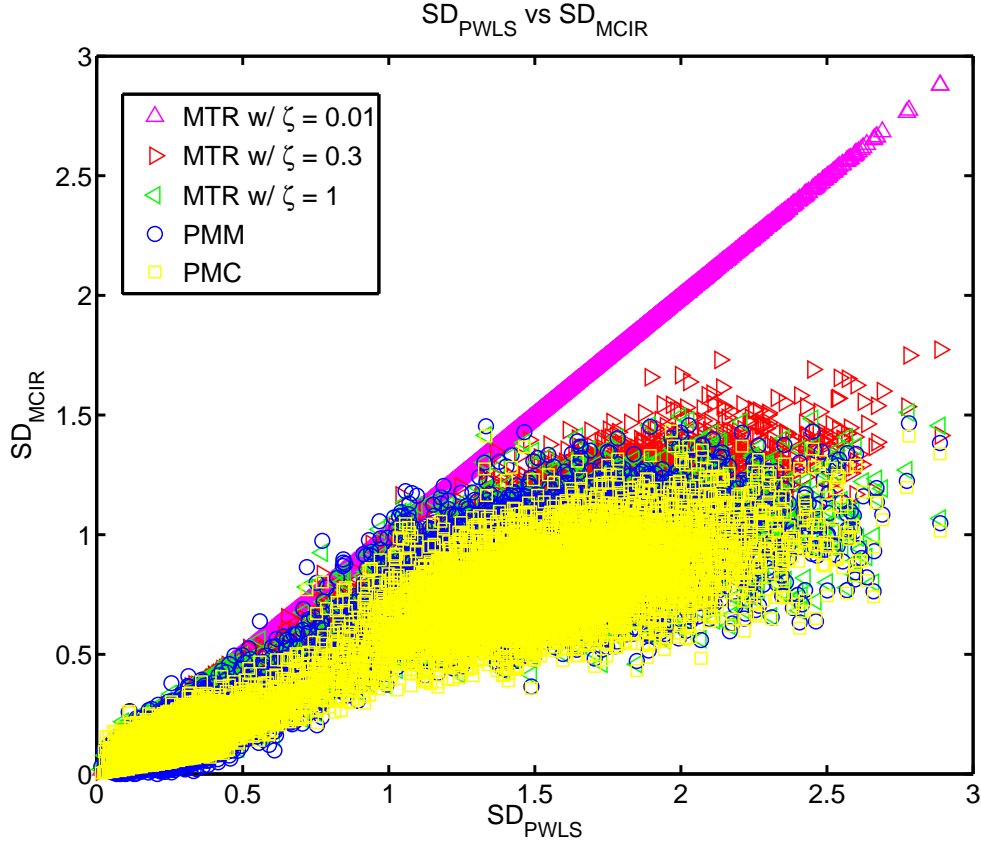
Figure 5.6: Standard deviation (SD) of PWLS vs. SD of MCIR methods. All MCIR methods reduce SD compared to PWLS from a single frame.

There are many factors to consider, such as different measurement matrices A_m, blurring kernel in each A_m, different detector response for different size of objects and so on. It is also very challenging to deal with different motions, such as scaling with different rate in each direction or shear motion. However, maintaining similar levels of spatial resolution for each frame, such as (5.38), and then applying post filtering would be reasonable to use in practice.

There can be many future directions for research in this area. Designing a spatial regularizer for uniform spatial resolution with shear motion and with different regularizers other than quadratic penalty will be a challenging task. Extending this analysis with unknown motion will be another interesting future work.

CHAPTER 6

Joint image reconstruction and nonrigid motion estimation with motion invertibility regularizer [4]

Medical imaging modalities such as PET, SPECT, CT and MRI provide useful patient image information for diagnosis, treatment planning, and intervention in clinical settings. However, due to the innate limitation of medical imaging modalities in terms of acquisition time and patient motion, there are some trade-offs between spatial resolution and motion artifacts. Gating methods based on breathing signals or ECG signals [63] can reduce motion artifacts significantly, but can also reduce SNR by discarding potentially useful data.

MCIR methods have been investigated to exploit all collected data and motion information to improve the quality of reconstructed images with a better SNR and less motion artifacts. Most of the methods incorporate nonrigid motion into their image reconstruction models since human organ motion is nonrigid [50]. Motion can be given from other sources [30, 44, 52, 53, 75] or be estimated from the collected data [35, 57, 99].

MCIR methods with given nonrigid motion are very useful and have been researched frequently. Many multi-modal imaging systems such as PET/CT and PET/MR provide low resolution functional imaging and high resolution structural imaging. MCIR methods can

---

[4]This chapter is based on [14].

95

be used to improve the quality of low resolution imaging and motion can be estimated from high resolution imaging such as CT or MR. Based on this situation, many researchers have investigated MCIR methods with given motion mainly for PET/CT [52, 53, 75]. However, since PET/CT does not acquire PET and CT measurements simultaneously, there can be discrepancies between PET and CT motion [21, 59].

Joint MCIR methods have broad potential applications. Two of the three MCIR methods described in Chapter 5, namely PMM and MTR, have been investigated previously for joint reconstruction/registration problems. Joint PMM has been investigated for PET [34–37], CT [97–99], and MRI [69, 70]. Joint MTR has been also studied for SPECT perfusion imaging [29–31] and emission computed tomography (ECT) [9, 27, 57]. However, there has been little research on the performance analysis for joint MCIR methods. In SR research, there are some efforts to seek the fundamental limits of PMM [7, 54, 101]. Robinson *et al.* used the Cramer-Rao (CR) bound to analyze the performance of joint PMM, but it was limited to global translation motion [78, 79]. Ruan also used the CR bound for the performance analysis of global translation motion estimation and treated images as nuisance parameters [82].

It may be beneficial to explore the estimates of joint MCIR methods with different spatial and motion regularization parameters. Better understanding of the joint MCIR models may be helpful to attack the performance analysis of joint MCIR methods. This chapter provides some preliminary results for different joint MCIR methods with various spatial and motion regularization parameter values. It also investigates the joint MCIR methods with different motion regularizers: a proposed motion invertibility regularizer in Chapter 3 and a conventional quadratic motion regularizer [14]. These preliminary results help reveal how different motion regularizers can affect image estimates. We simulated 4D gated PET imaging with the 4D XCAT phantom [88]. The XCAT phantom provides a

tool to add lesions and we placed 4 lesions in different areas.

6.1 Motion treatment in model-based image reconstruction

In this section, we briefly review different strategies for incorporating motion in model-based image reconstruction. We also review different MCIR models with unknown motion and add motion regularizers to MCIR models.

6.1.1 Ungated image reconstruction

One possible approach to motion in model-based image reconstruction is to ignore it altogether. In this case, the measurement model is as follows:

$$\boldsymbol{y}_{\mathrm{c}} = \boldsymbol{A}_{\mathrm{c}}\boldsymbol{f}_1 + \boldsymbol{\epsilon}_{\mathrm{c}}$$

where $\boldsymbol{A}_{\mathrm{c}} \triangleq [\boldsymbol{A}_1' \ldots \boldsymbol{A}_M']'$. Then, the PWLS estimator for $\boldsymbol{f}_1$ is

$$\hat{\boldsymbol{f}}_{\mathrm{SUM}} = \operatorname*{argmin}_{\boldsymbol{f}_1} \|\boldsymbol{y}_{\mathrm{c}} - \boldsymbol{A}_{\mathrm{c}}\boldsymbol{f}_1\|_{\boldsymbol{W}_{\mathrm{d}}}^2 + \eta_R\|\boldsymbol{C}_1\boldsymbol{f}_1\|_2^2. \tag{6.1}$$

Note that there is no motion estimation in this case.

6.1.2 Separate frame-by-frame image reconstruction

As the opposite extreme from section 6.1.1, one can reconstruct an image from each frame that is motion-free:

$$\hat{\boldsymbol{f}}_m = \operatorname*{argmin}_{\boldsymbol{f}_m} \|\boldsymbol{y}_m - \boldsymbol{A}_m\boldsymbol{f}_m\|_{\boldsymbol{W}_m}^2 + \eta_R\|\boldsymbol{C}_m\boldsymbol{f}_m\|_2^2, \quad m = 1, \cdots, M. \tag{6.2}$$

The measurement $\boldsymbol{y}_m$ can be collected over a short period of time or can be collected during the same phase of periodic motion such as cardiac and respiratory motion [62, 77, 109]. The estimates $\hat{\boldsymbol{f}}_m$ will have lower SNR than $\hat{\boldsymbol{f}}_{\mathrm{SUM}}$ because $\hat{\boldsymbol{f}}_m$ uses less data.

6.1.3 Post-reconstruction motion correction

The estimate (6.1) contains motion artifacts whereas (6.2) has poor SNR due to insufficient measurements. Using motion information in model-based image reconstruction may improve the reconstructed image quality in terms of SNR and motion artifacts. Post-reconstruction motion correction (PMC) is a straightforward method that implements this idea.

We denote a warp from $\boldsymbol{f}_n$ to $\boldsymbol{f}_m$ as $\boldsymbol{T}_{m,n}$ and assume that $\boldsymbol{T}_{m,n}$ is parametrized by $\underline{\alpha}_{m,n}$ in (2.6). Then, the warp can be represented as

$$\boldsymbol{T}_{m,n} = \breve{\boldsymbol{T}}(\underline{\alpha}_{m,n})\breve{\boldsymbol{T}}_0^{-1},$$

where $\breve{\boldsymbol{T}}_0 \triangleq \breve{\boldsymbol{T}}(\boldsymbol{0})$. The PMC method estimates the motion parameter vector $\underline{\alpha}_{1,m}$ from the reconstructed images:

$$\hat{\underline{\alpha}}_{1,m} = \underset{\underline{\alpha}_{1,m}}{\operatorname{argmin}} \, \boldsymbol{d}(\boldsymbol{f}_1, \breve{\boldsymbol{T}}(\underline{\alpha}_{1,m})\breve{\boldsymbol{T}}_0^{-1}\boldsymbol{f}_m) + \eta_M \mathcal{R}_M(\underline{\alpha}_{1,m}), \quad m = 2, \cdots, M$$

where $\boldsymbol{d}(\cdot, \cdot)$ is any metric to measure the distance between one image from the other. We used the sum of squared difference (L_2 norm), but other metrics such as correlation coefficient [41] or mutual information [72, 110] can also be used. $\mathcal{R}_M(\cdot)$ can be an elastic motion regularizer or one of the regularizers we proposed in chapter 3 and 4.

Then, the PMC estimator is the average of motion-corrected estimators for individual frames:

$$\hat{\boldsymbol{f}}_{\mathrm{PMC}} = \frac{1}{M} \left(\hat{\boldsymbol{f}}_1 + \sum_{m=2}^{M} \breve{\boldsymbol{T}}(\hat{\underline{\alpha}}_{1,m})\breve{\boldsymbol{T}}_0^{-1}\hat{\boldsymbol{f}}_m \right). \tag{6.3}$$

Unfortunately, the motion estimates $\hat{\underline{\alpha}}_1, \ldots, \hat{\underline{\alpha}}_M$ are based on image estimates $\hat{\boldsymbol{f}}_1, \ldots, \hat{\boldsymbol{f}}_M$ that may have poor image quality due to insufficient measurements.

6.1.4 Motion-compensated temporal regularization

By adding a motion regularizer to the cost function of MTR in (5.11), we have a joint MTR estimate for image and motion as follows:

$$(\hat{\boldsymbol{f}}_1, \cdots, \hat{\boldsymbol{f}}_M, \underline{\hat{\alpha}}_{2,1}, \cdots, \underline{\hat{\alpha}}_{M,M-1}) = \underset{\boldsymbol{f}_1, \cdots, \boldsymbol{f}_M, \underline{\alpha}_{2,1}, \cdots, \underline{\alpha}_{M,M-1}}{\text{argmin}} \sum_{m=1}^{M} \|\boldsymbol{y}_m - \boldsymbol{A}_m \boldsymbol{f}_m\|_{\boldsymbol{W}_m}^2$$

$$+ \eta_R \|\boldsymbol{C}_m \boldsymbol{f}_m\|_2^2 + \zeta \sum_{m=1}^{M-1} \|\boldsymbol{f}_{m+1} - \breve{\boldsymbol{T}}(\underline{\alpha}_{m+1,m}) \breve{\boldsymbol{T}}_0^{-1} \boldsymbol{f}_m\|_2^2 + \eta_M \mathcal{R}_M(\underline{\alpha}_{m+1,m}).$$

For periodic motion, we can modify the temporal regularization term by adding $\|\boldsymbol{f}_1 - \breve{\boldsymbol{T}}(\underline{\alpha}_{1,M}) \breve{\boldsymbol{T}}_0^{-1} \boldsymbol{f}_M\|_2^2$.

This cost function combines image reconstruction cost functions and image registration cost functions with a weight ζ. We usually optimize this cost function by the alternating optimization scheme in section 2.2.1 for images and motion. Motion estimates affect the quality of image reconstruction via the motion-compensated temporal regularization term, which may improve the quality of reconstructed images as discussed in chapter 5. Image estimates also affect motion estimation performance, so joint MTR improves the estimates of image and motion in a joint fashion.

6.1.5 Parametric motion model

Joint PMM is simply the combination of the PMM approach in (5.7) and a motion regularizer as follows:

$$(\hat{\boldsymbol{f}}_1, \underline{\hat{\alpha}}_{2,1}, \cdots, \underline{\hat{\alpha}}_{M,1}) = \underset{\boldsymbol{f}_1, \underline{\alpha}_{2,1}, \cdots, \underline{\alpha}_{M,1}}{\text{argmin}} \sum_{m=1}^{M} \|\boldsymbol{y}_m - \boldsymbol{A}_m \breve{\boldsymbol{T}}(\underline{\alpha}_{m,1}) \breve{\boldsymbol{T}}_0^{-1} \boldsymbol{f}_1\|_{\boldsymbol{W}_m}^2$$

$$+ \eta \|\boldsymbol{C}_1 \boldsymbol{f}_1\|_2^2 + \eta_M \sum_{m=2}^{M} \mathcal{R}_M(\underline{\alpha}_{m,1}).$$

Unlike other MCIR methods in this thesis, the joint PMM performs nonrigid image registration using raw data, *i.e.*, sinogram data in tomography. PMM uses a weighted least square metric that measures the difference between measurements and the projection

of warped images. A negative log likelihood can be used when joint PMM uses maximum likelihood estimation instead of PWLS. Joint PMM uses the alternating optimization scheme in section 2.2.1 and aims to improve the quality of both image and motion estimates in a joint fashion.

6.2 Simulation results

We simulated 4D gated PET imaging with the 4D XCAT phantom [88]. The spatial sampling of images was $160 \times 160 \times 48$ with $3.3 \times 3.3 \times 3.4 \ mm^3$ voxel size. Original images covered diaphragm and lung area. We generated $M = 8$ images at equally-divided respiratory phases during a 5 second breathing period. We assumed that there is no heart motion to focus on respiratory motion correction. Figure 6.1 shows sagittal and coronal views of exhale and inhale states for the XCAT phantom.
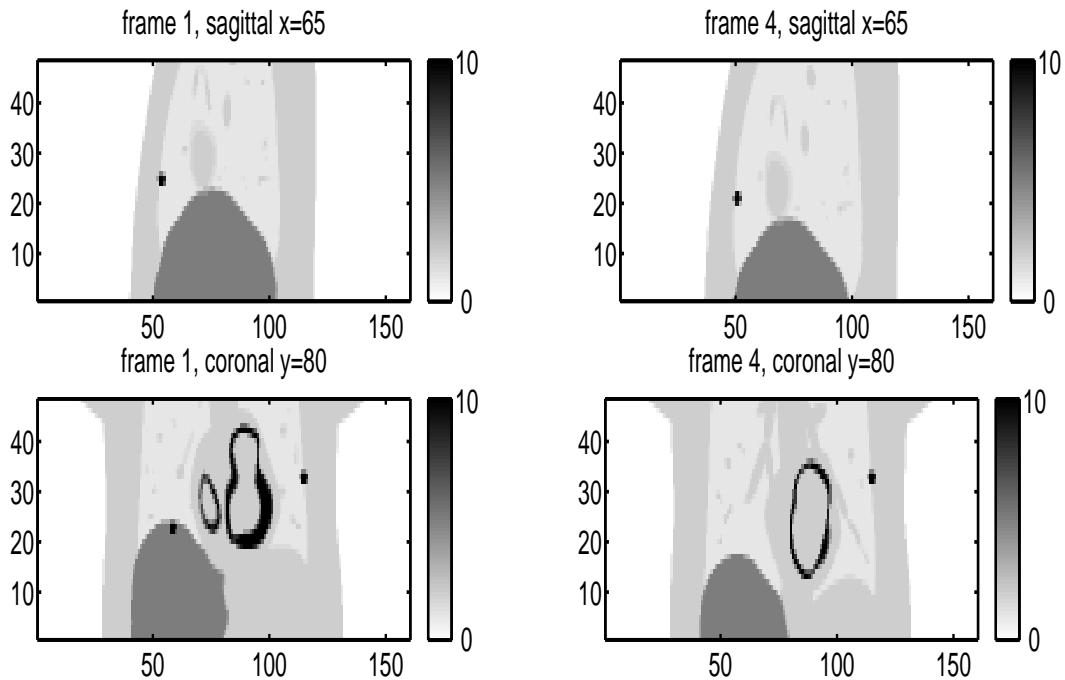
Figure 6.1: Sagittal (TOP) and coronal (BOTTOM) views of XCAT phantom, frame 1 (exhale, LEFT) and frame 4 (inhale, RIGHT)

We placed lesions at 4 different areas (2 in right lung, 1 in left lung, and 1 in liver)

at frame 1. Each spherical lesion had a 10 mm diameter. These lesions were moved and stored by the XCAT phantom toolkit [88]. Figure 6.2 shows 4 different slices where lesions are located at frame 1 (exhale status) and frame 4 (inhale status). Depending on the location of the lesions, they may appear in different slices because there is large superior-inferior motion by diaphragm. We chose 4 rectangular areas to contain all lesions as regions of interest (ROI). Our ROIs contain a total of 100 voxels out of the image's 1,228,800 voxels in different frames, which is only 0.0081% of the total volume.

Generated gated images were projected using CTI 931 PET scanner geometry with 160 detector samples, 3.375 mm distance between detector cells, 192 angle views, 3.375 mm strip width, and 10% random coincidences. We assumed that the sinogram of each gated image has 125,000 (125K) mean true coincidences and all collected sinograms contain 1 million (1M) counts total. We ignored the attenuation in this simulation. The conjugate gradient (CG) algorithm was used for image reconstruction optimization with 100 iterations. FBP reconstructed images were used as initial images. CG was also used for nonrigid motion estimation with 2-level multiresolution and 100, 200 iterations at each level.

A quadratic spatial regularizer was used to reduce the high noise of PET imaging. As we increase the spatial regularization parameter η_R, we can reduce the noise in reconstructed images, but we also lose details in them. Figure 6.3 illustrates that we need to choose η_R carefully to reduce the noise and to preserve fine details such as lesions. Figure 6.4 shows quantitative results for different spatial regularization parameter values. As we increase the spatial regularization parameter η_R, the norm of the difference between the true image and reconstructed images decreases. However, as we can observe in PWLS1M, a too strong regularization parameter may blur the fine structure of images and increase the norm of the difference. We can observe more dramatic results in the ROI
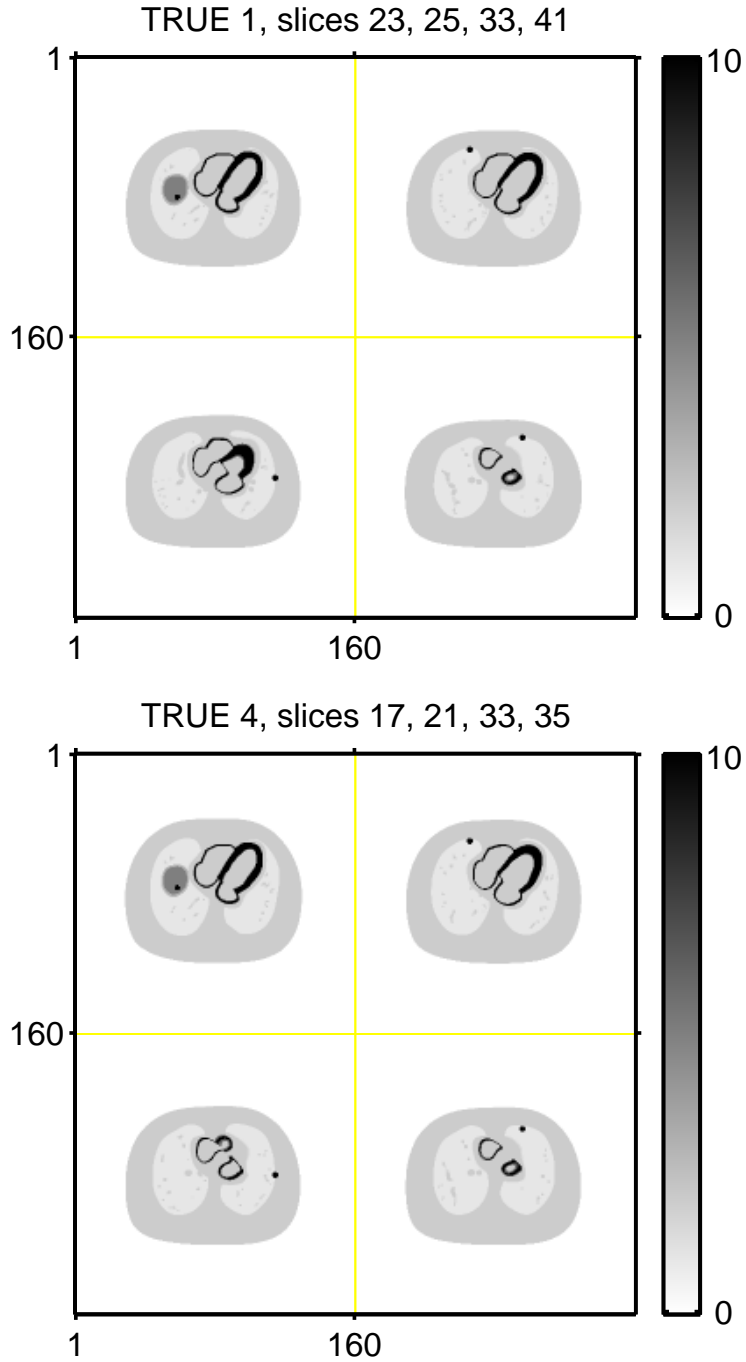
Figure 6.2: Axial views of frame 1 (exhale) and frame 4 (inhale) for 4 lesions.

since it contains the large portion of fine details, *i.e.*, lesions. Note that ROI only occupies

less than 0.01% of total volume, but contributes 5.05% to 24.67% of the total difference

norm. It seems that PWLS125K still benefits from using strong regularization parameters
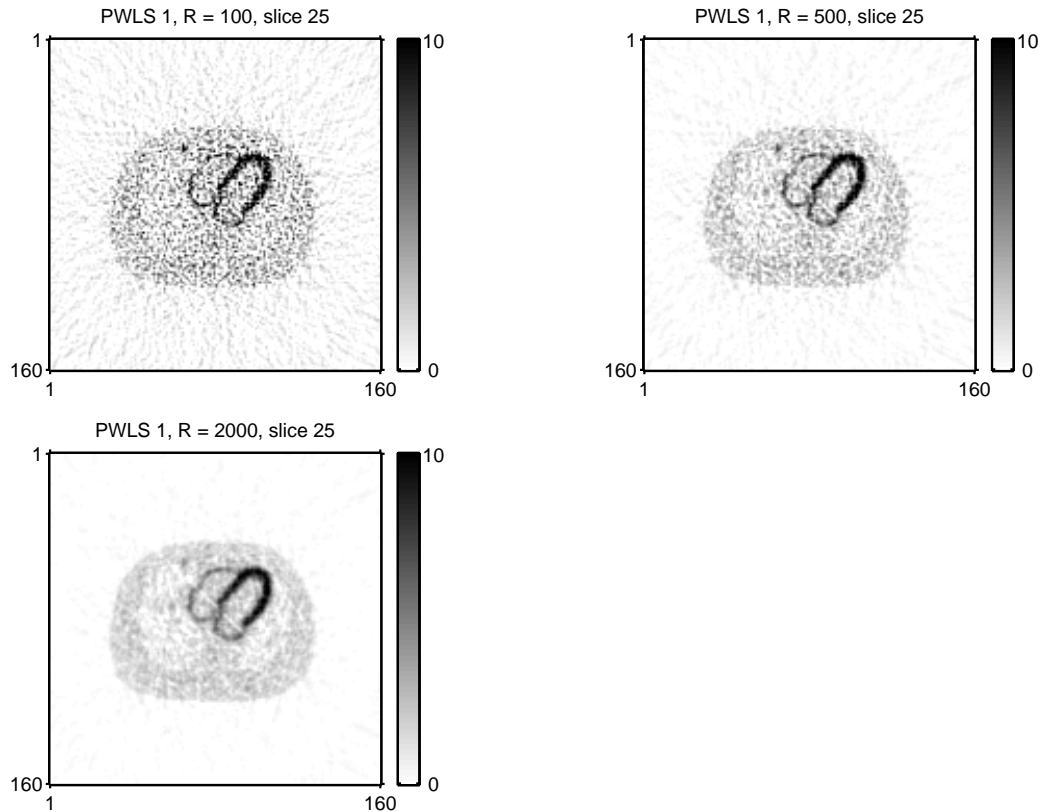
Figure 6.3: PWLS reconstruction with different η_R: 100, 500 and 2000.

because of high noise.

6.2.1 Gated and ungated image reconstructions

Figure 6.5 shows reconstructed images by gated PWLS reconstruction with low count measurements (one frame) and ungated PWLS reconstruction with high count measurements (all frames). The top figure shows severe noise due to low counts and it is not easy to differentiate between lesions and noise. Image structure can not be seen clearly. The bottom figure shows severe motion blurs. Most lesions and myocardium structures are blurred or placed at the wrong locations. These two examples show that utilizing all measurements and compensating for motion are both necessary to obtain good quality reconstructed images. Figure 6.6 shows a reconstructed image with 1M counts and without
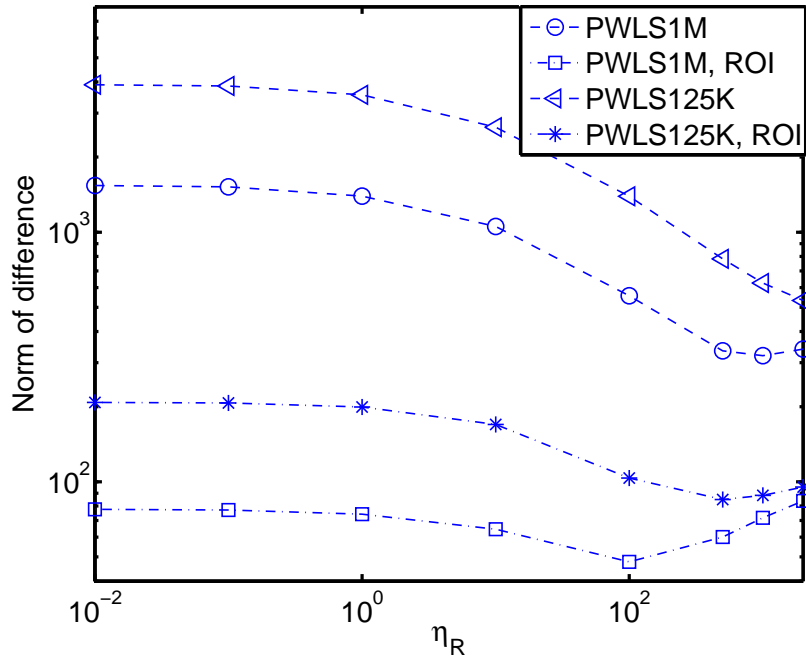
Figure 6.4: Norm of the difference between the true image and reconstructed images with different measurement counts and different spatial regularization parameters.

motion. It shows all 4 lesions better than images in figure 6.5. This figure may be a good reference for the performance of all MCIR methods.

Table 6.1 shows the qualitative results of gated (PWLS125K), ungated (SUM1M), and oracle (PWLS1M) image reconstructions. PWLS125K has the highest norm of difference between the true image and the reconstructed image for the same spatial regularization parameter. SUM1M has superior noise reduction performance for all areas (All) but PWLS125K shows lower norm of difference for ROI. This is an effect of gating, which avoids motion artifacts. Because we use all measurements (1M) and avoid motion artifacts, we may be able to achieve the norm of difference close to 47.8 in PWLS1M as seen in the Table 6.1.
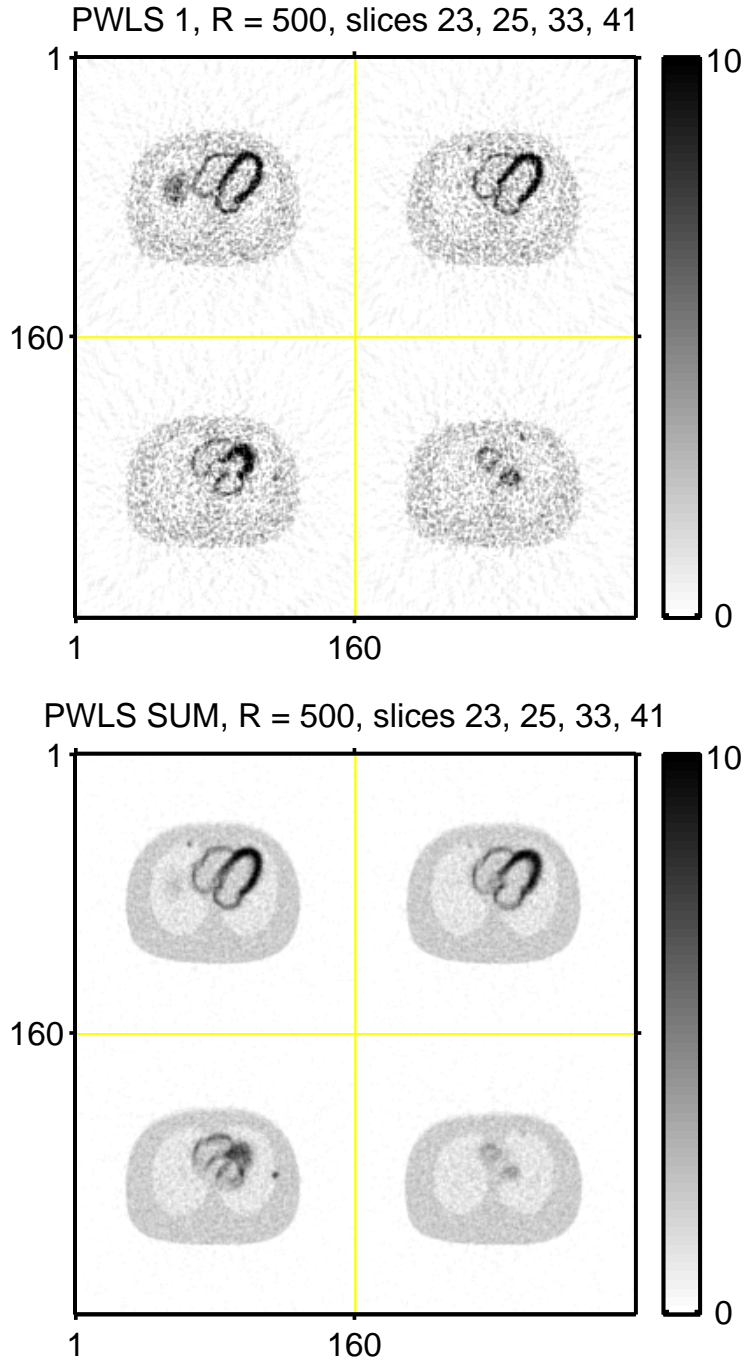
Figure 6.5: PWLS reconstruction with 125K counts (without motion) and 1M counts (with motion). Slices 23, 25, 33, 41.

6.2.2 Post-reconstruction motion compensation

Joint PMC methods with a quadratic motion regularizer and the proposed motion invertibility regularizer described in Chapter 3 were performed in this simulation. Figure 6.7
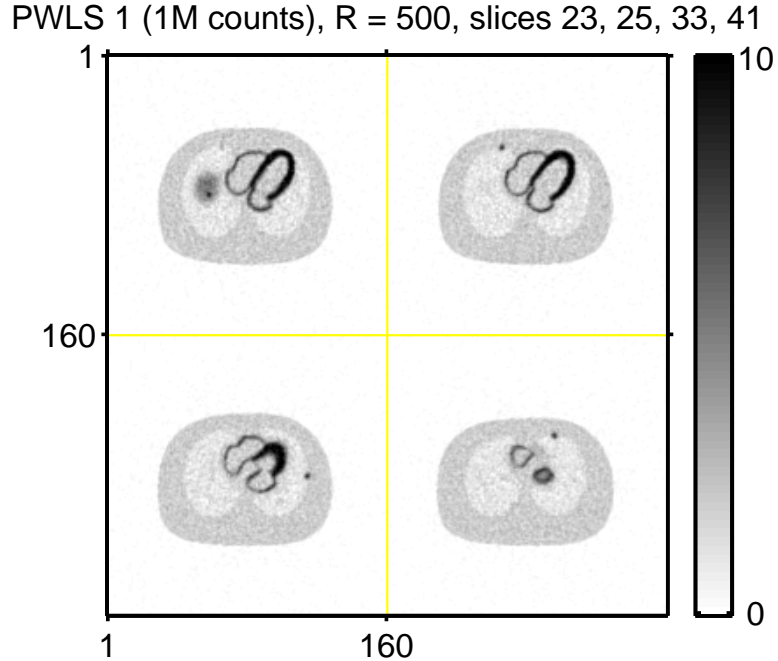
Figure 6.6: PWLS reconstruction with 1M counts, without motion (frame 1: slices 23, 25, 33, 41).

Table 6.1: Norm of difference for PWLS125K and SUM1M with various spatial regularization parameter values. Norms of a true image are 1581.7 (All) and 181.0 (ROI).

Area	Method	η_R			
		100	500	1000	2000
	PWLS1M	556.3	334.8	320.1	340.1
All	PWLS125K	1393.4	782.0	625.9	533.0
	SUM1M	769.2	610.7	587.3	578.6
	PWLS1M	47.8	60.1	71.7	83.9
ROI	PWLS125K	103.5	84.9	88.2	95.3
	SUM1M	106.6	110.6	114.8	119.3

shows PMC reconstructed images with a quadratic spatial regularizer ($\eta_R = 500$) and motion regularizers (a motion invertibility penalty with $\eta_M = 10$ and a motion quadratic penalty with $\eta_M = 0.1$). This figure shows the improvement of reconstructed image quality compared to Figure 6.5 in terms of SNR and motion artifacts. Most lesions show higher visibility, but reconstructing the lesion in the liver seems very challenging.

Figure 6.8 shows the estimated warps (slice 23) from an image at frame 4 to an image
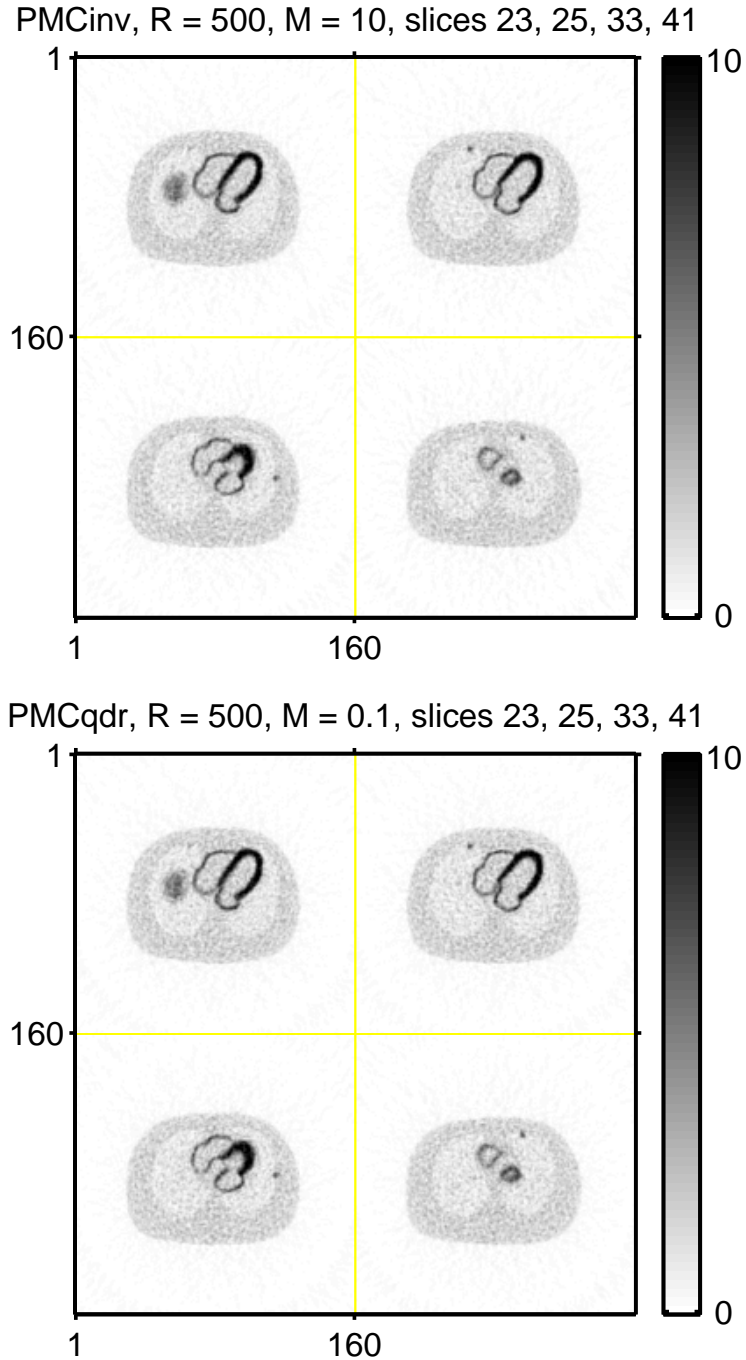
Figure 6.7: PMC reconstruction ($\eta_R = 500$) with invertibility penalty ($\eta_M = 10$, TOP) and quadratic penalty ($\eta_M = 0.1$, BOTTOM) (frame 1: slices 23, 25, 33, 41).

at frame 1 with both a motion quadratic regularizer and a motion invertibility regularizer.

The top left figure shows the estimated warp with a motion invertibility regularizer and

$\eta_M = 10$. As we increase $\eta_M = 1000$, we can have a better regularity in the estimated

warp as seen in the top right figure. Increasing the spatial regularization parameter η_R can regularize the estimated warp better as shown in the bottom left figure. Lastly, bottom right figure shows the estimated warp with a quadratic motion regularizer. Even though this looks more smooth compared to other warps in Figure 6.8, this warp still contains 276 voxels of the negative Jacobian determinant values out of 1228800 voxels. This shows that our proposed motion invertibility regularizer achieved the local invertibility of warps with more flexibility.
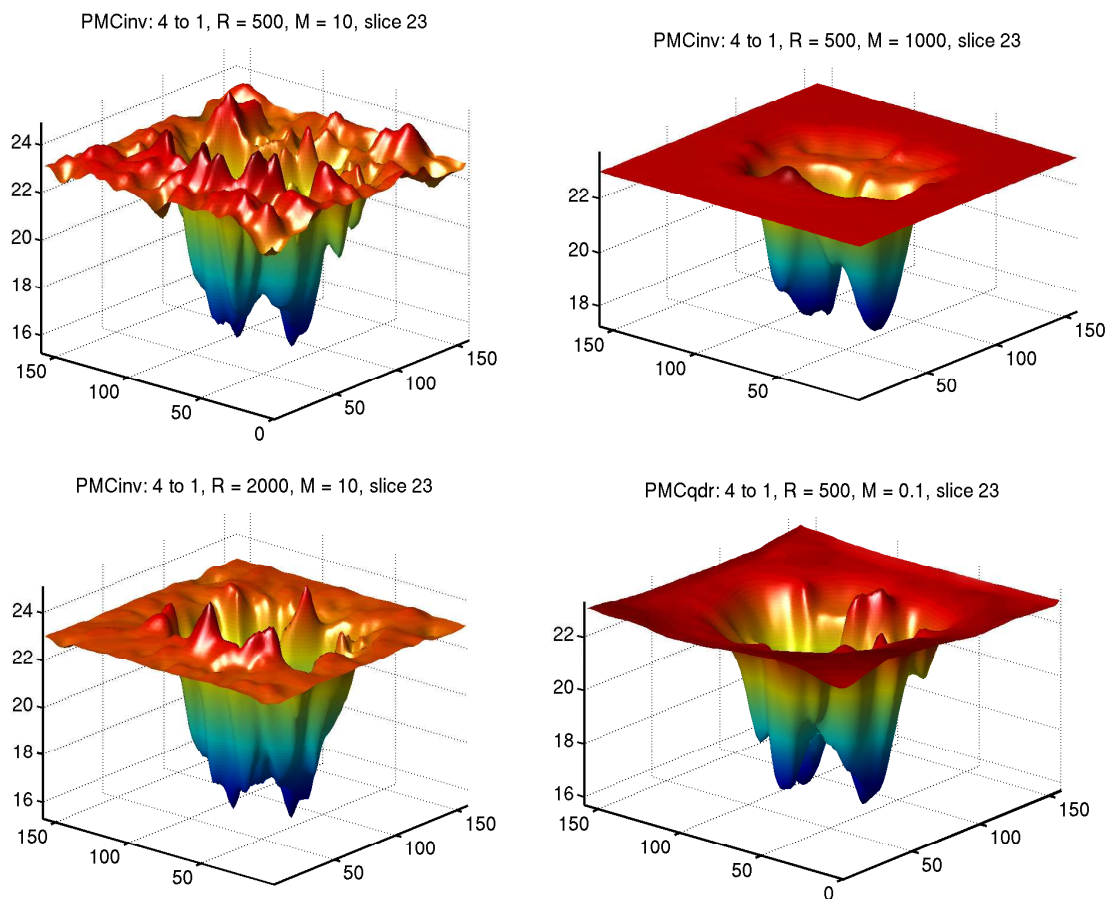
Figure 6.8: Warps that were estimated from individually reconstructed images. Only bottom right warp with quadratic penalty contains 276 points of negative Jacobian determinant value.

Table 6.2 shows the quantitative results of PMC with various regularization parameters. The number of voxels that contain the negative Jacobian determinant values (NJD)

shows that increasing spatial and motion regularization parameters reduces the number of negative Jacobian determinant values. In contrast, increasing spatial and motion regularization parameters may not always decrease the norm of difference between the true image and the reconstructed image. Too large spatial regularization parameter may blur the details of images and too large motion regularization parameter may allow insufficient flexibility of warps so that it may cause a mismatch. The norm of difference in ROI shows this point clearly. The lowest norm of difference in ROI were achieved with not-too-large spatial and motion regularization parameters.

In Table 6.2, PMC with the motion invertibility regularizer (PMCinv) achieved its lowest norm of difference 72.8 at ROI (622.0 at All) when $\eta_R = 100$ and $\eta_M = 10$. PMC with the motion quadratic regularizer (PMCqdr) achieved its lowest norm of difference 73.9 at ROI (655.4 at All) when $\eta_R = 100$ and $\eta_M = 0.1$. Note that NJD are 0 and 1279, respectively. This shows that using the proposed motion invertibility regularizer has better flexibility in terms of achieving local invertibility at each voxel with a similar level of difference norm.

Tables 6.1 and 6.2 show that PMC achieves better norm of difference at both ROI and All areas than gated and ungated image reconstruction methods. The minimum norms of difference for gated and ungated image reconstruction at All and ROI are 533.0 (All) and 84.9 (ROI). The minimum norms of difference for PMC with any motion regularizer are 435.0 (All) and 72.8 (ROI), which are superior to gated and ungated image reconstruction. However, because the nonrigid image registration in PMC was performed with reconstructed images from insufficient measurements, the accuracy of image registration may also be poor. Poor image registration hurts the performance of PMC significantly. Joint estimation of both images and motion may improve the performance and may achieve the performance close to the results of oracle image reconstruction (PWLS1M). The norms of

difference for PWLS1M are 320.1 in All and 47.8 in ROI.

Table 6.2: Norm of difference (All, ROI) and the number of negative Jacobian determinants (NJD) for PMC with various spatial and motion regularization parameters. Norms of a true image are 1581.7 (All) and 181.0 (ROI).

PMCinv		η_R			
Area	η_M	100	500	1000	2000
	0.1	678.8	465.6	437.4	435.0
All	10	622.0	440.4	424.8	430.4
	1000	624.9	434.7	420.4	431.5
	0.1	73.4	80.1	86.5	94.7
ROI	10	72.8	78.4	84.5	94.1
	1000	82.8	86.8	93.5	102.0
	0.1	9667	4538	2616	1126
NJD	10	0	5	0	0
	1000	0	0	0	0
PMCqdr		η_R			
Area	η_M	100	500	1000	2000
	0.01	699.7	481.3	447.9	440.3
All	0.1	655.4	446.7	423.5	426.4
	1	594.0	418.1	408.8	421.9
	0.01	77.0	81.0	88.5	95.5
ROI	0.1	73.9	75.2	84.0	94.6
	1	77.4	82.6	91.9	99.7
	0.01	51313	39431	29599	17422
NJD	0.1	1279	276	28	0
	1	0	0	0	0

6.2.3 Parametric motion model

The alternating optimization for joint PMM also was performed with respect to images and motion. FBP reconstructed images were used as initial images. Initial motion estimates were obtained from FBP reconstructed images with 2-level multiresolution and 100/100 iterations for each level. Then, alternating minimization for joint PMM was performed with 20 (image), 33 (motion), 20 (image), 33 (motion), 20 (image), 33 (motion), and 40 (image) iterations.

Figure 6.9 shows the PMM reconstructed images with a motion invertibility regularizer and a quadratic motion regularizer. Both reconstruction methods improved the quality of reconstructed images and the lesion visibility compared to gated and ungated image reconstructions in Figure 6.5. Figure 6.10 shows warp estimates of PMM with different spatial and motion regularizers. The top left figure shows the estimated warp with $\eta_R = 500$ and $\eta_M = 10$. This warp shows large flexibility, but only contains 45 voxels of negative Jacobian determinant values in 7 mappings and 1,228,800 voxels per each mapping. Increasing η_M can regularize the estimated warp better as seen in the top right figure. Unlike PMC, the estimated warp of PMM does not seem to be regularized much by increasing the spatial regularization parameter η_R as shown in the bottom left figure. It would be important to analyze the relationship between image estimates and motion estimates of PMM since accurate motion estimation is crucial for better performance of MCIR method.

Table 6.3 shows that increasing the spatial regularization parameter η_R causes the reduction of noise in general (All), but also blurs fine details in ROI. Increasing the motion regularization parameter η_M provides locally invertible warps at more voxels, but also limits the degree of freedom in the estimated warps. This lack of flexibility increases the norm of difference in ROI for large motion regularization parameter values. Note that PMMqdr with $\eta_R = 500$ and $\eta_M = 1$ has 987 negative Jacobian determinant values. This is because a too strong motion regularization parameter sometimes causes warps be folded at the boundaries of images. PMMinv shows the lowest norm of difference 63.3 at ROI, which is close to 47.8 at ROI from PWLS1M. It is lower than PMC's lowest norm of 72.8 at ROI. A PMM method is very promising for obtaining good-quality reconstructed images for ROI. However, note that the norm of difference for All is 718.9, which is higher than PMC's 622.0 for All. Analyzing this trade-off between image qualities of PMM at ROI and All would be an interesting future work to improve the performance of PMM image

PMMinv, R = 100, M = 10, slices 23, 25, 33, 41

PMMqdr, R = 100, M = 0.1, slices 23, 25, 33, 41
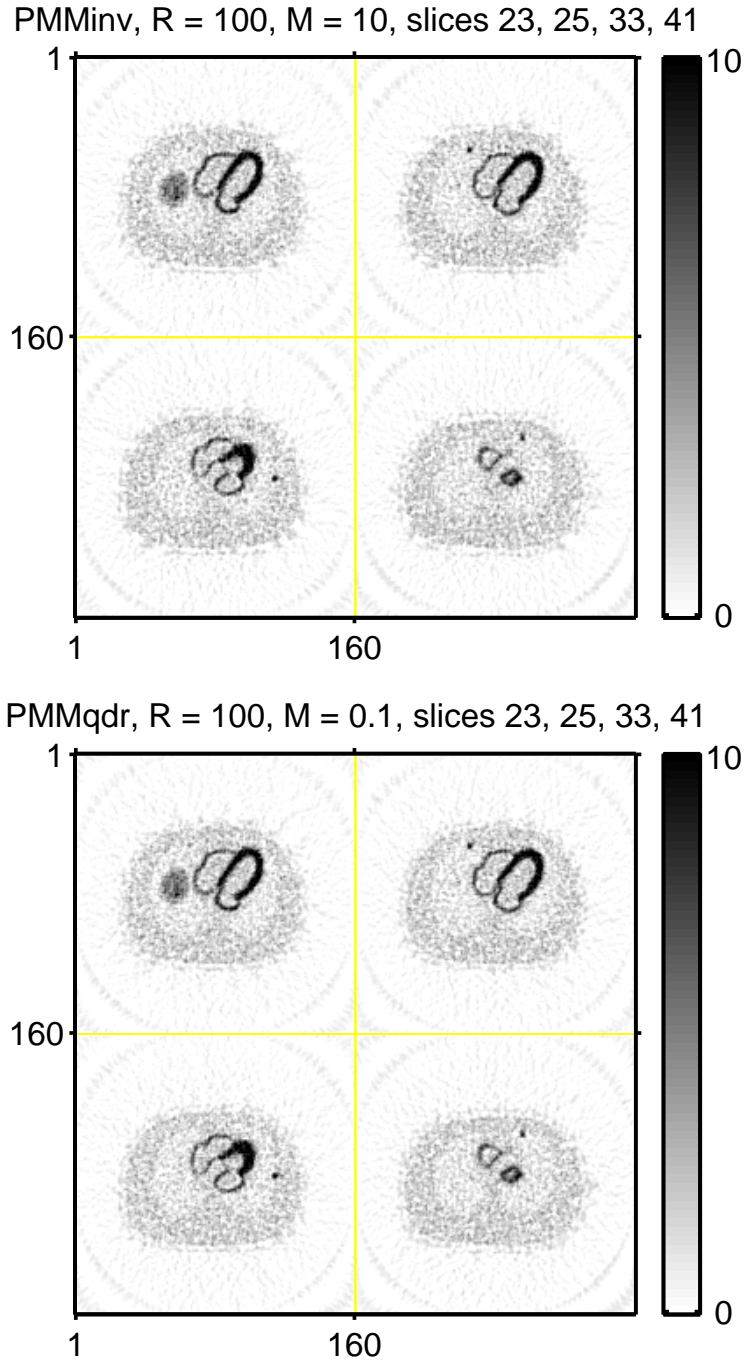
Figure 6.9: PMM reconstruction ($\eta_R = 100$) with invertibility penalty ($\eta_M = 10$) and quadratic penalty ($\eta_M = 0.1$) (frame 1: slices 23, 25, 33, 41).

reconstruction.
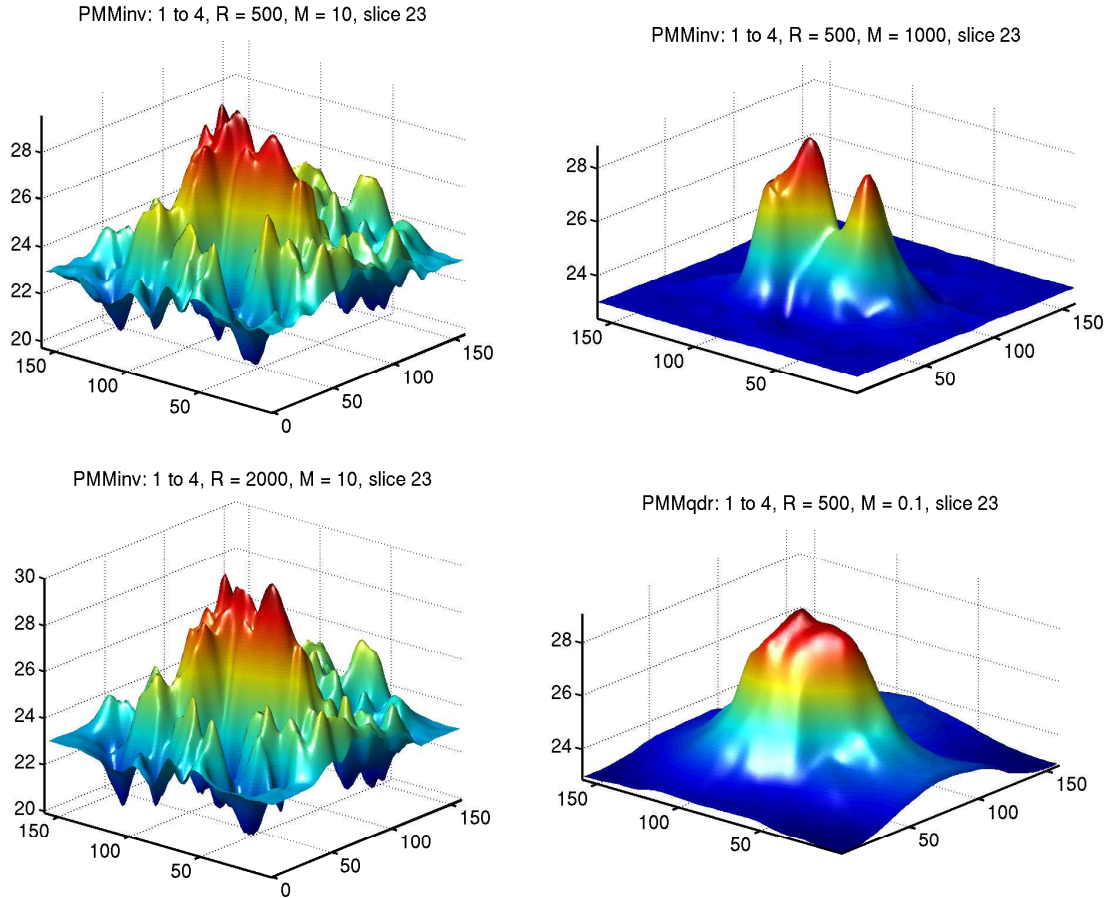
Figure 6.10: Estimated warps of PMM with different spatial and motion regularizers.

6.2.4 Motion-compensated temporal regularization

We performed the optimization for MTR in a similar way as PMM. First, we need to determine ζ for MTR. As discussed in Chapter 5, having large a ζ is important to increase the correlation between estimated images so that MTR can produce better quality images. However, in the practical implementation, having too large ζ may cause a slow convergence in the optimization process. Figure 6.11 shows that too large ζ increases the norm of difference in ROI because we set the maximum iteration number 100 and the image estimate did not converge. We chose $\zeta = 1$ for the rest of MTR simulation.

Figure 6.12 shows that the reconstructed MTR images are also less noisy and less

Table 6.3: Norm of difference (All, ROI) and the number of negative Jacobian determinants (NJD) for PMM with various spatial and motion regularization parameters. Norms of a true image are 1581.7 (All) and 181.0 (ROI).

PMMinv		η_R			
Area	η_M	100	500	1000	2000
	0.1	717.6	547.0	473.4	447.5
All	10	718.9	534.1	465.2	440.7
	1000	680.7	503.0	445.8	
	0.1	67.6	74.1	82.6	93.1
ROI	10	63.3	73.0	82.1	92.5
	1000	75.0	82.6	89.7	
	0.1		156		
NJD	10	243	45	12	29
	1000		0		

PMMqdr		η_R			
Area	η_M	100	500	1000	2000
	0.01	715.6	547.8	472.5	445.5
All	0.1	696.4	517.3	454.8	432.8
	1	685.7	530.2	471.8	
	0.01	66.5	74.4	82.4	93.2
ROI	0.1	67.3	76.1	85.8	95.7
	1	105.3	98.5	99.7	
	0.01		112		
NJD	0.1	66	0	0	0
	1		987		

blurred compared to gated and ungated reconstructed images in Figure 6.5. Figure 6.13 shows the estimated warps in MTR with different motion regularizers and their parameters. The top left figure shows the estimated warp with motion invertibility regularizer ($\eta_R = 500$, $\eta_M = 10$). Increasing η_M regularizes warps as seen in the top right figure, but increasing η_R does not seem to affect the regularity of motion much. The bottom right figure suggests that the quadratic motion regularizer may allow less flexibility than the motion invertibility regularizer.

Table 6.4 shows that a too large spatial regularization parameter η_R and a too large motion regularization parameter η_M increase the norm of difference between the true image
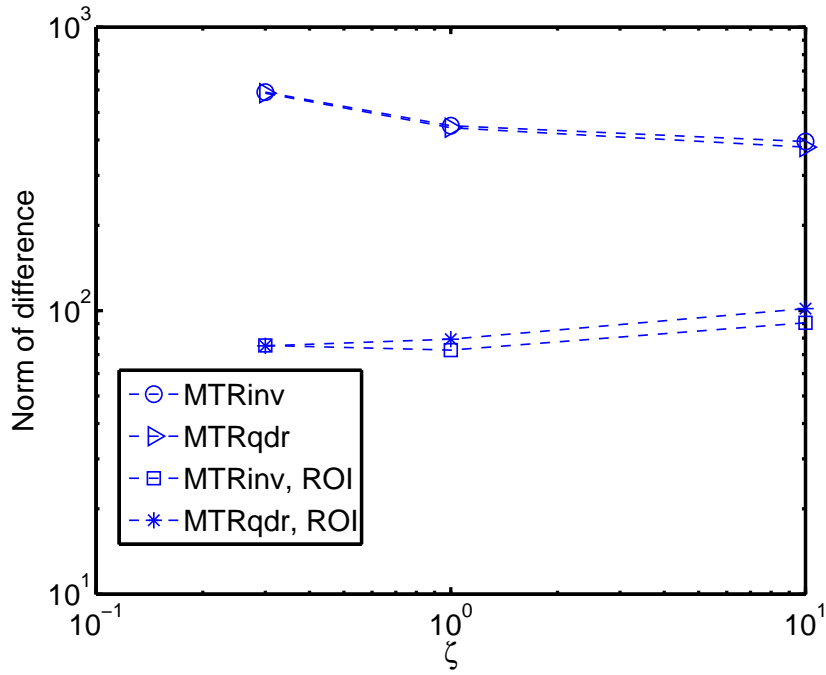
Figure 6.11: Norm of the difference between the true image and reconstructed images with different ζ and different motion regularizers.

and the reconstructed image. This is because a too large η_R may blur image details and a too large η_M may reduce the flexibility of image matching. Note that MTR have very small number of negative Jacobian determinant values compared to PMM or PMC. This is because MTR uses the warps between adjacent image frames, not the warps between frame 1 and frame m.

The lowest norm of difference in MTR is 60.1 at ROI, which is similar to the lowest norm of difference in PMM. However, the norm of difference in MTR for All (533.1) is much lower than the norm of difference in PMM for All (718.9) when each achieves the lowest norm of difference at ROI. For this reason, Figure 6.9 looks more noisy than Figure 6.12. In Chapter 5, we showed that PMM and MTR have the same image reconstruction performance for given motion information. Since motion estimation performance may degrade the image reconstruction performance in joint estimation framework, this result may be explained by an image registration performance analysis in MCIR models.

MTRinv, R = 100, M = 10, slices 23, 25, 33, 41

MTRqdr, R = 100, M = 0.1, slices 23, 25, 33, 41
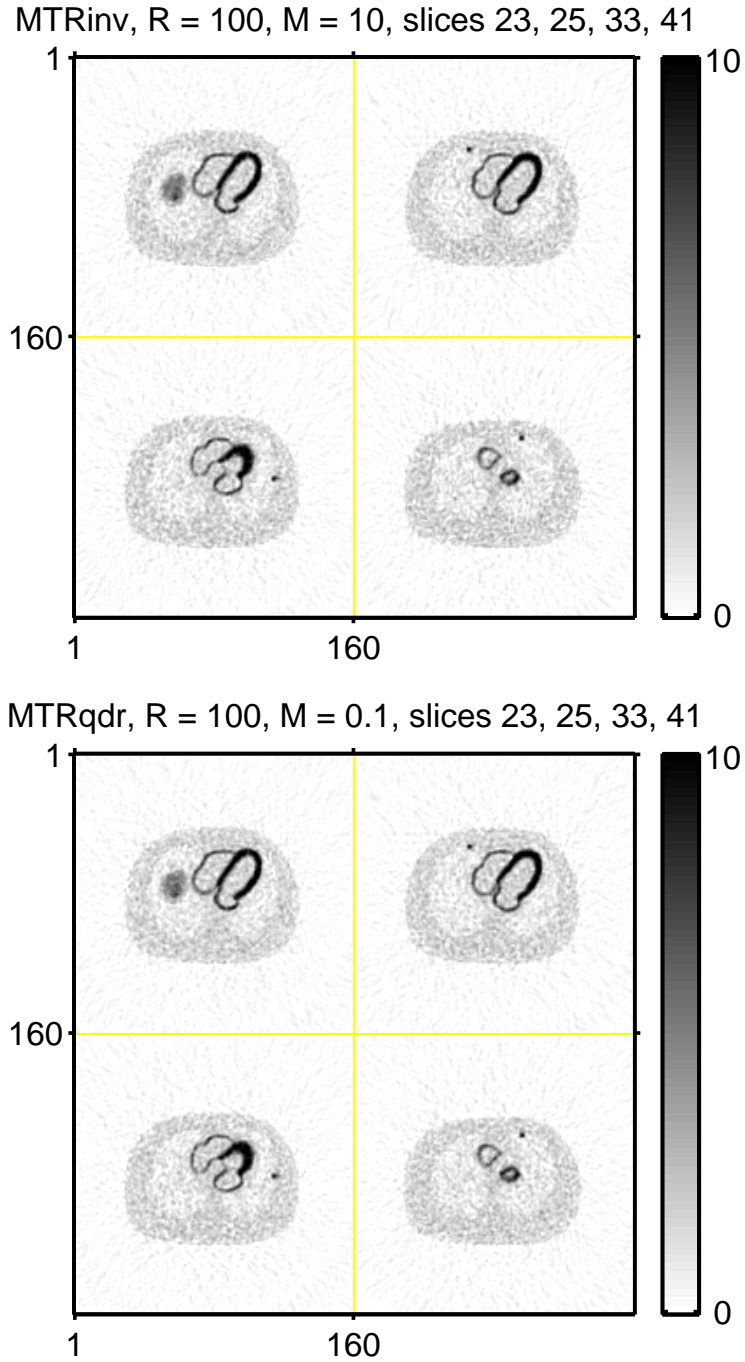
Figure 6.12: MTR reconstruction ($\eta_R = 100$) with motion invertibility regularizer ($\eta_M = 10$) and motion quadratic regularizer ($\eta_M = 0.1$) (frame 1: slices 23, 25, 33, 41).

This will be an interesting future work.

MTRinv: 2 to 3, R = 500, M = 10, slice 23

MTRinv: 2 to 3, R = 500, M = 10000, slice 23

MTRinv: 2 to 3, R = 2000, M = 10, slice 23

MTRqdr: 2 to 3, R = 500, M = 0.1, slice 23
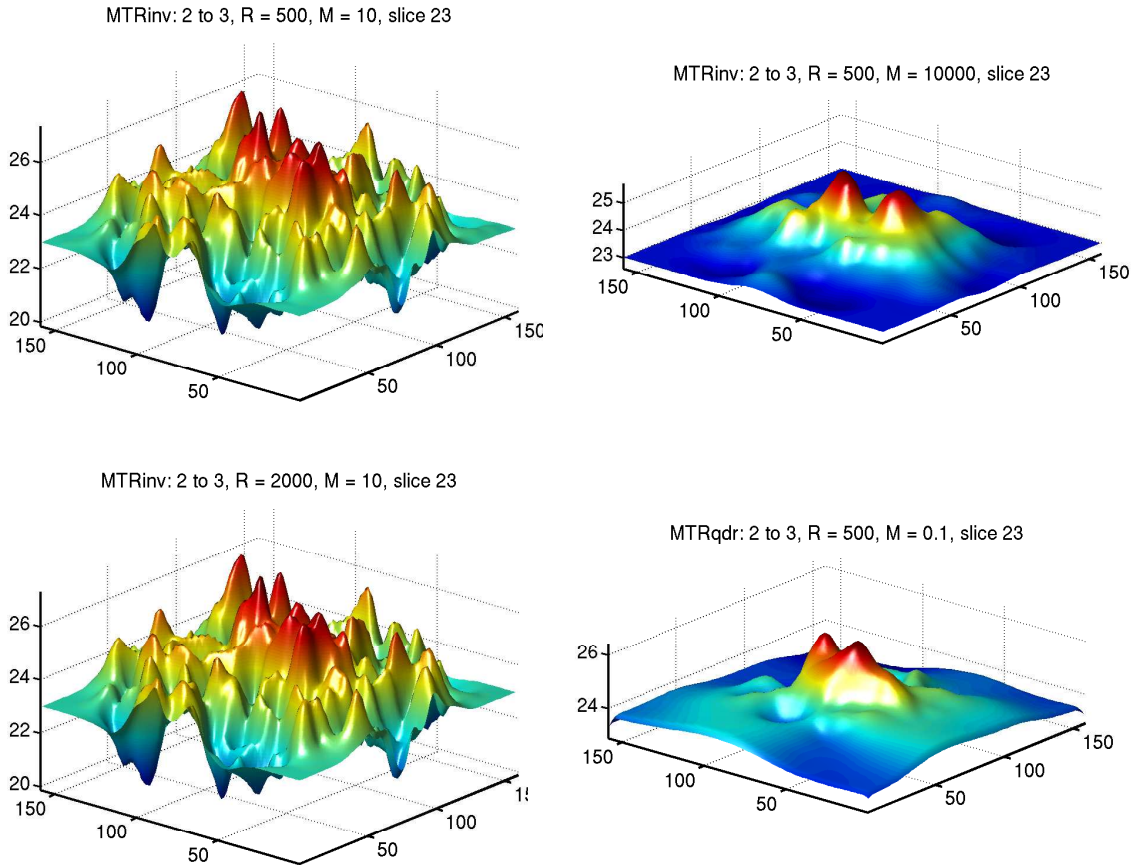
Figure 6.13: Warps of MTR reconstructed images with different spatial and motion regularization parameters.

6.3   Discussion

In this chapter, we investigated MCIR methods in terms of joint image reconstruction and nonrigid motion estimation. Estimated images and motion warps by each MCIR method with different spatial and motion regularizers show how each regularization parameter affects the estimators.

All MCIR methods outperformed gated and ungated image reconstruction in the lesion areas (ROI) and the overall region (All). Motion estimation results with the proposed motion invertibility regularizer and the quadratic motion regularizer show that the proposed method allows more flexibility of warps than a conventional quadratic motion regularizer

Table 6.4: Norm of difference (All, ROI) and the number of negative Jacobian determinants (NJD) for MTR with various spatial and motion regularization parameters ($\zeta = 1$). Norms of a true image are 1581.7 (All) and 181.0 (ROI).

MTRinv		η_R			
Area	η_M	100	500	1000	2000
All	0.1	533.0	451.8	432.7	
	10	528.8	448.9	430.6	433.3
	1000	517.5	442.5	427.0	
	10000		442.1		
ROI	0.1	61.1	73.5	83.5	
	10	61.0	72.6	82.2	92.6
	1000	66.1	76.3	85.4	
	10000		82.0		
NJD	0.1	0	0	0	
	10	0	0	0	0
	1000	0	0	0	
	10000		0		

MTRqdr		η_R			
Area	η_M	100	500	1000	2000
All	0.01	533.1	453.0	433.1	
	0.1	515.7	441.4	426.4	432.4
	1	525.7	451.7	434.9	
ROI	0.01	60.1	73.0	83.3	
	0.1	68.1	79.3	88.4	97.5
	1	78.8	84.9	90.8	
NJD	0.01	28	13	0	
	0.1	0	0	0	0
	1	0	0	0	

and discourages non-invertible deformations well.

There are several possible areas for future work. More realistic PET simulation with attenuation and scattering will be important to investigate. Statistical analysis with more realizations will reveal more statistically meaningful results in joint MCIR methods. Theoretical and empirical analyses of the motion estimation performance in MCIR methods such as Cramer-Rao bound may aid in improving the overall performance of MCIR methods in terms of images and motion. Observer study on the joint MCIR methods is also important for the clinical purpose since it deals with 'false alarm' in non-lesion areas.

We can investigate the motion estimation regularization more as we add a temporal regularizer in PMM or add more constraints in nonrigid motion estimation such as symmetricity or transitivity of warps. Joint MCIR methods are usually computationally demanding. In our simulation, for total 100 iterations of image estimation and 100 iterations of nonrigid motion estimation (4 alternation), it took about 7 hours without multi-threading. Implementing a parallel scheme using graphical processing unit (GPU) may make these methods be more practical in the clinical setting.

CHAPTER 7

Conclusion

7.1 Summary

This dissertation addressed the issues of motion in MCIR models. We investigated motion regularizations based on different motion priors, analyzed the spatial resolution and noise properties of MCIR models with different motion incorporation models, spatial regularization designs to provide uniform spatial resolution in the presence of motion, and joint MCIR methods with different spatial and motion regularizers for 4D XCAT simulation and lesions.

Chapter 3 and 4 proposed motion regularizers that can be used in MCIR models and in general image registration. Chapter 3 proposed a sufficient condition of local invertibility for deformations with nth-order B-spline bases. We also proposed a simple, fast and memory efficient motion regularizer based on the proposed sufficient condition. Chapter 4 investigated the conflict of using both motion invertibility regularizer and tissue rigidity regularizer near the diaphragm and the rib cage, *i.e.*, sliding area. We proposed to relax a motion invertibility regularizer by using a Geman-type function so that we can correct warped bones near the sliding area better and further match image intensity between deformed and target images. It also permitted discontinuous deformation fields near sliding area.

Chapter 5 discussed different MCIR models with known nonrigid motion. We discussed the relationship between different estimators from different MCIR methods. It turns out that MTR converges to PMM estimator as we increase ζ values. We can also match the spatial resolution of both PMM and MTR if we design the regularizers carefully. We also showed that PMC can be the same as PMM as PMC uses weighted average. We also developed a spatial regularization design to provide uniform spatial resolution. It allowed us to match the spatial resolution of one MCIR method to another. Having the same resolution is important to compare the noise properties of MCIR models.

Chapter 6 investigated joint MCIR methods with proposed motion invertibility regularizer. Realistic 4D XCAT phantom and lesions were used for gated PET image reconstruction simulation. Our simulation showed that all MCIR methods improved image quality in terms of SNR and reduces motion artifacts. We also observed that the joint estimation of motion such as PMM and MTR improves images in terms of lesion visibility than PMC. Our result also showed that our proposed motion invertibility regularizer encourages the local invertibility better in a noisy environment and allows more flexibility than a conventional quadratic motion regularizer.

7.2   Future work

The proposed motion invertibility regularizer encourages local invertibility of motion in a fast and memory-efficient way. There are some applications that actually require us to estimate inverse deformations. Combining consistent image registration with the proposed invertibility regularizer may improve the quality of estimated deformations [12].

At the end of Chapter 3, we showed a lemma that gives a sufficient condition that may provide a larger set of local invertibility of motion. This lemma contains many more constraints than the proposed sufficient condition. Implementing image registration with

many constraints in an efficient way will be both challenging and interesting to see.

We proposed a relaxed motion invertibility regularizer to cope with the conflicts between using a motion invertibility regularizer and a tissue rigidity regularizer. However, it is important to investigate more on how to determine design parameters in a Geman function that may be patient-dependent. Another issue can be the B-spline bases for motion and motion discontinuity. Since B-spline bases have finite support, they may be suboptimal for representing discontinuous deformations. Addressing this issue in a more general non-parametric motion estimation will be interesting.

We studied the spatial resolution and noise properties of MCIR methods and proposed a spatial regularization design to provide approximately uniform spatial resolution with translation, rotation and local scaling of same rates in all directions. It will be desirable to deal with motion such as scaling with different rates in different directions and shear motion for spatial regularization design. Developing a spatial regularization design for different imaging modalities, for more realistic system models that include blurring, and with different spatial regularizers such as edge-preserving spatial regularizers could be future studies.

Moreover, more realistic PET simulation with attenuation and scattering will be valuable. Applying to real PET measurements will provide valuable experiments for clinical settings. In our MCIR models, we did not take mass preservation or radio activitity preservation into account. However, it is well-known that the total mass and the total radioactivity are preserved. Investigating modified MCIR models with mass or activity preserving warps will be important.

Joint MCIR methods usually take several hours for one set of measurement data. However, it can be parallelized easily, so that implementing joint MCIR methods with parallel computations such as using GPU will be an important goal for practical use of these mod-

els in the future.

Motion estimation schemes of MCIR models are different. PMM uses maximum-likelihood based motion estimation and MTR uses image registration based on L_2 metric between two estimated images. PMC does not use joint motion estimation. Comparing the performance of motion estimation in different MCIR methods may be crucial to improving the quality of joint MCIR estimates. Cramer-Rao (CR) bound analysis for super-resolution with global translation has been studied thoroughly [79]. CR bound study on MCIR models with nonrigid motion is challenging, but it may provide valuable insights on the performance of MCIR methods in terms of image reconstruction and nonrigid motion estimation.

APPENDICES

APPENDIX A

Algorithms and several gradients/derivatives

A.1 Conjugate gradient and step size

For the cost function $\Psi(\underline{x})$, we want $\underline{x} \in \mathbf{R}^n$ such that

$$\min_{\underline{x}} \Psi(\underline{x})$$

where

$$\underline{x} = \begin{bmatrix} x_1 \\ \vdots \\ x_n \end{bmatrix}$$

To minimize $\Psi(\underline{x}) \in C^2$ for $\underline{x} \in \mathbf{R}^n$ by Conjugate Gradient method where C^2 is a twice differentiable function space, the kth iterative process of the conjugate gradient method is

$$\underline{x}^{k+1} = \underline{x}^k + \gamma \underline{d}^k$$

where

$$\underline{d}^k = \begin{cases} -\nabla\Psi(\underline{x}^k) & k = 0 \\ -\nabla\Psi(\underline{x}^k) + \beta^k \underline{d}^{k-1} & k > 0. \end{cases}$$

There are many ways to determine β^k, but we use the Polak-Ribière-Polyak method,

$$\beta^k = \frac{\nabla\Psi(\underline{x}^k)^T \big(\nabla\Psi(\underline{x}^k) - \nabla\Psi(\underline{x}^{k-1})\big)}{\nabla\Psi(\underline{x}^{k-1})^T \nabla\Psi(\underline{x}^{k-1})}$$

and we set this variable zero when it becomes a negative number. Now our minimization problem of $\Psi(\underline{x})$ with respect to $\underline{x}$ comes down to the minimization problem with respect to γ, *i.e.*,

$$\min_{\underline{x}} \Psi(\underline{x}) = \min_{\gamma} \Psi(\underline{x}^k + \gamma\underline{d}^k).$$

So, multi-dimensional optimization problem becomes a 1D line search problem. Since this is one of the steps in the optimization procedure for $\underline{x}$, we might not have to find an exact γ to minimize this cost function.

To determine the step size γ, we use the first iteration of Newton's method with the initial $\gamma = 0$,

$$\gamma = 0 - \frac{\dot{\Psi}(\underline{x}^k + 0\underline{d}^k)}{\ddot{\Psi}(\underline{x}^k + 0\underline{d}^k)}$$

where

$$
\begin{aligned}
\dot{\Psi}(\underline{x}^k + \gamma\underline{d}^k) &\equiv \frac{\partial \Psi(\underline{x}^k + \gamma\underline{d}^k)}{\partial \gamma} \\
\ddot{\Psi}(\underline{x}^k + \gamma\underline{d}^k) &\equiv \frac{\partial^2 \Psi(\underline{x}^k + \gamma\underline{d}^k)}{\partial \gamma^2}.
\end{aligned}
$$

A.2 Gradients/derivatives of weighted least square with motion

The weighted least square (WLS) data fitting term is

$$\Psi(\boldsymbol{c}, \underline{\alpha}) = \|\boldsymbol{y} - \boldsymbol{A}\breve{\boldsymbol{T}}(\underline{\alpha})\boldsymbol{c}\|_{\boldsymbol{W}}^2$$

where

$$[\breve{\boldsymbol{T}}(\underline{\alpha})]_{(xyz),(ijk)} = \omega\big(x + d(\underline{r}; \underline{\alpha}^x) - i\big)\omega\big(y + d(\underline{r}; \underline{\alpha}^y) - j\big)\omega\big(z + d(\underline{r}; \underline{\alpha}^z) - k\big)$$

and $\underline{r} = (x, y, z)$. We assume that

$$d(\underline{r}; \underline{\alpha}^q) = \boldsymbol{B}\underline{\alpha}^q.$$

The gradient of Ψ with respect to image $\boldsymbol{c}$ is straight forward

$$\nabla_{\boldsymbol{c}}\Psi(\boldsymbol{c},\underline{\alpha}) = 2\breve{\boldsymbol{T}}(\underline{\alpha})'\boldsymbol{A}'\boldsymbol{W}(\boldsymbol{A}\breve{\boldsymbol{T}}(\underline{\alpha})\boldsymbol{c} - \boldsymbol{y}). \tag{A.1}$$

The gradient of Ψ with respect to motion $\underline{\alpha}$ is

$$\nabla_{\underline{\alpha}}\Psi(\boldsymbol{c},\underline{\alpha}) = \begin{bmatrix} 2\boldsymbol{B}'\mathrm{diag}\left\{\partial_x\breve{\boldsymbol{T}}(\underline{\alpha})\boldsymbol{c}\right\}\boldsymbol{A}'\boldsymbol{W}(\boldsymbol{A}\breve{\boldsymbol{T}}(\underline{\alpha})\boldsymbol{c} - \boldsymbol{y}) \\ 2\boldsymbol{B}'\mathrm{diag}\left\{\partial_y\breve{\boldsymbol{T}}(\underline{\alpha})\boldsymbol{c}\right\}\boldsymbol{A}'\boldsymbol{W}(\boldsymbol{A}\breve{\boldsymbol{T}}(\underline{\alpha})\boldsymbol{c} - \boldsymbol{y}) \\ 2\boldsymbol{B}'\mathrm{diag}\left\{\partial_z\breve{\boldsymbol{T}}(\underline{\alpha})\boldsymbol{c}\right\}\boldsymbol{A}'\boldsymbol{W}(\boldsymbol{A}\breve{\boldsymbol{T}}(\underline{\alpha})\boldsymbol{c} - \boldsymbol{y}) \end{bmatrix} \tag{A.2}$$

where

$$[\partial_x\breve{\boldsymbol{T}}(\underline{\alpha})]_{(xyz),(ijk)} = \dot{\omega}\big(x + d(\underline{r};\underline{\alpha}^x) - i\big)\omega\big(y + d(\underline{r};\underline{\alpha}^y) - j\big)\omega\big(z + d(\underline{r};\underline{\alpha}^z) - k\big)$$

$$[\partial_y\breve{\boldsymbol{T}}(\underline{\alpha})]_{(xyz),(ijk)} = \omega\big(x + d(\underline{r};\underline{\alpha}^x) - i\big)\dot{\omega}\big(y + d(\underline{r};\underline{\alpha}^y) - j\big)\omega\big(z + d(\underline{r};\underline{\alpha}^z) - k\big)$$

$$[\partial_z\breve{\boldsymbol{T}}(\underline{\alpha})]_{(xyz),(ijk)} = \omega\big(x + d(\underline{r};\underline{\alpha}^x) - i\big)\omega\big(y + d(\underline{r};\underline{\alpha}^y) - j\big)\dot{\omega}\big(z + d(\underline{r};\underline{\alpha}^z) - k\big)$$

and $\dot{\omega}(x) = \partial\omega(x)/\partial x$.

As we have search directions of image $\underline{d}_{\boldsymbol{c}}$ and motion $\underline{d}_{\underline{\alpha}}$ by CG respectively, the step size of them can be determined as follows. For $\Psi(\boldsymbol{c} + \gamma\underline{d}_{\boldsymbol{c}},\underline{\alpha})$, the first derivative of it with respect to γ at $\gamma = 0$ is

$$\dot{\Psi}(\boldsymbol{c},\underline{\alpha}) = \nabla_{\boldsymbol{c}}\Psi(\boldsymbol{c},\underline{\alpha}) \cdot \underline{d}_{\boldsymbol{c}} \tag{A.3}$$

and the second derivative is

$$\ddot{\Psi}(\boldsymbol{c},\underline{\alpha}) = \|\boldsymbol{A}\breve{\boldsymbol{T}}(\underline{\alpha})\underline{d}_{\boldsymbol{c}}\|_{\boldsymbol{W}}^2 \tag{A.4}$$

For $\Psi(\boldsymbol{c},\underline{\alpha} + \gamma\underline{d}_{\underline{\alpha}})$, the first derivative of it with respect to γ at $\gamma = 0$ is

$$\dot{\Psi}(\boldsymbol{c},\underline{\alpha}) = \nabla_{\underline{\alpha}}\Psi(\boldsymbol{c},\underline{\alpha}) \cdot \begin{bmatrix} \underline{d}_{\underline{\alpha}^x} \\ \underline{d}_{\underline{\alpha}^y} \\ \underline{d}_{\underline{\alpha}^z} \end{bmatrix} \tag{A.5}$$

where

$$\underline{\alpha} + \gamma \underline{d}_{\underline{\alpha}} = \begin{bmatrix} \underline{\alpha}^x + \gamma \underline{d}_{\underline{\alpha}^x} \\ \underline{\alpha}^y + \gamma \underline{d}_{\underline{\alpha}^y} \\ \underline{\alpha}^z + \gamma \underline{d}_{\underline{\alpha}^z} \end{bmatrix}.$$

The second derivative is

$$\ddot{\Psi}(\boldsymbol{c}, \underline{\alpha}) \approx 2 \left\| \begin{bmatrix} \boldsymbol{A}\mathrm{diag}\left\{\partial_x \check{\boldsymbol{T}}(\underline{\alpha})\boldsymbol{c}\right\} \boldsymbol{B}\underline{d}_{\underline{\alpha}^x} \\ \boldsymbol{A}\mathrm{diag}\left\{\partial_y \check{\boldsymbol{T}}(\underline{\alpha})\boldsymbol{c}\right\} \boldsymbol{B}\underline{d}_{\underline{\alpha}^y} \\ \boldsymbol{A}\mathrm{diag}\left\{\partial_z \check{\boldsymbol{T}}(\underline{\alpha})\boldsymbol{c}\right\} \boldsymbol{B}\underline{d}_{\underline{\alpha}^z} \end{bmatrix} \right\|_{\boldsymbol{W}}^2 \tag{A.6}$$

where we approximate this equation by eliminating all the second order derivatives for $\check{\boldsymbol{T}}(\underline{\alpha})$ since the second order values tend to be unstable in high noise [73].

APPENDIX B

Proofs of Lemmas for invertibility sufficient condition

B.1   Proof of Lemma 3.1

Proof. The global maximum and minimum values exist since $|\mathbf{J}|$ is continuous on the compact set $I_1 \times \cdots \times I_9$. Suppose that $(x_1, \cdots, x_9)$ achieves the global minimum value of $|\mathbf{J}|$ and $\min I_k < x_k < \max I_k$ for some k. Fix all x_i except x_k, $|\mathbf{J}|$ is an affine function with respect to x_k so $|\mathbf{J}|$ can achieve equal or better global minimum value on either $x_k = \min I_k$ or $x_k = \max I_k$. The same argument can be applied for all x_i such that $\min I_i < x_i < \max I_i$ and thus it generates a contradiction. The same argument can be applied to the global maximum case. $\qquad\square$

B.2   Proof of Lemma 3.2

Proof. By Lemma 3.1, we need to evaluate $|\mathbf{J}|$ only on $x_1 \in \{-k_x, K_x\}$, $x_4 \in \{-k_y, K_y\}$, $x_9 \in \{-k_z, K_z\}$ and $x_i \in \{-k_{q_i}, k_{q_i}\}$ where $q_i = x$ for $i = 2, 3$, $q_i = y$ for $i = 4, 6$ and $q_i = z$ for $i = 7, 8$. For fixed x_i except x_1, $|\mathbf{J}(x_1)| = (1+x_1)\{(1+x_5)(1+x_9) - x_6 x_8\} + c$ where c is a constant for x_1 and $(1 + x_5)(1 + x_9) - x_6 x_8$ is always positive under given conditions. So $x_1 = K_x$ for $\max |\mathbf{J}|$ and $x_1 = -k_x$ for $\min |\mathbf{J}|$. Similarly we determine x_5 and x_9. For fixed x_i except x_2, $|\mathbf{J}(x_2)| = x_2\{x_6 x_7 - (1 + x_9)x_4\} + c$ where c is a constant

for x_2. For min $|\mathbf{J}|$, $x_2 = -k_x$ if $x_4 = -k_y$ and $x_2 = k_x$ if $x_4 = k_y$. In other words, $x_2 x_4 = k_x k_y$ for min $|\mathbf{J}|$. Similarly, $x_2 x_4 = -k_x k_y$ for max $|\mathbf{J}|$. In this fashion, $x_6 x_8$ and $x_3 x_7$ will be determined for max $|\mathbf{J}|$ and min $|\mathbf{J}|$. From these results, one can induce that $x_2 x_6 x_7 + x_3 x_4 x_8 = 0$ for max $|\mathbf{J}|$ and $x_2 x_6 x_7 = x_3 x_4 x_8 = -k_x k_y k_z$ for min $|\mathbf{J}|$. $\qquad\square$

B.3   Proof of Lemma 3.3

Proof. For $d(x) = \sum_i c_i \beta^n(x/m_x - i)$, by using $\frac{\partial}{\partial x}\beta^n(x) = \beta^{n-1}(x+1/2) - \beta^{n-1}(x-1/2)$ in [106]

$$
\begin{aligned}
\frac{\partial}{\partial x} d(x) &= \sum_i c_i \frac{\partial}{\partial x}\beta^n(x/m_x - i) \\
&= \sum_i (c_i - c_{i-1})\beta^{n-1}(x/m_x - i + 1/2)/m_x.
\end{aligned}
$$

Using the constraints $b_m \le \alpha^q_{i+1,j,k} - \alpha^q_{i,j,k} \le b_M$ and the property $\sum_i \beta^n(x/m_x - i) = 1$, we have the bounds

$$
\frac{\partial}{\partial x} d^q(\underline{r}) = \sum_{i,j,k}(\alpha^q_{i,j,k} - \alpha^q_{i-1,j,k})\beta^{n-1}(x/m_x - i + 1/2)
$$

$$
\beta^n(y/m_y - j)\beta^n(z/m_z - k)/m_x
$$

$$
\le b_M/m_x \sum_i \beta^{n-1}(x/m_x - i + 1/2)
$$

$$
\cdot \sum_j \beta^n(y/m_y - j)\sum_k \beta^n(z/m_z - k)
$$

$$
\le b_M/m_x.
$$

Similarly, $\frac{\partial}{\partial x}d^q(\underline{r}) \ge b_m/m_x$. The other directions y, z can be proved similarly. $\qquad\square$

B.4   Proof of Lemma 3.5

Proof. For 2D Jacobian determinant we use the same B-spline properties in the proof of

Lemma 3.3

$$
|\mathbf{J}| = \left(1 + \frac{\partial}{\partial x} d^x(\underline{r})\right)\left(1 + \frac{\partial}{\partial y} d^y(\underline{r})\right) - \frac{\partial}{\partial x} d^y(\underline{r}) \frac{\partial}{\partial y} d^x(\underline{r})
$$

$$
= \sum_{i,j} \sum_{i',j'} \left\{ \left(1 + \frac{\alpha^x_{i+1,j} - \alpha^x_{i,j}}{m_x}\right)\left(1 + \frac{\alpha^y_{i',j'+1} - \alpha^y_{i',j'}}{m_y}\right) - \right.
$$

$$
\left. \frac{\alpha^y_{i+1,j} - \alpha^y_{i,j}}{m_x} \frac{\alpha^x_{i',j'+1} - \alpha^x_{i',j'}}{m_y} \right\} \beta^{n-1}(x/m_x - i + 1/2)
$$

$$
\beta^n(y/m_y - j)\beta^n(x/m_x - i')\beta^{n-1}(y/m_y - j' + 1/2).
$$

$\beta^{n-1}(x/m_x - i + 1/2)\beta^n(x/m_x - i') = 0$ for $i' < i - n + 1$ or $i' > i + n$ and $\beta^n(y/m_y -$

$j)\beta^{n-1}(y/m_y - j' + 1/2) = 0$ for $j' < j - n$ or $j' > j + n - 1$. 3D case is similar. $\square$

APPENDIX C

Proofs of properties for warps.

C.1 Adjoint operator of $\mathcal{T}$

Assume that we have a continuous operator $\mathcal{T} : \mathcal{X} \rightarrow \mathcal{X}$ where $\mathcal{X}$ is the set of images over the domain $\mathbf{R}^n$. Assume that we have images $f \in \mathcal{X}$ and $g \in \mathcal{X}$ and that $g = \mathcal{T}f$. We define a transformation T such that $g(x) = (\mathcal{T}f)(x) = f(T(x))$, $x \in \mathbf{R}^n$. We assume that $\mathcal{T} : \mathcal{X} \rightarrow \mathcal{X}$ is invertible.

Adjoint operator $\mathcal{T}'$ of an operator $\mathcal{T}$ is defined as follows:

$$\langle g, \mathcal{T}f \rangle = \langle f, \mathcal{T}'g \rangle$$

where $\langle, \rangle$ denotes an inner product. Here we use the usual L_2 inner product. By a simple change of variable, we can get

$$
\begin{aligned}
\langle g, \mathcal{T}f \rangle &= \int g(x)(\mathcal{T}f)(x)dx \\
&= \int g(x)f(T(x))dx \\
&= \int f(y)\frac{1}{|\nabla T(T^{-1}(y))|}g(T^{-1}(y))dy \\
&= \langle f, \mathcal{T}'g \rangle
\end{aligned}
$$

where $y = T(x)$ and $|\nabla T(T^{-1}(y))|$ is the determinant of Jacobian matrix of T. We define

an operator $\mathcal{D}_T$ such that

$$g = \mathcal{D}_T f \quad \text{iff} \quad g(x) = \frac{1}{|\nabla T(x)|} f(x) \, , \forall x.$$

Then, the adjoint operator $\mathcal{T}'$ is given by

$$\mathcal{T}' = \mathcal{T}^{-1} \mathcal{D}_T. \tag{C.1}$$

Therefore, in continuous space, the adjoint of an invertible nonrigid warp is the product of the inverse of the warp with a diagonal operator based on the Jacobian determinant of the warp.

Now we apply this result to the discrete space operators $\boldsymbol{T}_{m,n}$ considered in (2.10). Using (C.1), we approximate the transpose of $\boldsymbol{T}_{m,n}$ as follows:

$$\boldsymbol{T}'_{m,n} \approx \boldsymbol{T}^{-1}_{m,n} \text{diag} \left\{ \frac{1}{|\nabla \boldsymbol{T}_{m,n}|_j} \right\} \approx \boldsymbol{T}_{n,m} \text{diag} \left\{ \frac{1}{|\nabla \boldsymbol{T}_{m,n}|_j} \right\}. \tag{C.2}$$

C.2 Uniform spatial resolution for 2D linear transformation

The continuous-space analogue of the uniform spatial resolution system (5.33) combined with a linear transformation $\mathcal{T}$ and an inverse transformation $\mathcal{T}^{-1}$ can be represented

$$\mathcal{T}^{-1} \mathcal{Q}' \mathcal{D} \left(\frac{1/|\rho|}{1/|\rho| + \eta \mathcal{R}(\rho, \Phi)} \right) \mathcal{Q} \mathcal{T} \tag{C.3}$$

where $\rho = \sqrt{u^2 + v^2}$ in the frequency domain (u, v), $\mathcal{Q}$ is a Fourier operator, and $\mathcal{T}$ corresponds to the linear transform

$$T(x, y) = \begin{bmatrix} a & b \\ c & d \end{bmatrix} \begin{bmatrix} x \\ y \end{bmatrix}.$$

As we assume that we have an input function $f(x, y)$ such that its Fourier transform $F(u, v)$, it is easy to show that the Fourier transform of $f(T(x, y))$ would be

$$\frac{1}{|\nabla T(u, v)|} F(T^{-1}(u, v)).$$

Therefore, the equivalent local frequency response for (C.3) would be

$$\frac{1/|\rho'|}{1/|\rho'| + \eta \mathcal{R}(\rho, \Phi)} = \frac{1}{1 + \eta |\rho'| \mathcal{R}(\rho, \Phi)} \tag{C.4}$$

where $|\rho'| = \|T(u, v)\|_2$.

We would like to modify a regularizer $\mathcal{R}(\cdot)$ so that

$$|\rho'| \mathcal{R}(\rho, \Phi) \approx (2\pi)^2 (\rho)^3. \tag{C.5}$$

For a quadratic spatial regularizer, we can rewrite (C.5) as follows:

$$\|T(u, v)\|_2 \left(\tilde{a} u^2 + \tilde{b} uv + \tilde{c} v^2 \right)^2 \approx (2\pi)^2 (u^2 + v^2)^3. \tag{C.6}$$

Therefore, the problem becomes to determine three free parameters $\tilde{a}, \tilde{b}$ and $\tilde{c}$ to approximate (C.6) which requires matching seven different terms. Regularizer designs to match the desired local impulse responses have been well-studied in Shi *et al.* [89]. Similar technique can be applied to our problem.

BIBLIOGRAPHY

BIBLIOGRAPHY

[1] S. Ahn and R. M. Leahy. Analysis of resolution and noise properties of nonquadratically regularized image reconstruction methods for PET. *IEEE Trans. Med. Imag.*, 27(3):413–24, March 2008.

[2] A. M. Alessio and P. E. Kinahan. Improved quantitation for PET/CT image reconstruction with system modeling and anatomical priors. *Med. Phys.*, 33(11):4095–103, November 2006.

[3] EG Amparo, CB Higgins, D Farmer, G Gamsu, and M McNamara. Gated MRI of cardiac and paracardiac masses: initial experience. *Am. J. Roentgenol.*, 143(6):1151–1156, 1984.

[4] E. Asma and R. M. Leahy. Mean and covariance properties of dynamic PET reconstructions from list-mode data. *IEEE Trans. Med. Imag.*, 25(1):42–54, January 2006.

[5] E. Asma, R. Manjeshwar, and K. Thielemans. Theoretical comparison of motion correction techniques for PET image reconstruction. In *Proc. IEEE Nuc. Sci. Symp. Med. Im. Conf.*, volume 3, pages 1762–7, 2006.

[6] W. Bai and M. Brady. Regularized B-spline deformable registration for respiratory motion correction in PET images. *Phys. Med. Biol.*, 54(9):2719–36, May 2009.

[7] S. Baker and T. Kanade. Limits on super-resolution and how to break them. *Pattern Analysis and Machine Intelligence, IEEE Transactions on*, 24(9):1167–1183, Sep 2002.

[8] A. Blake and A. Zisserman. *Visual reconstruction*. MIT Press, Cambridge, MA, 1987.

[9] Z. Cao, D. R. Gilland, B. A. Mair, and R. J. Jaszczak. Three-dimensional motion estimation with image reconstruction for gated cardiac ECT. *IEEE Trans. Nuc. Sci.*, 50(3):384–8, June 2003.

[10] J. Jeffrey Carr, III Crouse, John R., Jr. Goff, David C., Jr. D'Agostino, Ralph B., Neil P. Peterson, and Gregory L. Burke. Evaluation of Subsecond Gated Helical CT for Quantification of Coronary Artery Calcium and Comparison with Electron Beam CT. *Am. J. Roentgenol.*, 174(4):915–921, 2000.

[11] Y. Choi and S. Lee. Injectivity conditions of 2D and 3D uniform cubic B-spline functions. *Graphical Models*, 62(6):411–27, 2000.

[12] G. E. Christensen and H. J. Johnson. Consistent image registration. *IEEE Trans. Med. Imag.*, 20(7):568–82, July 2001.

[13] S. Chun and J. A. Fessler. Regularized methods for topology-preserving smooth nonrigid image registration using b-spline basis. In *Proc. IEEE Intl. Symp. Biomed. Imag.*, pages 1099–102, 2008.

[14] S. Y. Chun and J. A. Fessler. Joint image reconstruction and nonrigid motion estimation with a simple penalty that encourages local invertibility. In *Proc. SPIE 7258, Medical Imaging 2009: Phys. Med. Im.*, page 72580U, 2009.

[15] S. Y. Chun and J. A. Fessler. A simple regularizer for B-spline nonrigid image registration that encourages local invertibility. *IEEE J. Sel. Top. Sig. Proc.*, 3(1):159–69, February 2009. Special Issue on Digital Image Processing Techniques for Oncology.

[16] S. Y. Chun and J. A. Fessler. Spatial resolution and noise properties of regularized motion-compensated image reconstruction. In *Proc. IEEE Intl. Symp. Biomed. Imag.*, 2009. To appear as 1361. oral TO3.R1.2.

[17] S. Y. Chun, J. A. Fessler, and M. L. Kessler. A simple penalty that encourages local invertibility and considers sliding effects for respiratory motion. In *Proc. SPIE 7259, Medical Imaging 2009: Image Proc.*, page 72592U, 2009.

[18] W R Crum, T Hartkrns, and D L G Hill. Non-rigid image registration: theory and practice. *The British Journal of Radiology*, 77:S140–S153, 2004.

[19] M. Dawood, N. Lang, X. Jiang, and K. P. Schafers. Lung motion correction on respiratory gated 3-D PET/CT images. *IEEE Trans. Med. Imag.*, 25(4):476–85, April 2006.

[20] M. Elad and A. Feuer. Restoration of a single superresolution image from several blurred, noisy, and undersampled measured images. *IEEE Trans. Im. Proc.*, 6(12):1646–58, December 1997.

[21] H. Fayad, F. Lamare, V. Bettinardi, C. Roux, and D. Visvikis. Respiratory synchronized ct image generation from 4d pet acquisitions. In *Nuclear Science Symposium Conference Record, 2008. NSS '08. IEEE*, pages 5488–5492, Oct 2008.

[22] J. A. Fessler. Penalized weighted least-squares image reconstruction for positron emission tomography. *IEEE Trans. Med. Imag.*, 13(2):290–300, June 1994.

[23] J. A. Fessler. Mean and variance of implicitly defined biased estimators (such as penalized maximum likelihood): Applications to tomography. *IEEE Trans. Im. Proc.*, 5(3):493–506, March 1996.

[24] J. A. Fessler and W. L. Rogers. Spatial resolution properties of penalized-likelihood image reconstruction methods: Space-invariant tomographs. *IEEE Trans. Im. Proc.*, 5(9):1346–58, September 1996.

[25] R. Fransens, C. Strecha, and L. Van Gool. Optical flow based super-resolution: A probabilistic approach. *Comp. Vision & Im. Understanding*, 106(1):106–15, April 2007.

[26] S. Geman and D. Geman. Stochastic relaxation, Gibbs distributions, and Bayesian restoration of images. *IEEE Trans. Patt. Anal. Mach. Int.*, 6(6):721–41, November 1984.

[27] D. R. Gilland, B. A. Mair, J. E. Bowsher, and R. J. Jaszczak. Simultaneous reconstruction and motion estimation for gated cardiac ECT. *IEEE Trans. Nuc. Sci.*, 49(5):2344–9, October 2002.

[28] G. H. Golub and C. F. Van Loan. *Matrix computations*. Johns Hopkins Univ. Press, 2 edition, 1989.

[29] E. Gravier, Y. Yang, and M. Jin. Tomographic reconstruction of dynamic cardiac image sequences. *IEEE Trans. Im. Proc.*, 16(4):932–42, April 2007.

[30] E. Gravier, Y. Yang, M. A. King, and M. Jin. Fully 4D motion-compensated reconstruction of cardiac SPECT images. *Phys. Med. Biol.*, 51(18):4603–20, September 2006.

[31] E. J. Gravier and Y. Yang. Motion-compensated reconstruction of tomographic image sequences. *IEEE Trans. Nuc. Sci.*, 52(1):51–6, February 2005.

[32] D. L. G. Hill, P. G. Batchelor, M. Holden, and D. J. Hawkes. Medical image registration. *Phys. Med. Biol.*, 46(3):R1–47, March 2001.

[33] M. Holden. A review of geometric transformations for nonrigid body registration. *IEEE Trans. Med. Imag.*, 27(1):111–28, January 2008.

[34] M. Jacobson. *Approaches to motion-corrected PET image reconstruction from respiratory gated projection data*. PhD thesis, Univ. of Michigan, Ann Arbor, MI, 48109-2122, Ann Arbor, MI, 2006.

[35] M. W. Jacobson and J. A. Fessler. Joint estimation of image and deformation parameters in motion-corrected PET. In *Proc. IEEE Nuc. Sci. Symp. Med. Im. Conf.*, volume 5, pages 3290–4, 2003.

[36] M. W. Jacobson and J. A. Fessler. Joint estimation of respiratory motion and activity in 4D PET using CT side information. In *Proc. IEEE Intl. Symp. Biomed. Imag.*, pages 275–8, 2006.

[37] M. W. Jacobson and J. A. Fessler. An expanded theoretical treatment of iteration-dependent majorize-minimize algorithms. *IEEE Trans. Im. Proc.*, 16(10):2411–22, October 2007.

[38] B. Karacali and C. Davatzikos. Estimating topology preserving and smooth displacement fields. *IEEE Trans. Med. Imag.*, 23(7):868–80, July 2004.

[39] A. L. Kesner, R. A. Bundschuh, N. C. Detorie, M. Dahlbom, J. Czernin, and D. H. S. Silverman. Respiratory gated pet derived from raw pet data. In *Nuclear Science Symposium Conference Record, 2007. NSS '07. IEEE*, volume 4, pages 2686–2691, 2007.

[40] A.L. Kesner, M. Dahlbom, J. Czernin, and D.H.S. Silverman. Recombining respiratory gated pet frames. In *Nuclear Science Symposium Conference Record, 2007. NSS '07. IEEE*, volume 5, pages 3961–3963, 26 2007-Nov. 3 2007.

[41] J. Kim. *Intensity based image registration using robust similarity measure and constrained optimization: applications for radiation therapy*. PhD thesis, Univ. of Michigan, Ann Arbor, MI, 48109-2122, Ann Arbor, MI, 2004.

[42] J. Kim. Non-rigid image registration using constrained optimization (Korean). *Journal of Korea Information and Communications*, 29(10C):1402–13, 2004.

[43] J. Kim and J. A. Fessler. Nonrigid image registration using constrained optimization. In *SIAM Conf. Imaging Sci., Abstract Book*, 2004.

[44] G. J. Klein and R. H. Huesman. Four-dimensional processing of deformable cardiac PET data. *Med. Im. Anal.*, 6(1):29–46, March 2002.

[45] G. J. Klein, B. W. Reutter, M. H. Ho, J. H. Reed, and R. H. Huesman. Real-time system for respiratory-cardiac gating in positron tomography. *IEEE Trans. Nuc. Sci.*, 45(4):2139–43, August 1998.

[46] G. J. Klein, B. W. Reutter, and R. H. Huesman. Non-rigid summing of gated PET via optical flow. *IEEE Trans. Nuc. Sci.*, 44(4):1509–12, August 1997.

[47] J. Kybic, P. Thevenaz, A. Nirkko, and M. Unser. Unwarping of unidirectionally distorted EPI images. *IEEE Trans. Med. Imag.*, 19(2):80–93, February 2000.

[48] J. Kybic and M. Unser. Fast parametric elastic image registration. *IEEE Trans. Im. Proc.*, 12(11):1427–42, November 2003.

[49] D. S. Lalush and B. M. W. Tsui. Block-iterative techniques for fast 4D reconstruction using a priori motion models in gated cardiac SPECT. *Phys. Med. Biol.*, 43(4):875–86, April 1998.

[50] F Lamare, T Cresson, J Savean, C Cheze Le Rest, A J Reader, and D Visvikis. Respiratory motion correction for PET oncology applications using affine transformation of list mode data. *Physics in Medicine and Biology*, 52(1):121–140, January 2007.

[51] F Lamare, T Cresson, J Savean, C Cheze Le Rest, A J Reader, and D Visvikis. Respiratory motion correction for PET oncology applications using affine transformation of list mode data. *Physics in Medicine and Biology*, 52(1):121–140, January 2007.

[52] F. Lamare, M. J. Ledesma Carbayo, T. Cresson, G. Kontaxakis, A. Santos, C. Cheze LeRest, A. J. Reader, and D. Visvikis. List-mode-based reconstruction for respiratory motion correction in PET using non-rigid body transformations. *Phys. Med. Biol.*, 52(17):5187–204, September 2007.

[53] T. Li, B. Thorndyke, E. Schreibmann, Y. Yang, and L. Xing. Model-based image reconstruction for four-dimensional PET. *Med. Phys.*, 33(5):1288–98, May 2006.

[54] Zhouchen Lin and Heung-Yeung Shum. Fundamental limits of reconstruction-based superresolution algorithms under local translation. *IEEE Trans. Pattern Anal. Mach. Intell.*, 26(1):83–97, 2004.

[55] J. A. Little, D. L. G. Hill, and D. J. Hawkes. Deformations incorporating rigid structures. *Comp. Vision & Im. Understanding*, 66(2):223–32, May 1997.

[56] D. Loeckx, F. Maes, D. Vandermeulen, and P. Suetens. Nonrigid image registration using free-from deformations with a local rigidity constraint. In *Medical Image Computing and Computer-Assisted Intervention*, volume LNCS 3216, pages 639–46, 2004.

[57] B. A. Mair, D. R. Gilland, and J. Sun. Estimation of images and nonrigid deformations in gated emission CT. *IEEE Trans. Med. Imag.*, 25(9):1130–44, September 2006.

[58] R. Manjeshwar, . X. Tao, E. Asma, and K. Thielemans. Motion compensated image reconstruction of respiratory gated PET/CT. In *Proc. IEEE Intl. Symp. Biomed. Imag.*, pages 674–7, 2006.

[59] Ludovic Le Meunier, Roberto Maass-Moreno, Jorge A. Carrasquillo, William Dieckmann, and Stephen L. Bacharach. Pet/ct imaging: Effect of respiratory motion on apparent myocardial uptake. *Journal of Nuclear Cardiology*, 13(6):821 – 830, 2006.

[60] J. Modersitzki. FLIRT with rigidity–Image registration with a local non-rigidity penalty. *Intl. J. Comp. Vision*, 76(2):153–63, February 2008.

[61] O. Musse, F. Heitz, and J. P. Armspach. Topology preserving deformable image matching using constrained hierarchical parametric models. *IEEE Trans. Im. Proc.*, 10(7):1081–93, July 2001.

[62] S. A. Nehmeh, Y. E. Erdi, C. C. Ling, K. E. Rosenzweig, H. Schoder, S. M. Larson, H. A. Macapinlac, O. D. Squire, and J. L. Humm. Effect of respiratory gating on quantifying PET images of lung cancer. *J. Nuc. Med.*, 43(7):876–81, July 2002.

[63] S. A. Nehmeh, Y. E. Erdi, T. Pan, E. Yorke, G. S. Mageras, K. E. Rosenzweig, H. Schoder, H. Mostafavi, O. Squire, A. Pevsner, S. M. Larson, and J. L. Humm. Quantitation of respiratory motion during 4D-PET/CT acquisition. *Med. Phys.*, 31(6):1333–8, June 2004.

[64] Sadek A. Nehmeh and Yusuf E. Erdi. Respiratory motion in positron emission tomography/computed tomography: a review. *Semin Nucl Med.*, 38(3):167–176, 2008.

[65] M.K. Ng and N.K. Bose. Mathematical analysis of super-resolution methodology. *Signal Processing Magazine, IEEE*, 20(3):62–74, May 2003.

[66] N. Nguyen, P. Milanfar, and G. Golub. A computationally efficient superresolution image reconstruction algorithm. *IEEE Trans. Im. Proc.*, 10(4):573–83, April 2001.

[67] T. E. Nichols, J. Qi, E. Asma, and R. M. Leahy. Spatiotemporal reconstruction of list mode PET data. *IEEE Trans. Med. Imag.*, 21(4):396–404, April 2002.

[68] V. Noblet, C. Heinrich, F. Heitz, and J-P. Armspach. 3-D deformable image registration: a topology preservation scheme based on hierarchical deformation models and interval analysis optimization. *IEEE Trans. Im. Proc.*, 14(5):553–66, May 2005.

[69] F. Odille, N. Cîndea, D. Mandry, Cédric Pasquier, P-A. Vuissoz, and J. Felblinger. Generalized MRI reconstruction including elastic physiological motion and coil sensitivity encoding. *Mag. Res. Med.*, 59(6):1401–11, June 2008.

[70] F. Odille, P-A. Vuissoz, P-Y. Marie, and J. Felblinger. Generalized reconstruction by inversion of coupled systems (GRICS) applied to free-breathing MRI. *Mag. Res. Med.*, 60(1):146–57, July 2008.

[71] Asit K. Paul and Hani A. Nabi. Gated Myocardial Perfusion SPECT: Basic Principles, Technical Aspects, and Clinical Applications. *J Nucl Med Technol*, 32(4):179–187, 2004.

[72] J. P. W. Pluim, J. B. A. Maintz, and M. A. Viergever. Mutual-information-based registration of medical images: a survey. *IEEE Trans. Med. Imag.*, 22(8):986–1004, August 2003.

[73] W. H. Press, B. P. Flannery, S. A. Teukolsky, and W. T. Vetterling. *Numerical recipes in C*. Cambridge Univ. Press, New York, 2 edition, 1992.

[74] J. Qi and R. M. Leahy. Resolution and noise properties of MAP reconstruction for fully 3D PET. *IEEE Trans. Med. Imag.*, 19(5):493–506, May 2000.

[75] F. Qiao, T. Pan, J. W. Clark, and O. R. Mawlawi. A motion-incorporated reconstruction method for gated PET studies. *Phys. Med. Biol.*, 51(15):3769–84, August 2006.

[76] M. Reyes, G. Malandain, P. M. Koulibaly, M. A. González-Ballester, and J. Darcourt. Model-based respiratory motion compensation for emission tomography image reconstruction. *Phys. Med. Biol.*, 52(12):3579–600, June 2007.

[77] C. J. Ritchie, J. Hsieh, M. F. Gard, J. D. Godwin, Y. Kim, and C. R. Crawford. Predictive respiratory gating: a new method to reduce motion artifacts on CT scans. *Radiology*, 190(3):847–52, March 1994.

[78] D. Robinson and P. Milanfar. Fundamental performance limits in image registration. *IEEE Trans. Im. Proc.*, 13(9):1185–99, September 2004.

[79] D. Robinson and P. Milanfar. Statistical performance analysis of super-resolution. *Image Processing, IEEE Transactions on*, 15(6):1413–1428, June 2006.

[80] G. K. Rohde, A. Aldroubi, and B. M. Dawant. The adaptive bases algorithm for intensity-based nonrigid image registration. *IEEE Trans. Med. Imag.*, 22(11):1470–9, November 2003.

[81] T. Rohlfing, C. R. Maurer, D. A. Bluemke, and M. A. Jacobs. Volume-preserving nonrigid registration of MR breast images using free-form deformation with an incompressibility constraint. *IEEE Trans. Med. Imag.*, 22(6):730–741, June 2003.

[82] D. Ruan. *Image guided respiratory motion analysis: time series and image registration*. PhD thesis, Univ. of Michigan, Ann Arbor, MI, 48109-2122, Ann Arbor, MI, 2008.

[83] D. Ruan, J. A. Fessler, and S. Esedoğlu. Discontinuity preserving regularization for modeling sliding effects in medical image registration. In *Proc. IEEE Nuc. Sci. Symp. Med. Im. Conf.*, pages 5304–8, 2008.

[84] D. Ruan, J. A. Fessler, M. Roberson, J. Balter, and M. Kessler. Nonrigid registration using regularization that accommodates local tissue rigidity. In *Proc. SPIE 6144, Medical Imaging 2006: Image Proc.*, pages 614412:1–9, 2006.

[85] D. Rueckert, P. Aljabar, R. A. Heckemann, J. V. Hajnal, and A. Hammers. Diffeomorphic registration using B-splines. In *Medical Image Computing and Computer-Assisted Intervention*, pages 702–9, 2006.

[86] D. Rueckert, L. I. Sonoda, C. Hayes, D. L. G. Hill, M. O. Leach, and D. J. Hawkes. Nonrigid registration using free-form deformations: application to breast MR images. *IEEE Trans. Med. Imag.*, 18(8):712–21, August 1999.

[87] M. Sdika. A fast nonrigid image registration with constraints on the jacobian using large scale constrained optimization. *IEEE Trans. Med. Imag.*, 27(2):271–81, February 2008.

[88] W. P. Segars, M. Mahesh, T. J. Beck, E. C. Frey, and B. M. W. Tsui. Realistic CT simulation using the 4D XCAT phantom. *Med. Phys.*, 35(8):3800–8, August 2008.

[89] H. R. Shi and J. A. Fessler. Quadratic regularization design for 2D CT. *IEEE Trans. Med. Imag.*, 2009. To appear as TMI-2008-0455.

[90] O. Skrinjar and H. Tagare. Symmetric, transitive, geometric deformation and intensity variation invariant nonrigid image registration. In *Biomedical Imaging: Nano to Macro, 2004. IEEE International Symposium on*, pages 920–923 Vol. 1, April 2004.

[91] G. S. Slavin and D. A. Bluemke. Spatial and temporal resolution in cardiovascular MR imaging: review and recommendations. *Radiology*, 234(2):330–8, February 2005.

[92] C. O. S. Sorzano, P. Thevenaz, and M. Unser. Elastic registration of biological images using vector-spline regularization. *IEEE Trans. Biomed. Engin.*, 52(4):652–63, April 2005.

[93] M. Staring, S. Klein, and J. P. W. Pluim. A rigidity penalty term for nonrigid registration. *Med. Phys.*, 34(11):4098–108, November 2007.

[94] J. W. Stayman and J. A. Fessler. Regularization for uniform spatial resolution properties in penalized-likelihood image reconstruction. *IEEE Trans. Med. Imag.*, 19(6):601–15, June 2000.

[95] Richard Szeliski and James Coughlan. Spline-based image registration. *Int. J. Comput. Vision*, 22(3):199–218, 1997.

[96] K. Taguchi and H. Kudo. Motion compensated fan-beam reconstruction for nonrigid transformation. *IEEE Trans. Med. Imag.*, 27(7):907–17, July 2008.

[97] K. Taguchi, W. P. Segars, G. S. K. Fung, and B. M. W. Tsui. Toward time resolved 4D cardiac CT imaging with patient dose reduction: estimating the global heart motion. In *Proc. SPIE 6142, Medical Imaging 2006: Phys. Med. Im.*, page 61420J, 2006.

[98] K. Taguchi, W. P. Segars, H. Kudo, E. C. Frey, E. K. Fishman, and B. M. W. Tsui. Toward time resolved cardiac CT images with patient dose reduction: Image-based motion estimation. In *Proc. IEEE Nuc. Sci. Symp. Med. Im. Conf.*, volume 4, pages 2029–32, 2006.

[99] K. Taguchi, Z. Sun, W. P. Segars, E. K. Fishman, and B. M. W. Tsui. Image-domain motion compensated time resolved 4D cardiac CT. In *Proc. SPIE 6510, Medical Imaging 2007: Phys. Med. Im.*, page 651016, 2007.

[100] K. Taguchi, M. Zhang, E. C. Frey, J. Xu, W. Paul Segars, and B. M. W. Tsui. Image-domain material decomposition using photon-counting CT. In *Proc. SPIE 6510, Medical Imaging 2007: Phys. Med. Im.*, page 651008, 2007.

[101] M. Tanaka and M. Okutomi. Theoretical analysis on reconstruction-based super-resolution for an arbitrary psf. In *Computer Vision and Pattern Recognition, 2005. CVPR 2005. IEEE Computer Society Conference on*, volume 2, pages 947–954, June 2005.

[102] K. Thielemans, R.M. Manjeshwar, Xiaodong Tao, and E. Asma. Lesion detectability in motion compensated image reconstruction of respiratory gated pet/ct. In *Nuclear Science Symposium Conference Record, 2006. IEEE*, volume 6, pages 3278–3282, Nov 2006.

[103] B. Thorndyke, E. Schreibmann, A. Koong, and L. Xing. Reducing respiratory motion artifacts in positron emission tomography through retrospective stacking. *Med. Phys.*, 33(7):2632–41, July 2006.

[104] M. Unser. Splines: A perfect fit for signal and image processing. *spmag*, 16(6):22–38, November 1999.

[105] M. Unser, A. Aldroubi, and M. Eden. Fast B-spline transforms for continuous image representation and interpolation. *IEEE Trans. Patt. Anal. Mach. Int.*, 13(3):277–85, March 1991.

[106] M. Unser, A. Aldroubi, and M. Eden. B-spline signal processing: Part I—theory. *IEEE Trans. Sig. Proc.*, 41(2):821–33, February 1993.

[107] M. Unser, A. Aldroubi, and M. Eden. B-spline signal processing: Part II—efficient design and applications. *IEEE Trans. Sig. Proc.*, 41(2):834–48, February 1993.

[108] M. Unser, A. Aldroubi, and M. Eden. The L_2 polynomial spline pyramid. *IEEE Trans. Patt. Anal. Mach. Int.*, 15(4):364–79, April 1993.

[109] S. S. Vedam, P. J. Keall, V. R. Kini, H. Mostafavi, H. P. Shukla, and R. Mohan. Acquiring a four-dimensional computed tomography dataset using an external respiratory signal. *Phys. Med. Biol.*, 48(1):45–62, January 2003.

[110] W. M. Wells, P. Viola, H. Atsumi, S. Nakajima, and R. Kikinis. Multi-modal volume registration by maximization of mutual information. *Med. Im. Anal.*, 1(1):35–51, March 1996.

[111] R. Zeng, J. A. Fessler, and J. M. Balter. Respiratory motion estimation from slowly rotating X-ray projections: Theory and simulation. *Med. Phys.*, 32(4):984–91, April 2005.

[112] R. Zeng, J. A. Fessler, and J. M. Balter. Estimating 3-D respiratory motion from orbiting views by tomographic image registration. *IEEE Trans. Med. Imag.*, 26(2):153–63, February 2007.

[113] Marcelo V. W. Zibetti, Fermín S. V. Bazán, and Joceli Mayer. Determining the regularization parameters for super-resolution problems. *Signal Process.*, 88(12):2890–2901, 2008.

[114] Marcelo Victor Wüst Zibetti and Joceli Mayer. Simultaneous super-resolution for video sequences. In *ICIP (1)*, pages 877–880, 2005.

[115] M.V.W. Zibetti and J. Mayer. A robust and computationally efficient simultaneous super-resolution scheme for image sequences. *Circuits and Systems for Video Technology, IEEE Transactions on*, 17(10):1288–1300, Oct. 2007.